DIRECT AIR CAPTURE

CHARACTERIZATION AND DESIGN OF A NOVEL ABSORPTION PROCESS

by

Mrigank Sinha

in partial fulfillment of the requirements for the degree of

Master of Science
in Mechanical Engineering

at the Delft University of Technology,
to be defended publicly on Friday December 20, 2019 at 13:00.

Student number:	4727274	
Daily Supervisor:	Ir. J. van Kranendonk,	ZEF B.V.
Thesis committee:	Prof. dr. ir. E. Goetheer (Chair),	TU Delft
	Dr. R. Delfos,	TU Delft
	Prof. dr. ir. W. de Jong,	TU Delft

This thesis is confidential and cannot be made public until December 20, 2021.

An electronic version of this thesis is available at http://repository.tudelft.nl/.

TU Delft Delft University of Technology

ABSTRACT

Rising concentration of CO_2 in the atmosphere has become a significant concern, paving the way for worldwide research on mitigation techniques like carbon capture and storage (CCS) and carbon capture and utilization (CCU). Zero Emission Fuel (ZEF), an aspiring startup based in the Netherlands, aims to develop a micro plant that produces methanol from just solar energy and air. Their process involves capturing CO_2 and H_2O directly from the air, splitting H_2O to obtain H_2 and producing methanol by reacting CO_2 with H_2. The focus of this research is on the absorption process of ZEF's direct air capture unit. Instead of capturing CO_2 and H_2O through a widely used batch direct air capture process, ZEF chooses to side with a novel continuous absorption and desorption process involving a flow of bulk polyamines without any conventional support structures. Polyethyleneimine (PEI-MW-600) and Tetraethylenepentamine (TEPA) are used as absorbents to achieve a target of capturing 825 grams of CO_2 in 8 hours every day from a single direct air capture unit.

Preliminary investigations show that the viscosity of PEI-600 is significantly higher than that of TEPA. An increase in CO_2 concentration increases the viscosity of both polyamines significantly. In comparison, increasing H_2O concentration leads to a maximum viscosity point in both polyamines and subsequent decrease in viscosity with a further increase in H_2O concentration. Although, compared to CO_2, H_2O has a smaller effect on viscosity. Moreover, premixed samples of PEI-600 and TEPA with H_2O show an increase in the CO_2 absorption rate when pure CO_2 is bubbled through the samples.

In order to study and characterize the novel absorption process, an experimental setup facilitating a flow of absorbent is developed, and experiments are conducted following an experimental approach to calculate the mass transfer rates and average concentrations of CO_2 and H_2O. Fourier-transform infrared spectroscopy is used to estimate these concentrations. Experiments are performed on different initial concentrations of PEI and TEPA. TEPA is found to have a better absorption performance with an average CO_2 absorption rate that is two times higher than PEI-600. Contrary to preliminary investigations done by bubbling CO_2 into polyamines, absorbents with premixed water flowing down a channel were found to have lower CO_2 absorption rates than pure polyamines.

A multiple regression viscosity model, heat model, and a model of absorption column is developed using the data collected to estimate average viscosity, the heat of absorption of water, and characteristics of the absorption process. Diffusion of CO_2 through the absorbent layers is found to be the primary limiting factor, while mass flow rates of absorbent and air are also found to influence the absorption process.

Finally, a design of the absorption column is made to meet ZEF's requirement taking into account various performance characteristics studied during the thesis.

ACKNOWLEDGEMENTS

The journey I have made in the last 9 to 10 months has made me stronger, has given me confidence and a strong sense of purpose to move ahead in my life, achieving goals that once seemed very distant. I take pride in admitting that this change in mindset and evolution wasn't all my doing. I feel blessed and lucky to have known many people who were a part of my journey, helping and inspiring me all along.

Firstly, I thank Zero Emission Fuels to give me an opportunity to do my thesis with them, providing an open learning platform and an energetic environment with a buzz of new ideas budding every day.

Jan van Kranendonk, you have been my mentor and an immense source of inspiration throughout my thesis and time at ZEF. Thank you for putting your faith in me, answering my questions on weekends and showing me the horizon of intellectual smartness. I don't know how but my discussion sessions with you always fill me with enthusiasm and determination and every time it ends it leaves me with new knowledge and perspective. Thank you.

Ulrich Starke, you have been a constant source of strength to me, giving me direction, support, and advice whenever I didn't see the light at the end of the tunnel. Your grit, mentality, and attitude to achieve set goals inspire me. Thank you for your constant encouragement and belief in me.

Hessel Jongebreur, thank you for pats on the back and being the voice of wisdom even when I did not realize that I needed help. Your humility, kindness and the incredible talent to always say what is needed leave me in awe even today.

I would also like to thank Professor Earl Goetheer for being my thesis chair and motivating me in many ways throughout my thesis. Thank you for the early morning meetings and entertaining my weird hypothesis every now and then. You positively pushed me to achieve more and always made time for me even with your busy schedule. Your belief in me gave me strength and an urge to do more. Your idea about bringing different fields together to achieve a common goal inspires me. Thank you.

Dr. Rene Delfos, you have been instrumental in evolving the way I think. I never felt any barrier to go and speak with you and I always left with a solution to my problems. You showed interest in my work even though some of it wasn't related to your field of study. You made sure to give me a positive remark every time I achieved something. You taught me to look at things from a fundamental point of view and reason everything out without jumping to conclusions. Thank you.

A very strong support system has been my family in Netherlands, my housemates. Sawan, Kalpit, Afshan and Neel thank you for being there in times of need. In your own ways, each of you helped. We still stick together after two and a half years in both happiness and sadness. Our daily rituals are something one would rarely find anywhere else. Thank you.

Floor Boon, you are a close friend and have become really important to me in this last year. You have seen me at my lowest and at my peak and yet haven't differentiated. You have helped me in more ways than I care to admit. We are still a team and it gives me a lot of strength knowing that I can rely on you and get your counsel when I am lost. You taught me an alternate way to view things. Unknowingly, you push me to perform better and achieve things that seem distant at first. Thank you.

Mom, Dad and Bhavya, thank you for being the rock behind me and showering me with love and support.

Dadi ma, this thesis is dedicated to you. I promised you that I will make my own name, pave my own path and make a good strong statement whenever I can. I am keeping that promise no matter what. You always believed in me and loved me unconditionally. That belief you had in me has been my candle in dark times. Thank you. I hope I can make you proud.

I would also like to thank Professor Brian Tighe, Evert Vixseboxse and my friends Fenna, Arya, Koen, Marieke, Gokberk, Abhinaw and Raghav for helping me out and being a positive influence on me.

NOMENCLATURE

Table 1: List of molecules mentioned in this thesis

Molecular Structure	Description
OH^-	Hydroxide ion
CO_2	Carbon dioxide
H_2O	Water
$NaOH$	Sodium Hydroxide
H_2	Hydrogen
O_2	Oxygen
KOH	Potassium Hydroxide
Na_2CO_3	Sodium Carbonate
K_2CO_3	Potassium Carbonate
$CaCO_3$	Calcium Carbonate
$Ca(OH)_2$	Calcium Hydroxide
CaO	Calcium Oxide
CH_4	Methane
Y_2O_3	Yttrium Oxide
RNH_3	Primary amine
R_2NH	Secondary amine
R_3N	Tertiary amine
$RNH_2{}^+COO^-$	Zwitterion
$RNHCOO^-$	Carbamate
$HCO_3{}^-$	Bicarbonate

Table 2: List of abbreviations used in this thesis

Abbreviation	Description
ZEF	Zero Emission Fuels
DAC	Direct Air Capture
CCS	Carbon Capture and storage
CCU	Carbon capture and utilization
MEA	Monoethanolamine
DEA	Diethanolamine
TEA	Triethylamine
MDEA	Methyldiethanolamine
MeOH	Methanol
PEI-600	Polyethyleneimine (Molecular weight of 600 grams /mol)
TEPA	Tetraethylenepentamine
TSA	Temperature swing absorption
VSA	Vacuum swing absorption
PSA	Pressure swing absorption
FTIR	Fourier-transform infrared spectroscopy
NMR	Nuclear magnetic resonance spectroscopy

CONTENTS

List of Figures

List of Tables

1

INTRODUCTION

In the following chapter, one of the major global problems on Earth is discussed briefly along with its cause and effects. Thereafter, some possible solutions are discussed and the motivation for this thesis is established. Subsequently, the scope and research objectives of the thesis are mentioned and the chapter concludes with the thesis approach and the report outline.

1.1. THE PROBLEM AT HAND

In terms of scientific development, humans have evolved admirably in the last few centuries. However, the development of advanced technology comes at a great cost. The global energy demand is increasing and is still satisfied majorly by fossil fuels. In addition to depleting our fossil fuel reserves, we are also increasing greenhouse gas emissions by burning these fossil fuels to produce heat and energy. As a result, we are experiencing a rise in the average temperature of the Earth's climate, a phenomenon referred to as climate change and more commonly known as *global warming*.

1.1.1. INCREASE IN GLOBAL ENERGY CONSUMPTION

As technology is becoming easily accessible to people, their lifestyle standards are rising with time which has a direct consequence on global energy consumption. Figure 1.1 shows the steep increase of the global primary energy consumption in recent years.

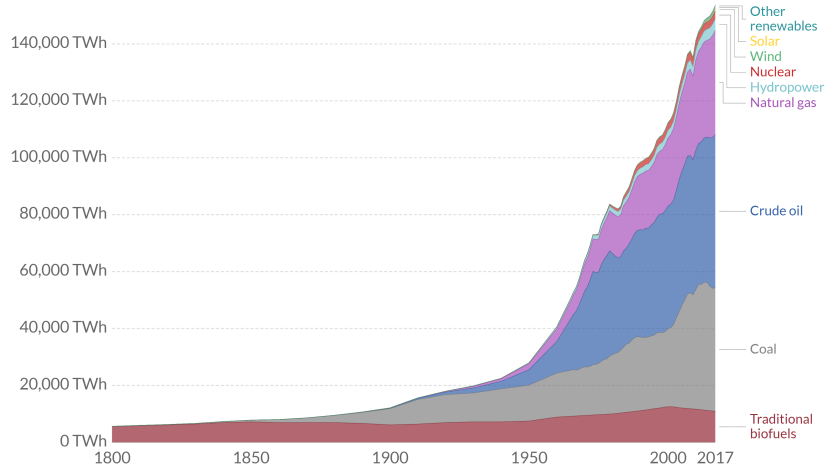

Figure 1.1: Global primary energy consumption, measured in terawatt-hours (TWh) per year [1]

1.1.2. FOSSIL FUELS

A close inspection of figure 1.1 would lead to a realization that even today, the majority of our energy consumption is through fossil fuel reserves. To put things in perspective, the contribution of fossil fuels in global energy consumption is isolated and shown in figure 1.2. The consequence of this is two folds. Not only are we depleting our fossil fuel reserves, but also increasing the global greenhouse gas emissions [26].

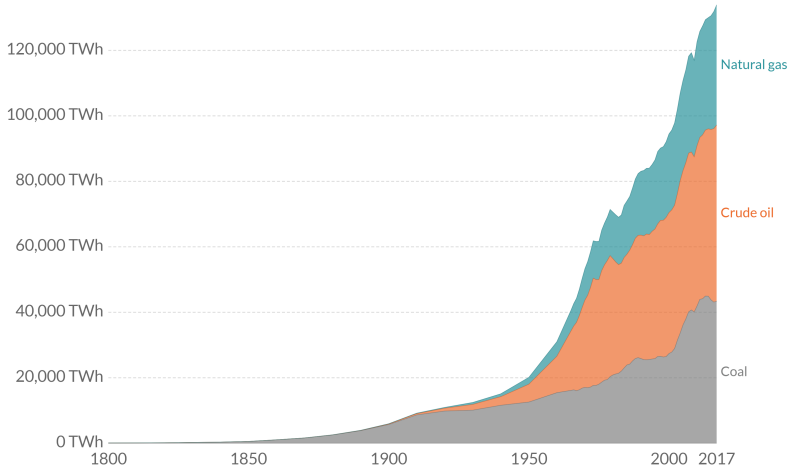

Figure 1.2: Global primary energy consumption by fossil fuel source, measured in terawatt-hours (TWh) [2]

1.1.3. CO_2 EMISSIONS

Greenhouse gas emissions are majorly comprised of carbon dioxide [27]. The global energy related CO_2 emissions reached a value of 33.1 Gt CO_2 in 2018, being the highest value recorded ever [28].The consequence of these emissions can be seen in Figure 1.3, which shows the increase of concentration of CO_2 over the years in the atmosphere.

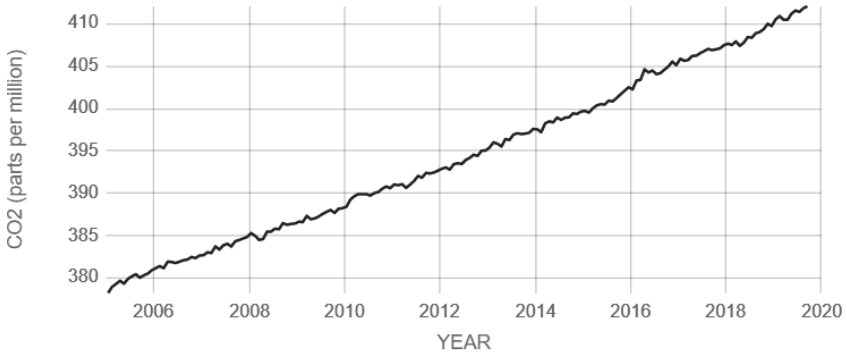

Figure 1.3: Increase in concentration of CO_2 (ppm) in the atmosphere per year [3]

1.1.4. CONSEQUENCES

The global climate is changing for worse and with the increase in the greenhouse gas emissions, the global average temperature is also steadily increasing. The last decade was the warmest decade since 1880 with 2016 being the warmest year ever recorded [29][30]. Figure 1.4 sheds light on the global temperature anomaly.

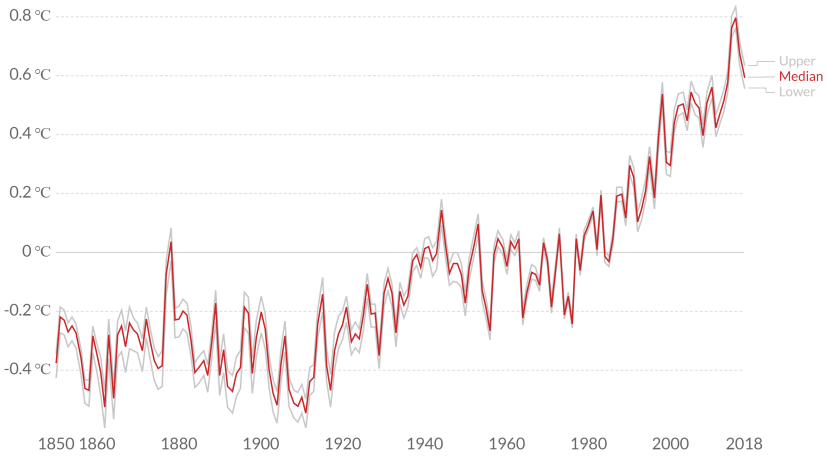

Figure 1.4: Global average temperature anomaly relative to 1961-1990 average temperature in degree celsius ($^{\circ}C$) [4]

Severe weather conditions, air pollution, higher wildlife extinction rates, acidic oceans and higher sea levels are some of the well known affects of climate change. With the world's population increasing drastically, the energy demand would only increase in the coming years, which in turn would lead to increase in consumption of fossil fuels, higher CO_2 emissions and thus *global warming*. It is high time to work towards mitigation techniques to counter or reduce the CO_2 concentration in air.

1.2. MITIGATION

Initially, this section briefly discusses the current mitigation measures to reduce CO_2 emissions. The section concludes with the introduction of Direct Air Capture, the chosen miti-

gation technique for this thesis.

1.2.1. CARBON MANAGEMENT

Many mitigation technologies have been developed and are currently in use throughout the world. Broadly, these can be classified into three main approaches:

- **Energy Efficient Technologies:** This method aims at building energy efficient technologies which could help in reducing CO_2 emissions.
- **Carbon Capture and Storage (CCS):** This process involves capturing waste carbon dioxide from large point sources such as factories or power plants and transporting it to a storage site, usually a geological formation where it is deposited so that it does not enter the atmosphere [31].
- **Carbon Capture and Utilization (CCU):** This process utilizes the captured carbon dioxide to produce products of higher economic value such as alternate energy sources like methanol, bio-fuels or other hydrocarbons or even commercial products like plastics or concrete [32][33].

Moving ahead, an important point to note is that most of the carbon dioxide capture is done from flue gasses from industries or power plants. If major sources of global CO_2 emissions by sector are considered, one would realize that a significant amount of these emissions are through sources other than industries and power plants. Other sectors like transport, residential & commercial and agriculture & land use contribute approximately 35% towards the total emissions [34].In order to stop or reduce the increasing levels of carbon dioxide in air, capturing it only through large point or concentrated sources will not be enough. This brings us to the broader topic of this thesis - Direct Air Capture.

1.2.2. INTRODUCTION TO DIRECT AIR CAPTURE

As the name suggests, direct air capture (DAC) is a process of capturing CO_2 directly from ambient air as compared to conventional carbon capture techniques which use point sources such as industries or power plants. The CO_2 captured can be used for storage or utilization. The most common capture technologies include chemical absorption or adsorption of CO_2. Large volumes of air are made to flow through filters or fixed beds which are usually impregnated with amines or other sorbents. Some of the common sorbents are monoethanolamine (MEA), diethanolamine (DEA), potassium hydroxide (KOH) and sodium hydroxide (NaOH). The sorbents are regenerated using pressure, temperature or moisture swing processes and used again [35][36].

ADVANTAGES

- Although the concentration of CO_2 in air is only about 0.04% which is 250 times lower when compared to roughly 10% in flue gases, the thermodynamic energy requirement of the process is only 2 to 4 times higher than that of flue gases [37][36].

- Direct air capture would enable CO_2 capture from any source. Its independence from concentrated point sources makes its location flexible. This could allow collection of CO_2 from many small fossil fuel burning units, which is not possible through other large scales conventional carbon capture techniques [26].
- Contaminants such as NO_x and SO_x are in found in lower concentrations in air than flue gases. Therefore the life time of the sorbents used in direct air capture could be higher [26].
- As a final advantage, DAC could be used to lower the concentration of CO_2 in air.

Even though the advantages of DAC look promising, building a DAC system which is cost effective with a high CO_2 capture rate can be challenging. This is where an ambitious startup known as Zero Emission Fuels comes into picture.

1.3. ZERO EMISSION FUELS (ZEF B.V.)

This thesis is done on behalf of Zero Emission Fuels (ZEF B.V.) working together with Delft University of Technology and Dutch organisation for Natural Science Research, TNO. Zero Emission fuels, a startup based in Delft, Netherlands aims at producing zero emission methanol by using just air and sunlight through integrated small scale methanol production plants. The entire process is divided into four subsystems as shown below in figure 1.5.

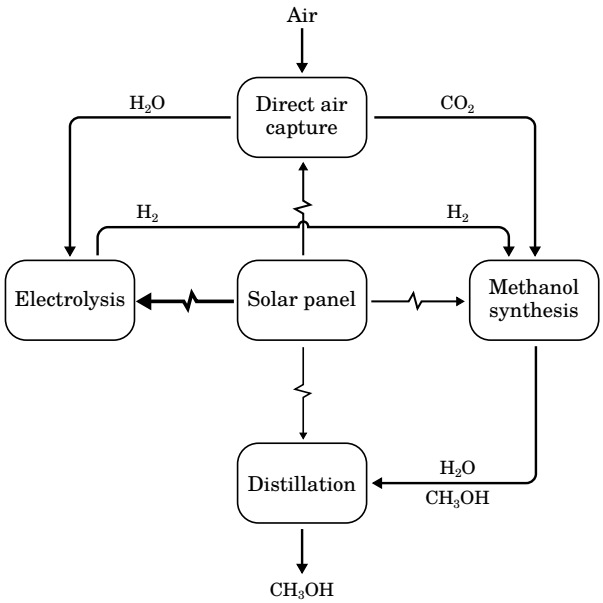

Figure 1.5: A schematic overview of a ZEF methanol production plant [5]

A description of the entire process of methanol production through each subsystem is given below:

- **Direct Air Capture:** The first step in ZEF's process starts with direct air capture where amine based absorbents are used to capture CO_2 and H_2O directly from air in the absorber and are separated through a desorber for further use.

- **Electrolysis:** The water captured by DAC is split into H_2 and O_2 in the electrolyzer and the H_2 is sent further to the methanol synthesis reactor.
- **Methanol Synthesis:** CO_2 from DAC and H_2 from the electrolyzer act as input for the methanol synthesis reactor which chemically converts them into the main product CH_3OH and byproduct H_2O.
- **Distillation:** H_2O, the byproduct is separated from CH_3OH through distillation to achieve 99.8% pure methanol which can be used as a commercial grade fuel.

The energy required to operate one such micro plant is delivered through 3 solar panels, each capable of producing 300 Watts. This thesis pertains to the DAC subsystem at ZEF. Before going into the research objectives of this project, general specifications of the DAC subsystem are mentioned.

1.3.1. DAC SUBSYSTEM

PRODUCTION SPECIFICATIONS

The ultimate goal of ZEF is to produce 600 grams of methanol per day through each micro plant. Since, the system is powered through a solar panel, it's intermittent power supply allows this subsystem to work for only 8 hours a day assuming average sunlight of 8 hours per day. Therefore, each DAC subsystem in a micro plant is required to capture sufficient CO_2 in its working hours for the methanol to be produced by the micro plant. The governing chemical reaction for methanol production is shown below.

$$CO_2 + 3\,H_2 \rightleftharpoons CH_3OH + H_2O \tag{1.1}$$

It can be seen from equation 1.1 that one mole of CO_2 reacts with three moles of H_2 to form one mole of CH_3OH. Therefore, in order to achieve a yield of 600 grams of CH_3OH per day, we would have to react 825 grams of CO_2. To conclude, the capture target of CO_2 is 825 grams every 8 hours.

CONTINUOUS DAC PROCESS

The developed DAC systems throughout the world use a batch direct air capture system. Having realized the potential of a continuous DAC system in terms of energy savings, ZEF revamped its DAC subsystem a year ago and is trying to build a continuous DAC system. The process requires a polyamine sorbent to flow continuously on a flow surface in a chamber while experiencing a counter current air flow. The sorbent absorbs CO_2 and H_2O from air and flows into the desorption chamber where it is regenerated and reused in the absorber. Although this process is chosen due to its mechanical simplicity and potential energy efficiency, prior research on such a system without a sorbent support structure has not been done.

CURRENT RESEARCH

Since, this type of a continuous DAC system is deemed to be a novel process, ZEF is currently researching on multiple aspects of this DAC system. To broadly classify, the research is divided into three pillars - absorption, desorption and life cycle analysis. Polyethyleneimine

(PEI) of molecular weight of 600 grams and Tetraethylenepentamine (TEPA) are currently being researched as potential sorbents.

This thesis is concerned with the absorption part of the research mentioned above on the two sorbents - PEI-600 and TEPA.

1.4. RESEARCH OBJECTIVES

The primary objective of this thesis is to **Characterize the continuous absorption process of PEI-600 and TEPA.** In order to achieve this objective, this research aims to answer the following research questions:

- What are the important characteristics influencing the absorption process?
- What are the limiting factors during absorption in a continuous process?
- What would be the preferred sorbent (PEI-600 or TEPA) from an absorption standpoint?

With the knowledge obtained from the research questions above, the final objective of this thesis is to **Design an absorption column that meets ZEF's requirements.**

1.5. THESIS SCOPE

Unlike many thesis projects, being a relatively novel research, characterisation of the absorption in a continuous can be exploratory. Therefore, it is necessary to define the scope of research before hand and some declarations should be made in advance.

- It is important to note that this thesis requires selection of a flow profile. Although this is done in subsequent chapters, the fluid flow dynamics are not researched. Having said that, some fluid properties are investigated due to the relevance in absorption characterisation.
- This project is solely done from an absorption standpoint and desorption or life cycle characteristics are not investigated.
- Despite the fact that literature study involves research done on many different amines, experiments are only performed on PEI-600 and TEPA.

1.6. REPORT OUTLINE AND APPROACH

Figure 1.6 shows the outline and the flow of this report. The report begins with a background research on commonly used polyamines and relevant literature study. Based on this study, some preliminary investigations are conducted to understand the behavior of polyamines pertaining to absorption. Subsequently, based on the these investigations and recommendations from previous research, an experimental setup is developed and experiments are conducted on PEI-600 and TEPA. A heat model and a model of absorption column is made using the data collected from experiments and finally, the absorption column

meeting ZEF's requirements is designed. The report ends with discussion on results and conclusions and detailed recommendations to provide a platform for future research.

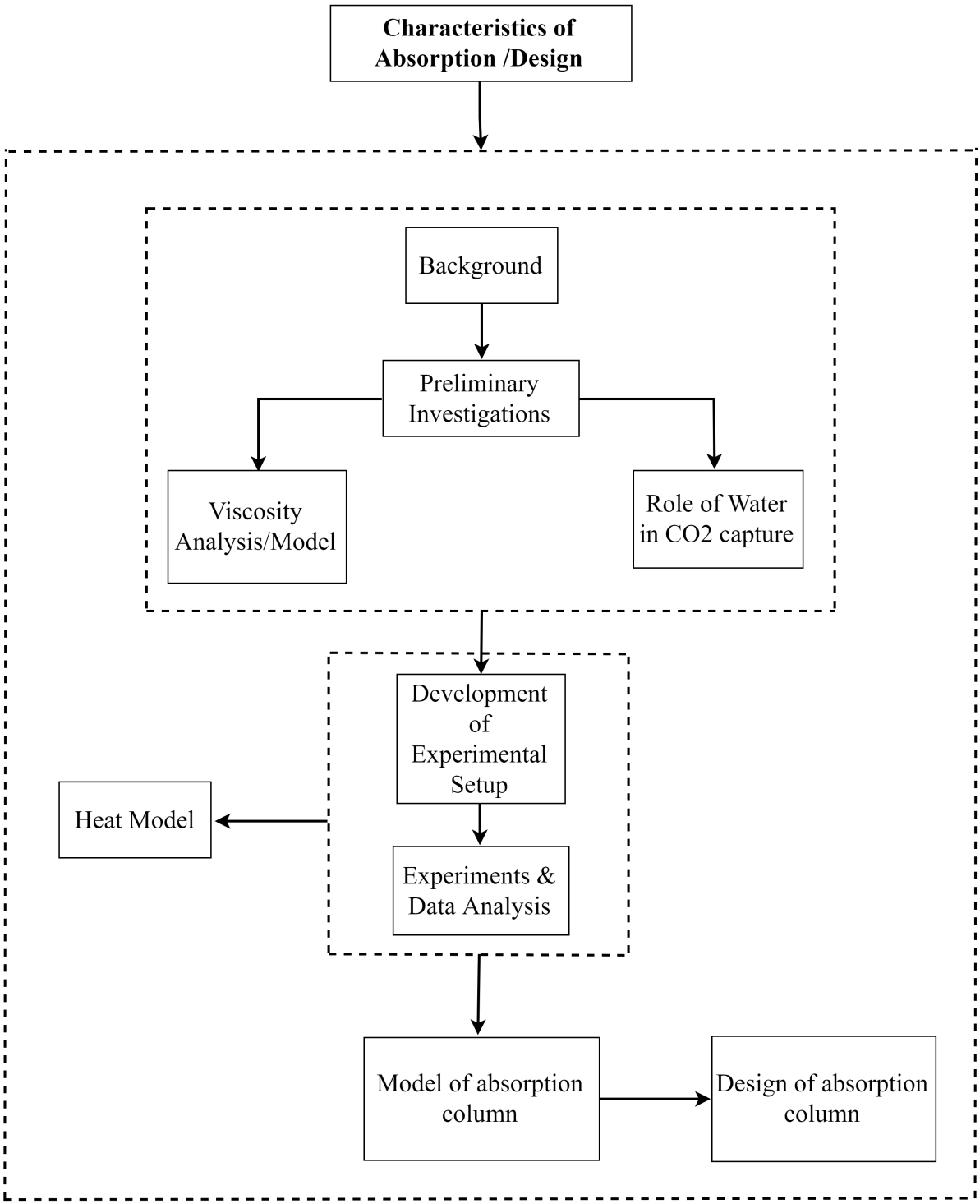

Figure 1.6: Outline of report

2

BACKGROUND

The following chapter commences with introduction to current direct air capture technologies to acquire an overview and methodology of functional DAC systems across the world. Thereafter, the details and evolution of ZEF's DAC system are studied and current problems are discovered. Subsequently, the background of amines in CO_2 capture is researched and the chapter concludes with the necessary steps required to proceed with this thesis.

2.1. CURRENT DAC TECHNOLOGIES

As the concentration of CO_2 is very dilute in air, most existing direct air capture systems utilize chemical sorbents due to their strong binding characteristics. Based on the type of sorbent, all available DAC technologies can be divided into 3 groups - aqueous solutions of strong bases, amine adsorptions and inorganic solid sorbents [38].This classification can further be simplified into *Liquid Solvent Systems* and *Solid Sorbent Systems* [6][39]. A few companies which are active in the DAC field are given below in figure 2.1.

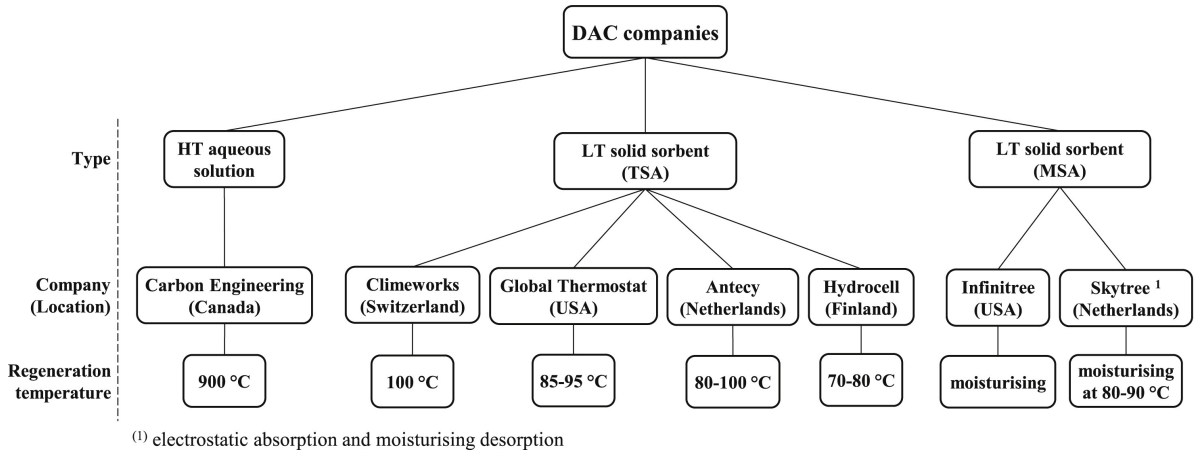

Figure 2.1: Active companies in the field of CO_2 DAC. Abbreviations: HT-high temperature, LT - low temperature, MSA - moisture swing adsorption, TSA - temperature swing adsorption [6]

2.1.1. LIQUID SOLVENT SYSTEM

This type of system consists of two components namely air contactor and re-generator which work simultaneously. Generally, sodium hydroxide ($NaOH$) or potassium hydroxide (KOH) are used as sorbents which are brought in contact with ambient air through the air contractor [40]. The CO_2 molecules react with the hydroxide solution to form a carbonate (Na_2CO_3 or K_2CO_3) solution. The re-generator takes the carbonate solution as input where it is mixed with calcium hydroxide ($Ca(OH)_2$) in the causticiser forming solid calcium carbonate ($CaCO_3$) and regenerating the hydroxide sorbent which is sent back to the air contactor. Meanwhile, the calciner unit heats the $CaCO_3$ at 900°C to release CO_2. The byproduct, calcium oxide (CaO) is mixed with water in the slaker unit to regenerate $Ca(OH)_2$ [6][39].Due to the high heat requirement in the re-generator, the liquid solvent DAC system is highly energy intensive. The process can be understood by the process diagram in figure 2.2 below.

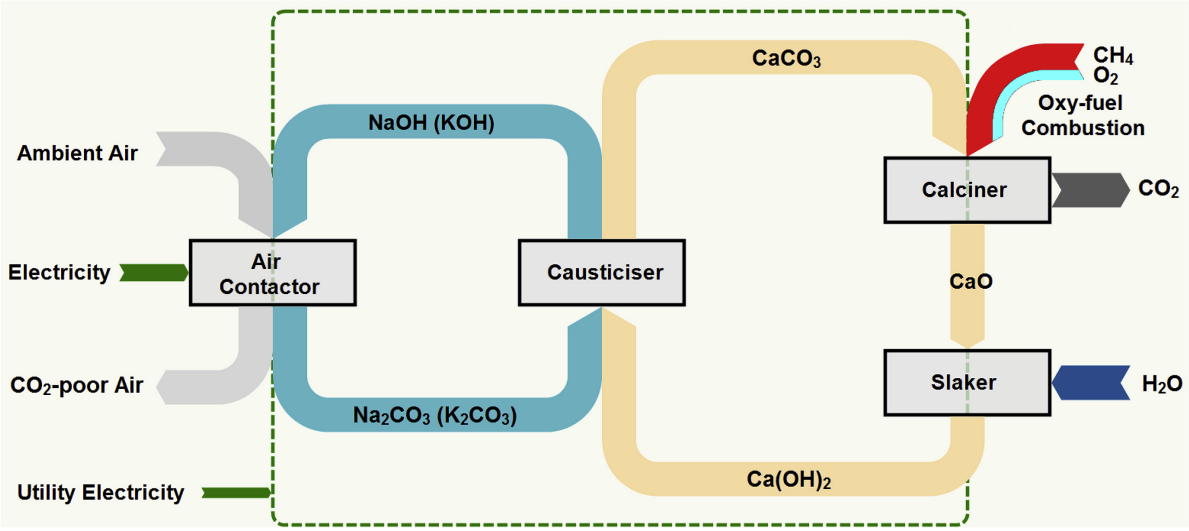

Figure 2.2: A liquid solvent DAC system using aqueous solutions of $NaOH$ or KOH [7][6]

The Canadian company, Carbon Engineering shown in figure 2.1, captures CO_2 from ambient air by utilizing potassium hydroxide (KOH) in a liquid solvent DAC system [6][39][41].

2.1.2. SOLID SORBENT SYSTEM

The two main processes in the solid sorbent system, similar to liquid sorbent system decribed in section 2.1.1 are adsorption and desorption [39]. Since temperature swing adsorption (TSA) is suitable when it comes to capturing ultra dilute species [42], generally either only TSA or TSA along with vacuum swing adsorption (VSA) is generally utilized.

ADSORPTION PROCESS

Ambient air is made to flow through an air contactor or filter, a solid structure made of CO_2 adsorbing material through the use of a fan. The solid structure chemically bonds the CO_2 and CO_2 depleted air flows out of the air contactor. Although this process is not as energy-intensive as desorption, the electrical power required to drive the fan can be considerably

high depending on the pressure drop.

DESORPTION PROCESS

After the sorbent is fully saturated, the adsorption process comes to a halt and the desorption stage commences. The system is heated and vacuumed (optional) and CO_2 is desorbed. Due to the heat required to induce the desorption of CO_2 (ΔH_{ads}) and electrical power required to drive the vacuum pumps, this process is the most energy intensive process in a solid sorbent DAC system [39].

The figure 2.3 briefly describes the important processes in a solid sorbent system.

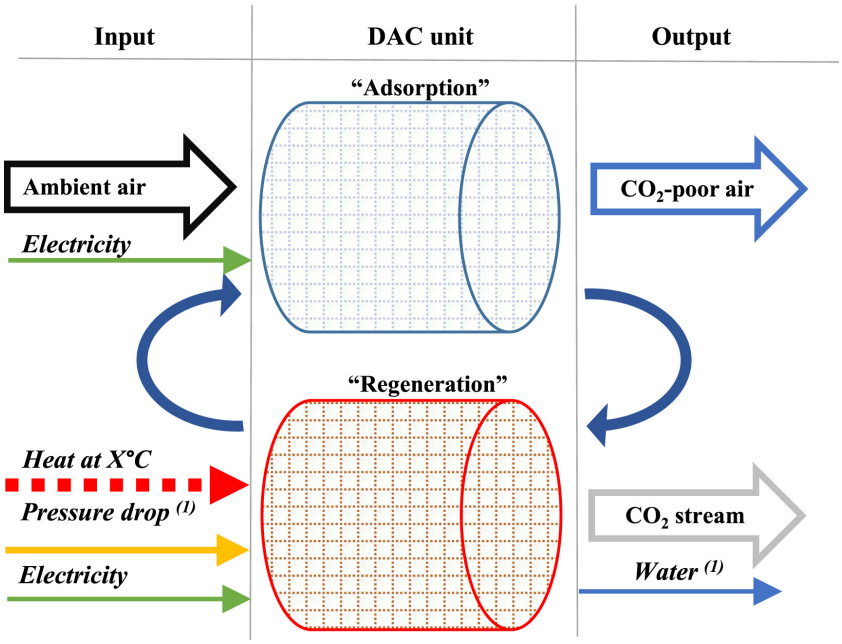

Figure 2.3: An overview of a solid sorbent DAC system [6]. (1) Conditional (depends on the system)

The specific conditions of the system is determined by the sorbent being used. Many sorbents are proposed in literature. Some of them are discussed below:

- **Climeworks** uses cellulose fiber supported by amines as a solid filter which chemically bonds CO_2 from air and also absorbs moisture from the air aiding the plant to provide enough water for its own use. The pressure is reduced and the system is heated to about 100°C to release CO_2 [6][43].
- An amine polymer adsorbent is used by **Global Thermostat** which results in a reduction of full cycle time to less than 30 minutes. The sorbent is regenerated at 85-95°C in less than 100 seconds [44].
- **Antecy** makes use of a potassium carbonate (K_2CO_3) based composite sorbent to adsorb CO_2 at ambient conditions. The regeneration process requires reducing the system pressure and heating it up to 80-100°C [45].

- A K_2CO_3/Y_2O_3 based solid sorbent DAC system powered by wind energy was proposed by Derevschikov *et al.*[46] that regenerates at 150-250°C. Although the sorbent can be easily destroyed due to its sensitivity to high temperatures.

- Researchers have studied other sorbents and their feasibility pertaining to CO_2 capture. Kulkarni and Sholl[47] proposes a silica sorbent that can be desorbed by introducing steam at 110°C with an output of 88% CO_2. An amino based metal organic framework was also studied which utilizes a combination of vacuum and temperature swing system [48].

2.1.3. OTHER SYSTEMS

In addition to the two major types of DAC systems mentioned above, many new approaches have been suggested in the literature. Massachusetts Institute of Technology recently came up with a new technique of electro-swing reactive CO_2 capture based on the work of Voskian and Hatton[49]. Ion-exchange resins are also being used to capture CO_2 using moisture swing adsorption. Thin resin sheets are exposed to ambient air to capture CO_2. Thereafter, the sheets are moved to a closed system where CO_2 is released by addition of water [50][51].Another new solution included a conceptual design for building a nano-factory of molecular filters powered by solar energy suggested by Freitas Jr.[52].

Having gained a broader perspective and knowledgeable overview of current technologies in the field of direct air capture, the evolution of DAC system at ZEF was investigated and previous research was studied.

2.2. ZEF - DAC EVOLUTION & RESEARCH

It is important to have an overview of all the research done at ZEF in the field of DAC to be able to make a structured approach to this project. This section first discusses the step-wise evolution of DAC at ZEF and subsequently moves towards the latest findings and recommendations of previous researchers.

2.2.1. EVOLUTION

Three prototypes for a direct air capture system have been worked on by ZEF in the past. With time, ZEF evolved from the conventional batch process to a continuous DAC system.

DAC - PROTOTYPE 1

The first prototype, built by February 2018 was a small scale conventional solid sorbent DAC system which worked on a temperature-vacuum swing operation [53]. Polyethylenimine of high molecular weight was impregnated on silica to create a packed bed. The adsorber captured CO_2 and H_2O when ambient air was made to flow through the system. Subsequently, as the sorbent became saturated, the chamber was vacuumed to 0.1 bar and heated to release CO_2 and H_2O. The chamber was cooled to ambient temperature after desorption ended and the adsorption process commenced again [54]. An isometric assembly of the first prototype can be seen in the figure 2.4.

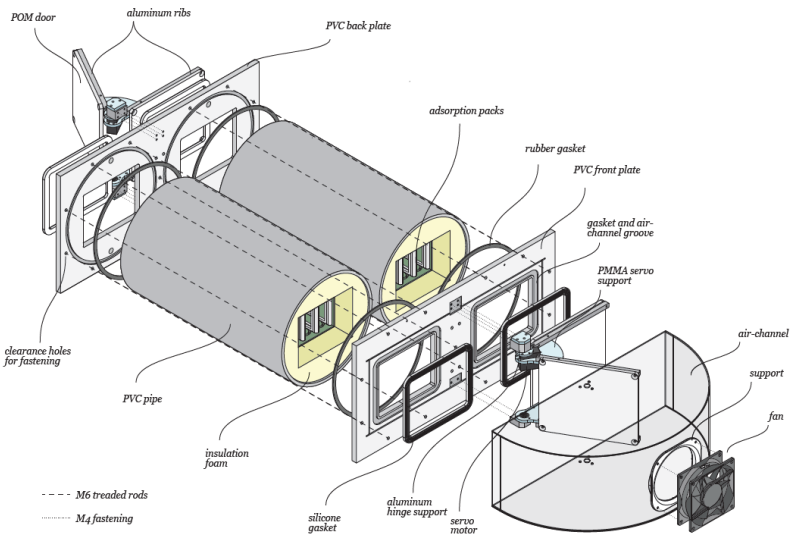

Figure 2.4: Isometric assembly of DAC prototype - 1 [8]

Due to the large volume of the unit and low cost of active carbon based sorbents, a monolithic sorbent system was proposed for the next prototype [54].

DAC - PROTOTYPE 2

The second prototype build by July 2018 utilized an active carbon monolith due to its superior and effective adsorption following previous recommendations. The monolith was impregnated with two different types of polyethylenimine of molecular weights 1200 and 10,000. Although this prototype was never properly functional due to leakages in its chambers, figure 2.5 shows a conceptual design of this prototype. The working principal of this prototype was similar to the last one and a temperature-vacuum swing process was employed [53][55].

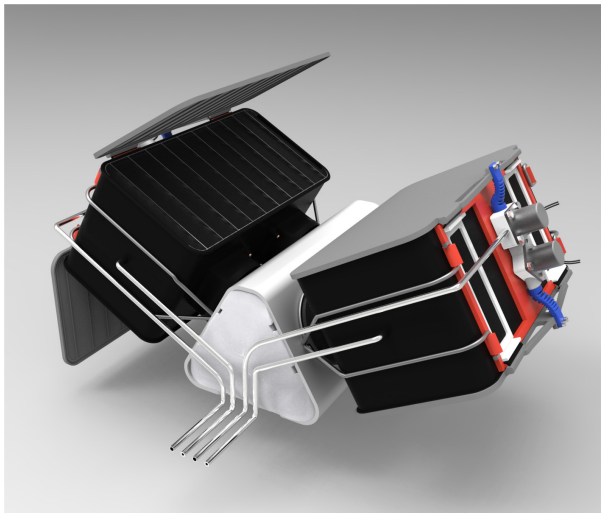

Figure 2.5: Concept design of DAC prototype - 2 [9]

Many drawbacks to this system were discovered. Apart from maintaining leak tight cham-

bers, the brittleness of active carbon made it difficult to work with and impregnate. Gravity led inhomogeneous distribution of polyethylenimine was the final nail in the coffin and this prototype was discarded [55].This paved the way to a paradigm shift in ZEF's DAC systems. Instead of a batch system with solid sorbents, ideas of a continuous DAC system with bulk amines with no support structure began to take shape.

DAC - PROTOTYPE 3

Setting themselves apart from the widely used conventional batch solid sorbent DAC systems, ZEF started researching a continuous DAC system with a separate absorber and desorber using only bulk amines. A continuous system would save energy costs due to lesser valves, reduction in power and quantity of vacuum pumps and lower energy requirements when compared to a batch system. The basic functioning of this system was similar to the previous ones apart from the fact that bulk amines were being used without silica or active carbon monolith as support. The absorber or the absorption column would consist of a vertical flow surface allowing the lean bulk amine to flow, capturing CO_2 and H_2O while an induced counter-current airflow is applied through a fan. The rich amine would flow into a desorption chamber which would be continuously vacuumed and heated resulting in release of CO_2 and H_2O and regeneration of the amine. The lean amine will then be then pumped back to the absorption column making it a continuous direct air capture process [53].

2.2.2. RESEARCH AT ZEF

This section describes the stage in which ZEF is currently in pertaining to research regarding continous absorption. Many experiments on continous absorption were done through a test setup shown in figure 2.6. The setup was 3d printed with a acrylic plate as a flow surface, a fan to ensure air flow and pumps which recirculated the sorbent on the plate to multiple runs. The results obtained by previous researchers are categorized below.

Figure 2.6: Absorption test setup used by previous teams [10]

NON-HOMOGENEOUS FLOWS

The first and foremost problem faced by these researchers was to achieve a homogeneous flow surface. It was established that the CO_2 capture was mostly on the surface of the sorbent since the absorption was diffusion limited and therefore, the requirement was a thin homogeneous surface such that CO_2/sorbent ratio by weight was maximum. This condition couldn't be reached since due to surface tension, a homogeneous layer couldn't be

achieved without manual intervention. Various hydrophilic surfaces like paper were tested as a flow surface to achieve a smaller contact angle between the sorbent and the plate. However, the results were not promising and some examples of such experiments can be seen in figures 2.7 and 2.8 which shows a drippy flow instead of a homogeneous one. All experiments done were conducted after manual intervention of flow to make it homogeneous [10].

Figure 2.7: Flow test on acrylic [10]

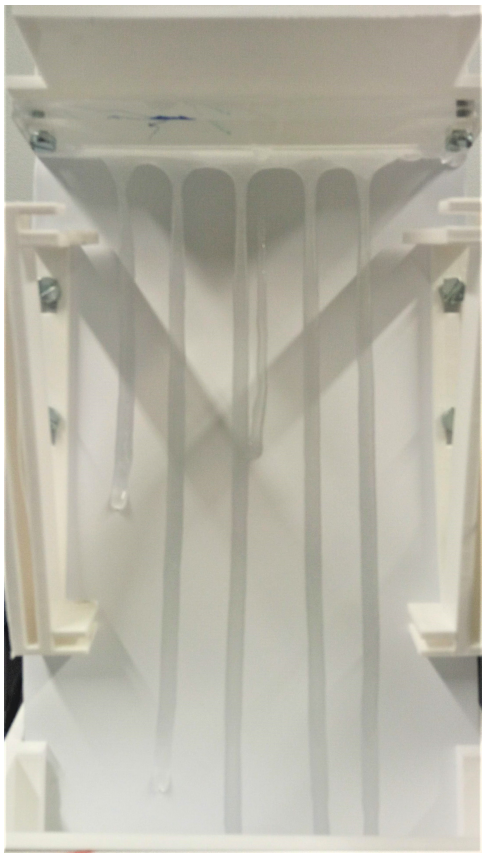

Figure 2.8: Flow test on paper [10]

LOADING DATA

It was observed that the water absorption in the sorbent was higher than CO_2. The H_2O/CO_2 ratio by weight was between 10 and 20 for PEI-600 and TEPA according to the data calculated by previous teams. A max of 2.37 $molsCO_2/kg$ of sorbent was absorbed during this absorption process when the sorbent was left on the plate for 2 weeks. However, no values for a maximum concentration of CO_2 at equilibrium could be found out. Some diffusion coefficients in the order of 10^{-12} and 10^{-10} for CO_2 and H_2O respectively were calculated by Serrano Barthe[53] which further proved that the CO_2 absorption process was diffusion limited.

MEASUREMENTS METHODS

A coulometric Karl Fischer titrator was used to find the water content from samples by dilution samples with methanol and running the titrator. Concentration of CO_2 was measured

by using a phosphoric acid test setup at TNO using the same methanol mixed samples. Fourier-transform infrared spectroscopy was used as a qualitative analysis tool to compare samples with different CO_2 and H_2O concentrations [53][10].

ADVICE/RECOMMENDATIONS

This section only contains the advice made by previous teams regarding absorption [53][10]. The recommendations are as follows:

- It was observed that the viscosity of the sorbents changed a lot during the absorption process, however, this wasn't quantified. It was recommended to conduct viscosity experiments to understand the flow process better.
- A recommendation was also made to try out different flow surfaces and profiles since a homogeneous flow was needed for a continuous absorption process.
- Mass transfer coefficients were not investigated and only the diffusion coefficients were estimated. It was recommended to find a way to calculate the absorption rate based on a mass transfer coefficient.
- A suggestion to research faster ways to measure the CO_2 and H_2O content in sorbent was made since the coulometric Karl Fischer titrator and the phosphoric acid tests were time consuming.

2.3. ABSORPTION IN FALLING LIQUID FILM

Since this thesis is done considering a falling film flow on a flat surface, some basic concepts and equations of such a mass transfer process are described in this section.

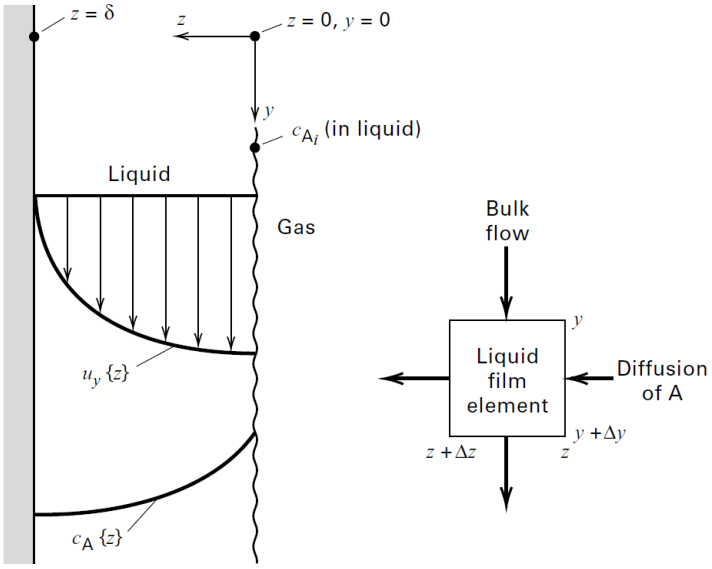

Figure 2.9: Mass transfer from a gas into a falling, laminar liquid film [11]

Figure 2.9 shows a laminar falling film while a gas A is being absorbed as the liquid flows. At any given position i, concentration of A in the liquid film is c_{Ai} whereas $c_A(z)$ is the concentration profile of A through a layer thickness of δ as shown. The velocity profile marked as

$u_y(z)$ is also shown assuming no slip boundary and is expressed as shown below in equation 2.1 where ρ is density, μ is viscosity and g is acceleration due to gravity [11].

$$u_y = \frac{\rho g \delta^2}{2\mu}[1 - \frac{z^2}{\delta^2}] \tag{2.1}$$

Considering the following boundary conditions, the total rate of absorption can be calculated.

$$c_A = c_{Ai} \quad at \quad z = 0 \quad for \quad y > 0 \tag{2.2}$$

$$c_A = c_{Ao} \quad at \quad y = 0 \quad for \quad 0 < z < \delta \tag{2.3}$$

$$\partial c_A / \partial z = 0 \quad at \quad z = \delta \quad for \quad 0 < y < L \tag{2.4}$$

Therefore the absorption rate of A from gas to the liquid film of height L and width W is given by equation 2.5.

$$n_A = \bar{u_y} \delta W (\bar{c_{AL}} - c_{Ao}) \tag{2.5}$$

where

n_A	=	total rate of absorption of A $[mol/s]$
$\bar{u_y}$	=	bulk average velocity of the liquid film $[m/s]$
δ	=	thickness of the film $[m]$
W	=	width of the film $[m]$
$\bar{c_{AL}}$	=	average concentration of A in the liquid at L $[mol/m^3]$
c_{Ao}	=	initial concentration of A at y=0 $[mol/m^3]$

An analogy to heat transfer can be made while solving mass transfer problems involving flowing liquids. Newton's law of cooling defines a heat transfer coefficient, h for the equation given below.

$$Q = hA\Delta T \tag{2.6}$$

where

Q	=	rate of heat transfer $[W]$
h	=	heat transfer coefficient $[W/m^2K]$
A	=	area for heat transfer (normal to the direction of heat transfer) $[m^2]$
ΔT	=	temperature driving force $[K]$

The same equation can be applied for mass transfer where a composition-driving force replaces ΔT. Since the above mentioned driving force can be expressed in many ways, different units for the mass transfer coefficient can be obtained. The most relevant equation for this thesis, equation 2.7 can be seen below using concentration in weight percentages as driving force (Δc_A).

$$n_A = k_c A(c_{Ai} - \bar{c_A}) \tag{2.7}$$

where

n_A = rate of absorption $[mol/s]$
k_c = mass transfer coefficient $[mol/m^2 s]$
A = area for mass transfer (normal to the direction of mass transfer) $[m^2]$
c_{Ai} = concentration at a position i [wt%]
$\bar{c_A}$ = bulk average concentration of A in the film [wt%]

Although no general name for the equation 2.7 is in use, for the purpose of this thesis, the mass transfer coefficient k_c with the units $mol/m^2 s$ is termed as the ***space-time yield*** in the chapters to come.

2.3.1. HENRY'S LAW

Henry's law states that given a constant temperature, the amount of gas that dissolves in a given type and volume of liquid is directly proportional to the partial pressure of the gas in equilibrium with that liquid [11]. In other words, the law states that the solubility of a gas in a liquid is directly proportional to the partial pressure of the gas above the liquid. The equations for Henry's law is stated below.

$$H_{gas} = \frac{p_{gas}}{c_{gas}} \tag{2.8}$$

where

H_{gas} = Henry's law constant [L.bar/mol]
p_{gas} = partial pressure of gas [bar]
c_{gas} = solubility of gas at fixed temperature in a particular solvent [mol/L]

The reason this topic is introduced is because during absorption, physical solubility plays a role. The important thing to note here is that during the absorption process, if the partial pressure of a gas decreases, the solubility of the gas will also decrease. This fact is kept in mind while doing experiments and modelling the absorption column and is stated in the following chapters.

2.3.2. FICK'S FIRST LAW OF DIFFUSION

In 1855, Fick came up with a law for diffusion which was analogous to Fourier's law of heat conduction which shows a proportionality between heat flux due to conduction and the temperature gradient. Similar to Fourier's law, Fick's first law also features a proportionality between molar flux by molecular diffusion and the concentration gradient. The law can be described by equation 2.9 [56].

$$J = -D\frac{dc_A}{dz} \tag{2.9}$$

where

J = diffusion flux $[mol/m^2 s]$
D = diffusion coefficient or diffusivity $[m^2/s]$
$\frac{dc_A}{dz}$ = molar concentration gradient $[mol/m^3.m]$

Much like Henry's law, Fick's first law of diffusion will also be used later in this thesis during the modelling of the absorption column.

2.3.3. STOKES-EINSTEIN EQUATION

For a liquid with low Reynold's number, the Stokes-Einstein equation (2.10) relates the diffusion of spherical particles with the fluid's viscosity [11][57].

$$D = \frac{k_B T}{6\pi\mu r} \tag{2.10}$$

where

D	=	diffusion constant $[m^2/s]$
T	=	temperture of the fluid $[K]$
k_B	=	Boltzmann constant $[m^2 kg/s^2 K]$
μ	=	dynamic viscosity of fluid $[kg/ms]$
r	=	radius of spherical particle $[m]$

The Stokes-Einstein equation predicts an inverse variation of liquid diffusivity with viscosity. An extension of equation 2.10 was done by Wilke and Chang[58] emperically for more concentrated solutions and the effects of temperature and viscosity were identical [11]. Both equations by Stokes-Einstein and Wilke and Chang[58] also predict that $D\mu/T$ is constant over a narrow temperature range [11].A smaller dependence of liquid diffusivity with viscosity was predicted by Hayduk and Minhas[59]. However, the consensus is that liquid diffusivity varies inversely with viscosity raised to an exponent which is less than 1 and closer to 0.5 [11][60][57].

2.4. AMINES

Industries often use alkanolamines as sorbents for the purpose of CO_2 capture. Monoethanolamine (MEA), diethanolamine (DEA), triethanolamine (TEA) and methyldiethanolamine (MDEA) are some of the most commonly used aliphatic amines used in CO_2 capture processes due to their selectivity towards CO_2 and H_2O [61]. In general, amines can be classified into primary, secondary and tertiary amines as seen in figure 2.10 where alkyl groups are represented by R, nitrogen atom by N, hydrogen atom by H and a lone pair of electrons is denoted by two dots. This classification is made based on the number of alkyl groups attached to the nitrogen atom.

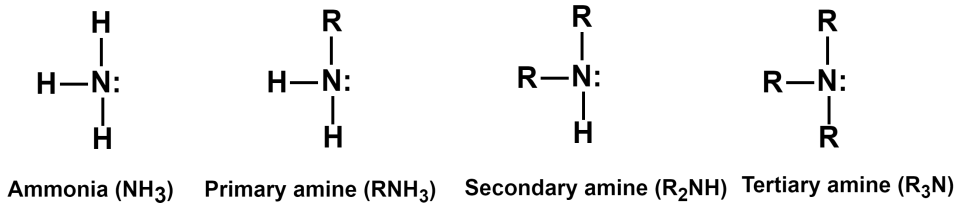

Figure 2.10: Different types of amines : primary, secondary and tertiary [12][13]

MEA is a primary amine, DEA is secondary and TEA and MDEA are tertiary amines. The structures of these frequently utilized amines can be seen in figure 2.11.

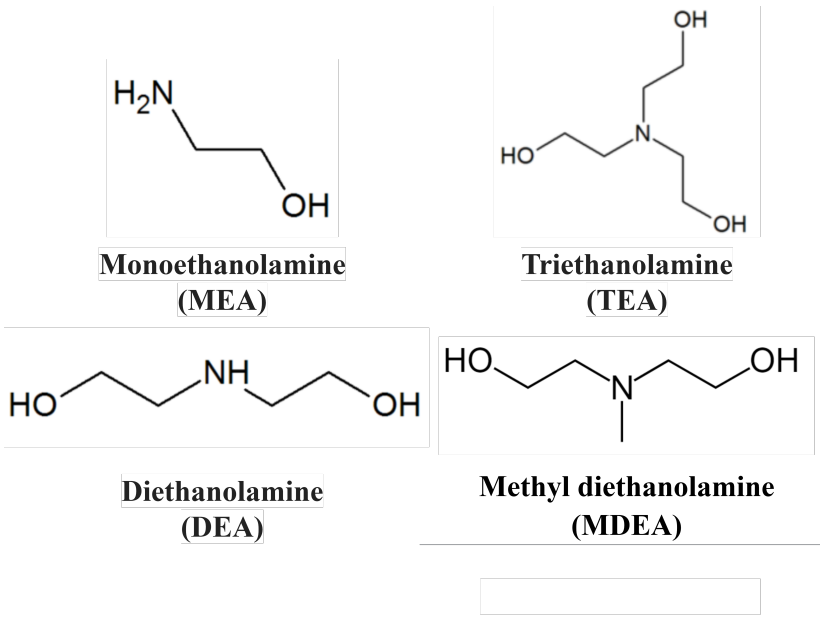

Figure 2.11: Structures of commonly used amines for the purpose of CO_2 capture [12][13]

2.4.1. ABSORPTION IN AMINES

A high affinity for CO_2 absorption can be achieved at room temperatures or lower and the absorption process can be divided into 4 steps [62].

1. Diffusion of CO_2 from bulk gas to the gas-liquid interface.
2. Physical dissolution of CO_2 in the sorbent.
3. Reaction of CO_2 with the amine being used.
4. Diffusion of the reacted CO_2 through the sorbent.

Fick's law of diffusion (2.3.2) and Henry's law (2.3.1) play an important role in step 1 and 2. The reactions of amines to capture CO_2 is can take either of both of two routes - carbamate formation and bicarbonate formation [63][14].While absorption of CO_2 different reactions can take place with primary, secondary and tertiary amines.

REACTIONS

Primary (RNH_2) and secondary (R_2NH) amines

The primary and secondary amines like MEA and DEA have a high reactivity due to formation of stable carbamates while CO_2 absorption. The reaction begins with the formation of zwitterion (reaction 2.11) which is subsequently deprotonated to form carbamate (reaction

2.12) [64][61][62][14]. An example for such a reaction for a primary amine is given below.

$$CO_2 + RNH_2 \leftrightarrow RNH_2{}^+COO^- \tag{2.11}$$

$$RNH_2{}^+COO^- + RNH_2 \leftrightarrow RNHCOO^- + RNH_3{}^+ \tag{2.12}$$

The global reaction of carbamate formation for a primary amine can be viewed as reaction 2.14. Secondary amines undergo similar reactions.

$$CO_2 + RNH_2 \leftrightarrow RNHCOO^- + RNH_3{}^+ \tag{2.13}$$

Although these reactions have a high reactivity, they have a high solvent regeneration cost and stoichiometrically, the loading of CO_2 is limited to 0.5 mol CO_2/mol amine [61][63].Greater loadings can only be achieved at higher partial pressures [61] where carbamates can be hydrolysed to form a free amine and bicarbonate [63].

$$RNHCOO^- + H_2O \leftrightarrow RNH_2 + HCO_3{}^- \tag{2.14}$$

Tertiary (R_3N) amines

Due to lack of a free proton, tertiary amines can not react with CO_2 directly to form carbamate [14]. However, due to CO_2 hydrolysis at high pressures, tertiary amines like TEA and MDEA can form bicarbonates (reaction 2.15) [65][61][14][63].

$$R_3N + CO_2 + H_2O \leftrightarrow R3NH^+ + HCO_3{}^- \tag{2.15}$$

The bicarbonate route has lower reactivity with CO_2, however, the solvent regenration cost is low and stoichiometrically, a loading of 1 mol CO_2/mol amine can be achieved [63][61][65].

Other reactions

The reactions shown above occur in the presence of amines. However, multiple other reactions occur simultaneously in presence of water. Bicarbonate formation can occur by a direct reaction of CO_2 with H_2O (reaction 2.16), carbonates can be formed if bicarbonates react with H_2O (reaction 2.17), water can split into hydronium ion and OH^- (reaction 2.18) and hydronium ion can protonate primary or secondary amines (reaction 2.19) [66][67].

$$CO_2 + 2H_2O \leftrightarrow H_3O^+ + HCO_3{}^- \tag{2.16}$$

$$HCO_3{}^- + H_2O \leftrightarrow H_3O^+ + CO_3{}^{2-} \tag{2.17}$$

$$2H_2O \leftrightarrow H_3O^+ + OH^- \tag{2.18}$$

$$RNH_2 + H_3O^+ \leftrightarrow RNH_3{}^+ + H_2O \tag{2.19}$$

Note on Carbamates vs Bicarbonates

As explained above, CO_2 can be captured by storing it as either carbamate or bicarbonate. Carbonate formation can take place in primary and secondary amines even if no water is present. However, formation of bicarbonates requires the presence of water and high pressures. In addition, studies done on MEA have resulted in a consensus that bicarbonate

formation is minimal in CO_2 loadings less that 0.4 mol CO_2/mol amine and carbamates still dominate at higher loadings [68]. Moreover, Mani *et al.*[69] has explained that formation of carbamates and bicabonates can also be explained by pH.Carbamate formation is associated with high pH solutions whereas more bicarbonates are formed when CO_2 reacts with amines and the pH lowers.

AQUEOUS AMINES - CO_2 CAPTURE

It has also been observed that aqueous solutions of amines perform better in terms of CO_2 capture capabilities compared to dry amines [70][71][72][73][74][75][65][64]. Veneman[14] collected data on CO_2 capture on dry sorbents vs wet sorbents (figure 2.12) and found out that in general, wet amines have better reaction kinetics than dry amines.

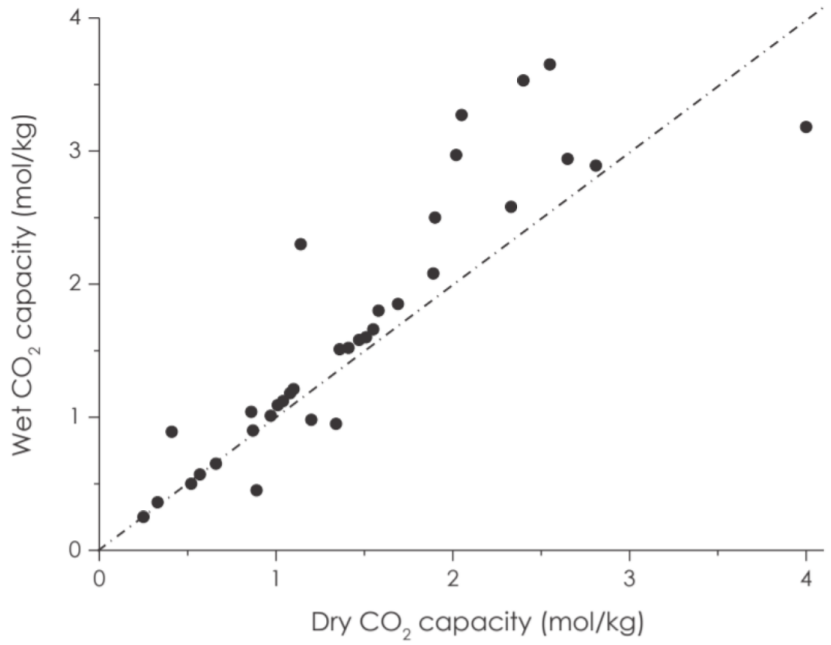

Figure 2.12: Parity plot of CO_2 capacity of supported amines tested under both dry and wet conditions. This graph doesn't specify the concentration of moisture in the supported amines and is meant to just give a qualitative perspective on dry vs wet amines [14]

Figure 2.12 qualitatively points towards the effect of water in increasing CO_2 capacity of amine. Morever, Littel *et al.*[64] argued that OH^- and other bases play an important role in the deprotonation of zwitterion in reaction 2.12 and the overall reaction rate of CO_2 capture increased as the basicity of alkanolamine increased. In conclusion aqueous amines are associated with better reaction kinetics for CO_2 capture [65][75][74][73].

GENERAL PROPERTIES

General properties of amines can be crucial in understanding the absorption process. Properties like molecular weight, density, specific heat and viscosity of MEA, DEA, TEA and MDEA can be found in table 2.1 [13].

Table 2.1: General properties of MEA, DEA, TEA and MDEA [13]

Sorbent Type	Molecular weight [g/mol]	Density at 20°C [kg/m3]	Specific heat [kJ/kgK]	Viscosity at 20°C [mPa-s]
MEA	61.08	1016	2.72	23.2
DEA	105.14	1091.2 (30°C)	2.73	389 (30°C)
TEA	149.19	1124.8	2.33	930
MDEA	119.7	1038-1041	1.72	101

2.4.2. VISCOSITY OF AMINES

Table 2.1 shows the viscosity of most commonly used pure amines for the absorption of CO_2. According to literature the viscosity of amines varies with temperature and composition. Since viscosity has a inverse relation with diffusivity, it is an important fluid property. Thus, this section analyses the effect of these factors on viscosity of MEA ,DEA and MDEA.

EFFECT OF TEMPERATURE

The viscosity of amines is expected to decrease exponentially with increasing temperatures. Figure 2.13 shows the viscosity changes of pure MEA, DEA and MDEA with temperature variations [76][77].

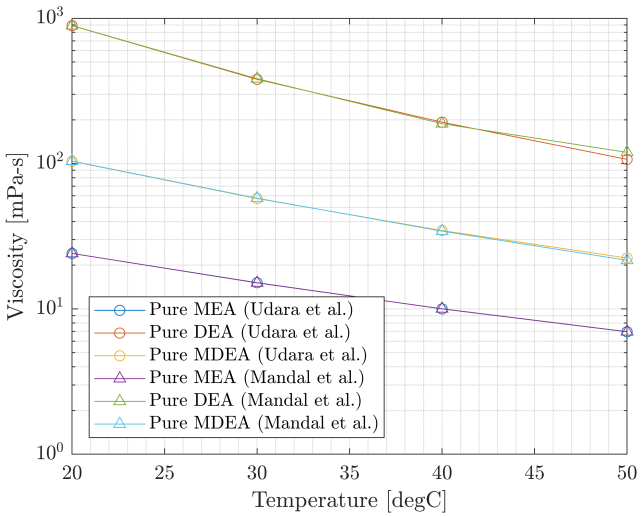

Figure 2.13: Viscosity of MEA, DEA and MDEA plotted against increasing temperatures

EFFECT OF VARYING WATER CONCENTRATIONS

Amines exhibit an interesting effect relating to viscosity as water concentration is varied. Figure 2.14 shows the viscosity of MEA and MDEA with varying concentrations of water [77]. It can be seen that the viscosity initially increases with increasing water concentration and then decreases continuously.

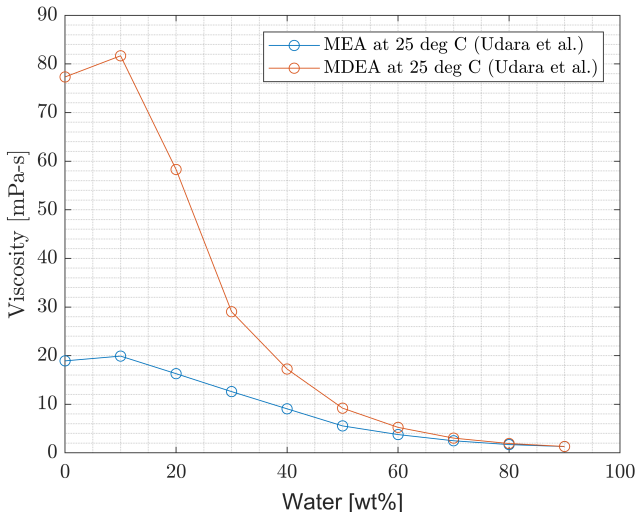

Figure 2.14: Viscosity of MEA and MDEA plotted against increasing water concentrations at 25°C

Similar observations were made by L Fernandes and R Figueiredo[15] on liquid ammonia-water mixtures where it was observed that relation between viscosity and water composition often exhibited a point of maximum or minimum or both. This was explained by considering aqueous solutions of amines as a mixture of dissimilar polar species which can build or break hydrogen bonds. The maximum peak was associated with formation of hydrogen bonds within the solution. Figure 2.15 shows the viscosity of a liquid ammonia-water system at 10°C with varying ammonia mass fractions. Similar behavior was seen in water-methanol and water-ethanol systems [78].

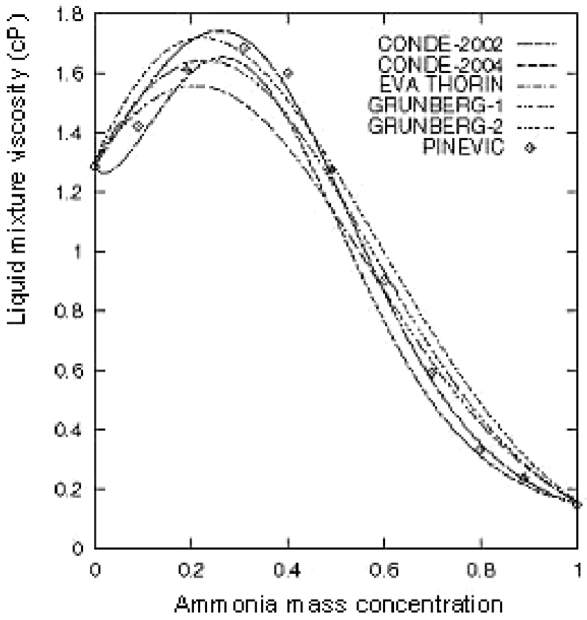

Figure 2.15: Experimental models used to predict viscosity of liquid ammonia-water system at 10°C collected and plotted by L Fernandes and R Figueiredo[15]

EFFECT OF VARYING CO_2 CONCENTRATIONS

Zhang *et al.*[79] measured the viscosity of MEA at different water concentrations with different loadings of CO_2. One such example can be seen in figure 2.16 where MEA (70% H_2O) at 25°C is loaded with CO_2 and the viscosity is measured at different loadings. It is observed that the viscosity of MEA increases with increase in the CO_2 content.

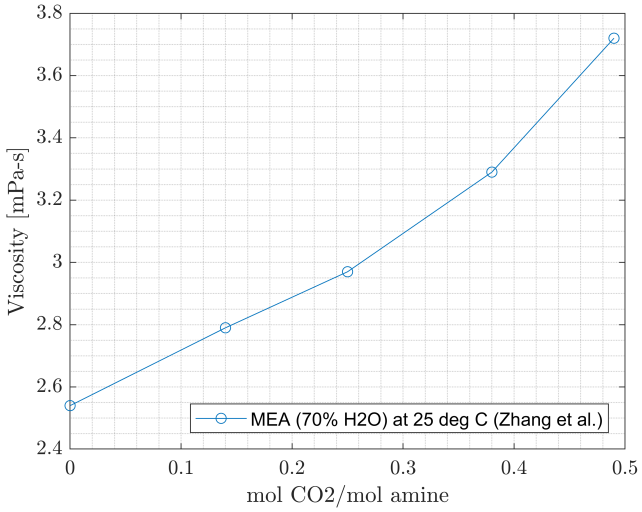

Figure 2.16: Viscosity of MEA (70% H_2O) with different CO_2 loadings

2.4.3. HEAT OF ABSORPTION

An important aspect of direct air capture is the heat of absorption (ΔH_{abs}) of CO_2 and H_2O. It directly relates to the regenerative energy costs required to replenish the amines for continuous absorption. Absorption in the case of CO_2 and H_2O is exothermic, and energy is released while in order to desorb, energy needs to be supplied in order to break the chemical bonds and release the captured substance, making it endothermic.
The heat of absorption of CO_2 is a function of loading (CO_2/amine) and temperature [80][81] and is considered complex since it is different in different types of amines. It is the sum of the following reaction enthalpies [82]:

1. Physical dissolution of CO_2
2. Amine protonation
3. Carbamate formation
4. Dissociation of water
5. Deprotonation of carbonic acid
6. Other minute contributions

It is observed that the reaction enthaply of amine protonation is the highest contributor to the enthalpy of absorption [82]. Some of the values of heat of absorption of CO_2 averaged on various loading are mentioned in the table 2.2 below. It should be noted that various

data on different temperature ranges was also available, however, only the values at lower temperature as close as possible to room temperature have been indicated since absorption process in this thesis would occur at room temperatures.

Table 2.2: Heat of absorption [$kJ/molCO_2$] of commonly used amines in aqueous solutions.

Amine	Heat of absorption [kJ/mol CO2]
MEA (30% aqueous)	-75 (@40 °C) [81], -70 (@ 40 °C) [80]
MEA (70% aqueous)	-70(@40 °C) [82]
MDEA (70% aqueous)	-50(@ 40 °C) [82]
DEA (90% aqueous)	-68 (@ 25 °C) [82]

Similarly, water would have its own heat of absorption which would be a sum of its latent heat, physical dissolution and any interactions that might occur within the amine such as formation or breaking of hydrogen bonds. Although the latent heat of water is dependent on temperature, Table 2.3 shows the average latent heat of water at room temperature.

Table 2.3: Average latent heat [$kJ/molH_2O$] of water

Molecule	Average latent heat [kJ/mol H_2O]
H_2O	40.8 [83]

Therefore, if the enthalpy of absorption and the rate of absorption is known, the overall heat transfer can be calculated as shown in equations 2.20 and 2.21.

$$Q_{abs,CO_2} = \dot{m}_{CO_2}.\Delta H_{abs,CO_2} \tag{2.20}$$

$$Q_{abs,H_2O} = \dot{m}_{H_2O}.\Delta H_{abs,H_2O} \tag{2.21}$$

where

Q_{abs,CO_2} = Heat transfer due to absorption of CO_2 [W]
Q_{abs,H_2O} = Heat transfer due to absorption of H_2O [W]
$\dot{m}_{CO_2}$ = rate of absorption of CO2 [mols CO_2 /sec]
$\dot{m}_{H_2O}$ = rate of absorption of H2O [mols H_2O /sec]
$\Delta H_{abs,CO_2}$ = heat of absorption of CO_2 [J/mol CO_2]
$\Delta H_{abs,H_2O}$ = heat of absorption of H_2O [J/mol H_2O]

2.5. PEI-600 AND TEPA

Before, discussing the next steps, the general information available on the relevant sorbents, PEI-600 and TEPA are shown.

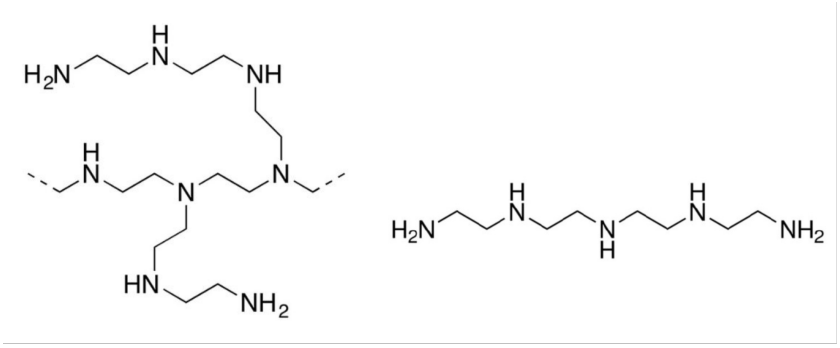

Polyethylenimine(PEI) **Tetraethylenepentamine(TEPA)**

Figure 2.17: Molecular structures of PEI-600 and TEPA [16][17][18]

It can be seen from figure2.17 that PEI-600 is a branched polymer that consists of primary, secondary and tertiary amines whereas TEPA is a linear polymer made up of only primary and secondary amines. Table 2.4 shows the general properties of PEI-600 and TEPA which can be compared to properties of MEA, DEA, TEA and MDEA shown in table 2.1.

Table 2.4: General properties of PEI-600 and TEPA

Sorbent Type	**Molecular weight [g/mol]**	**Density at 20 deg C [kg/m3]**	**Specific heat [kJ/kgK]**	**Viscosity at 20 deg C [mPa-s]**
PEI-600	600 [18]	1029-1038 [18]	2.44 [84]	500-2500 [18]
TEPA	189.31 [17][16]	993 [16], 991[17]	1.89 [17]	23.4[17],80[16]

In addition to the general properties mentioned above, table 2.5 presents some data on the heat of absorption of CO_2 in PEI-600 and TEPA. These values vary with different loading and temperatures and thus, an average value is presented.

Table 2.5: Heat of absorption of PEI-600 and TEPA [kJ/mol CO_2]

Amine	**Heat of absorption [kJ/mol CO2]**
PEI-600 (impregnated on silica)	-80 [85] , -50 [72] , -95 [84]
TEPA (liquid amine)	-85 [86]
TEPA (impregnated on silica)	-50 [86]

2.6. CONCLUSION

Based on the data available on PEI-600 and TEPA, previous research at ZEF and literature, the following points can be concluded which indicate the steps needed to be taken to proceed further with this thesis project.

- Based on recommendations of previous teams at ZEF and literature survey, it is evident that information on viscosity of PEI-600 and TEPA and effect of temperature and composition of amine is not readily available. Since viscosity is closely linked

with diffusivity and CO_2 and H_2O both have impacts on viscosity, a set of preliminary experiments will be done on viscosity analysis before moving ahead with this thesis.

- Literature has also pointed out that aqueous amines have better CO_2 capture capabilities. Therefore, the effects of water will be be researched along with viscosity analysis as the second preliminary experiment.

- Previous research at ZEF (2.2.2) indicates that a homogeneous layer of sorbent is difficult to achieve on a flat plate. Therefore, an alternative flow profile can be suggested. Instead of sorbents flowing on a plate, a rectangular channel can be used such that the sorbent connects to both the side walls and the flow is homogeneous throughout the channel. Many such channels can be milled on a plate to achieve the required surface area for absorption. It is decided to go ahead with a channel flow and for the purpose of this thesis, flow through only one channel will be considered. The data obtained will be extrapolated to multiple channels.

- In order to save time to be able to perform multiple experiments on a channel flow setup, the need to find a faster method for calculating the concentration of CO_2 and H_2O is crucial. Although, spectroscopy through FTIR is mostly used for qualitative analysis, Smal *et al.*[87] utilized a TG-FTIR to calculate the concentrations of CO_2 and H_2O by connecting it to a gas stream and calibrating it. Their work shows that given enough samples, there are ways to predict concentrations based on a good calibration. Therefore, this method will be analysed further since it has a potential of making experiments faster and saving valuable time by bypassing Karl Fischer titrations and phosphoric acid tests.

- Finally, based on literature and recommendations, this thesis would try to find mass transfer coefficients (space-time yield) to characterize absorption in bulk amine flows.

3

PRELIMINARY INVESTIGATION

This chapter consists of methodologies for sample preparation in order to perform preliminary investigation discussed in 2.6. After each of those experiments, the results are discussed in detail.

3.1. SAMPLE PREPARATION METHODOLOGY

To conduct any experiment and observe effects of different CO_2 and H_2O concentrations, it would be necessary to have multiple samples of PEI-600 and TEPA with varying CO_2 and H_2O concentrations. Therefore, it was decided to make a master batch of PEI-600 and TEPA. Since, literature showed that amines like MEA and DEA absorb CO_2 at a higher rate with water present, it was decide to pre-mix the sorbents with 40% H_2O prior to loading with CO_2. The method of loading these samples in described in section 3.1.1.

3.1.1. LOADING TEST SETUP

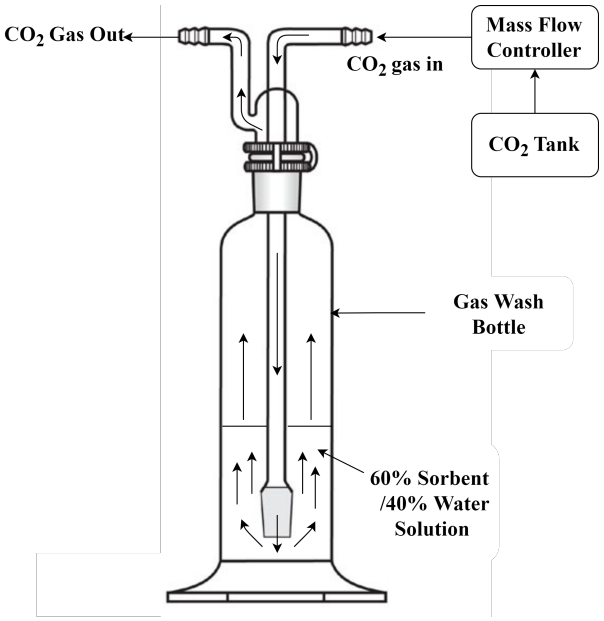

Figure 3.1: Schematics of setup used to load CO_2 into sorbent

Figure 3.1 shows a schematic of the setup used for loading CO_2 into aqueous solution of sorbents to make master batches of PEI-600 and TEPA. A mass flow controller is used to control the CO_2 gas flow coming from the CO_2 tank. For the purpose of loading, the mass flow controller doesn't play a major role. However, it was observed that the sorbent solution starts frothing when CO_2 is bubbled through it and therefore, a mass flow controller was used to make sure that a low mass flow of CO_2 can be maintained so the froth doesn't overflow out of the gas wash bottle. A value of 15 l/hr was chosen as the mass flow rate of CO_2. The CO_2 gas passed through the mass flow controller and entered the gas wash bottle as shown in figure 3.1 and bubbled through the aqueous sorbent solution. Some of the CO_2 was absorbed in the sorbent solution and the rest flowed out from the outlet depicted in the figure. This process was done for 30 minutes and it was observed that the aqueous sorbent solution became very viscous. After making the CO_2 loaded master batch, concentration of CO_2 and H_2O in the solution was to be determined.

3.1.2. MEASUREMENT OF CO_2 AND H_2O CONCENTRATION

After the master batch was prepared, it was well mixed with a magnetic stirrer on a magnetic hotplate to ensure homogeneous concentration of CO_2 and H_2O through out the master batch. The CO_2 concentration was determined using a phosphoric acid test setup at TNO and a coulometric Karl Fischer titrator borrowed from TNO was used to measure the H_2O concentration.

PHOSPHORIC ACID TEST

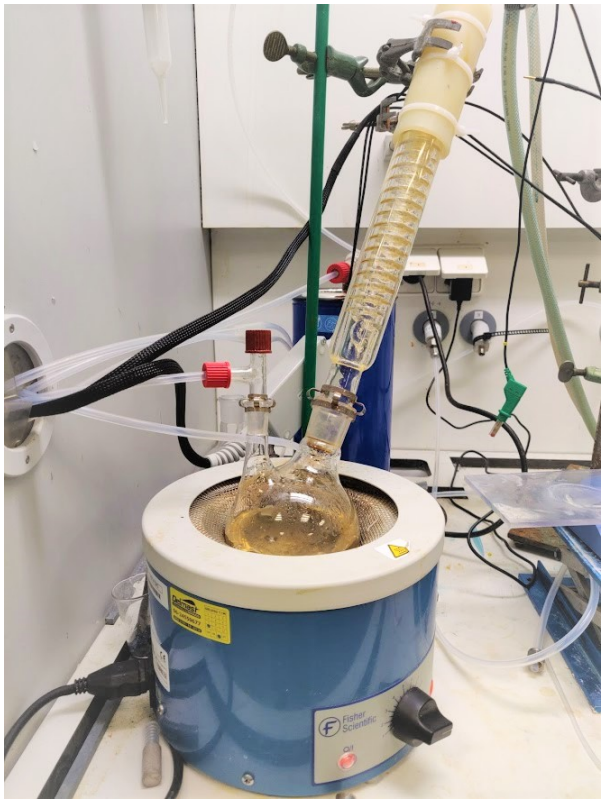

Figure 3.2: Phosphoric acid test setup at TNO

To calculate the concentration of CO_2 in the master batch, a small sample was collected from the master batch and mixed with methanol in the ratio 1:10 (sorbent solution : methanol) by weight. This was done because the maximum concentration of CO_2 that could be measured using the setup shown in figure 3.2 was 3% CO_2 by weight per sample. Therefore it was necessary to dilute the sample and since amines are soluble in methanol, it was chosen as the diluting agent. A 5 ml solution diluted with methanol was injected in the setup, the hot phosphoric acid broke down the amines releasing CO_2 and H_2O in gas form. These gases were continuously flushed with Nitrogen, the water was condensed and the rest was made to pass through a calibrated CO_2 analyzer which calculated the mass flow rate of CO_2 gas which was converted to total weight of CO_2 and displayed on the user interface made by TNO. The least count of this experiment was 10^{-9} gram. For more information on phosphoric acid test, see appendix A.2.

COULOMETRIC KARL FISCHER TITRATOR

Figure 3.3: C20 coulometric Karl Fischer titrator

The water concentration was measured using a C20 coulometric Karl Fischer titrator shown in figure 3.3. Since the data sheet suggested to have a water concentration of less than 1% by weight in the samples being titrated for optimum water concentration determination, the same methanol diluted samples were used [21]. Samples of about 0.1 ml were titrated in the machine and the result was shown on the screen shown in the figure. The least count of this method was 10^{-6} gram. More information regarding this method can be found in appendix A.1.

3.1.3. PREPARATION OF NEW SAMPLES

After the concentration of the CO_2 and H_2O in the master batch was measured, the samples were diluted with pure sorbents, mixed using magnetic stirrers and put in a sonic bath to remove bubbles to achieve varying concentrations needed for experiments. Subsequently, each new sample was again measured for accurate CO_2 and H_2O concentrations using the phosphoric acid setup and Karl Fischer titrator. The new samples with varying concentrations can be seen in tables 3.1 and 3.2

Table 3.1: Prepared samples of PEI-600 with varying concentrations of CO_2 and H_2O

Sorbent	H2O (wt%)	CO2 (wt%)
PEI-600	0	0
PEI-600	10	0
PEI-600	20	0
PEI-600	30	0
PEI-600	40	0
PEI-600	10.23	2.6
PEI-600	10.06	4.1
PEI-600	20.21	2.41
PEI-600	20.06	4.1
PEI-600	29.6	3
PEI-600	30.5	5.63
PEI-600 Master Batch	**33.22**	**13.53**

Table 3.2: Prepared samples of TEPA with varying concentrations of CO_2 and H_2O

Sorbent	H2O (wt%)	CO2 (wt%)
TEPA	0	0
TEPA	10	0
TEPA	20	0
TEPA	30	0
TEPA	40	0
TEPA	10.32	2.32
TEPA	15.55	5.17
TEPA	10.25	3.2
TEPA	20.195	2.46
TEPA	20.25	3.2
TEPA	30	1.56
TEPA	30	4
TEPA	30	5.725
TEPA	30	9.43
TEPA Master Batch	**31.27**	**16.03**

3.2. VISCOSITY MEASUREMENTS

Figure 3.4: Contraves low shear 40 rheometer

Following the advice of previous teams at ZEF (2.2.2), the first preliminary experiments done were to calculate the viscosity of the samples shown in tables 3.1 and 3.2. A Contraves low shear 40 rheometer shown in figure 3.4 was used to conduct viscosity measurements on the samples prepared. Around 5 ml of each sample was used for one measurement. Each sample was tested for viscosity at 10, 20, 30 and 40 degree Celsius. However, after correcting for error in temperature readings, these values were corrected to 11, 20, 29.2 and 38 degree Celsius respectively. At each temperature, the sample was tested for different deformation rates ranging from 0.01 to 1 $radian/second$. In addition, negative deformation rates (inverse rotation) were also applied to check for any shear thinning or thickening effects. However, this process was done with all the samples of both PEI-600 and TEPA and all of them were found to be Newtonian. More information on conducting experiments with this rheometer can be found in A.4. The viscosity values obtained from these experiments are tabulated in table 3.3.

Table 3.3: Viscosity data of samples of PEI-600 and TEPA at different temperatures

Concentration of sorbent			Viscosity (pa-s)			
Sorbent	**H2O (wt%)**	**CO2 (wt%)**	**11 deg C**	**20 deg C**	**29.2 deg C**	**38 deg C**
PEI-600	0	0	6.71	2.774	1.351	0.6945
PEI-600	10	0	10.76	4.29	1.815	0.9335
PEI-600	20	0	11.28	4.076	1.651	0.8051
PEI-600	30	0	6.145	2.208	0.8966	0.4407
PEI-600	40	0	2.611	1.009	0.4377	0.2101
PEI-600	10.23	2.6	58.54	20.18	7.746	3.325
PEI-600	10.06	4.1	182.1	58.01	21.49	8.794
PEI-600	20.21	2.41	37.14	12.22	4.497	1.901
PEI-600	20.06	4.1	83.1	26.46	8.887	3.604
PEI-600	29.911	1.5375	10.81	3.071	1.542	0.6658
PEI-600	29.6	3	17.47	6.045	2.379	1.093
PEI-600	30.5	5.63	45.23	14.28	5.041	2.129
PEI-600	33.22	13.53	82.24	28.07	11.39	5.317
TEPA	0	0	0.1981	0.09403	0.04877	0.02723
TEPA	10	0	0.4947	0.2227	0.1144	0.06534
TEPA	20	0	0.9484	0.3815	0.1822	0.09629
TEPA	30	0	0.9815	0.3836	0.1744	0.09114
TEPA	40	0	**Crystal**	0.2005	0.09762	0.05473
TEPA	10.32	2.32	1.84	0.7826	0.363	0.1811
TEPA	15.55	5.17	11.3	3.876	1.525	0.6904
TEPA	10.25	3.2	3.114	1.283	0.5714	0.2774
TEPA	20.195	2.46	2.645	1.008	0.4249	0.2016
TEPA	20.25	3.2	4.156	1.54	0.6433	0.2986
TEPA	30	1.56	1.417	0.577	0.2583	0.1273
TEPA	30	4	2.185	0.8728	0.3755	0.1855
TEPA	30	5.725	4.704	1.764	0.7335	0.3508
TEPA	30	9.43	17.35	5.438	2.102	0.9252
TEPA	31.27	16.03	41.08	14.44	5.779	2.544

3.2.1. VALIDATION OF RESULTS

Although the values for viscosity for loaded samples of PEI-600 and TEPA are not readily available in the literature, a data-sheet on epomin (industrial grade PEI-600) was found with a graph representing viscosity of PEI-600 with varying concentration of water and no CO_2. The comparison in the viscosity of PEI-600 (epomin data-sheet) and PEI-600 can be seen from figures 3.5 and 3.6 which were put to a common scale. Although the graph for Epomin did not indicate clear values, it was observed that the trend in viscosity was similar with almost identical values. Since the duplos for the experiments done in this thesis yielded identical values, the data from figures 3.5 and 3.6 were considered sufficient to validate the experimental data from Contraves low shear 40 rheometer. **Note: Unfortunately, only the graph representing the viscosity of epomin could be found and not the actual data set.**

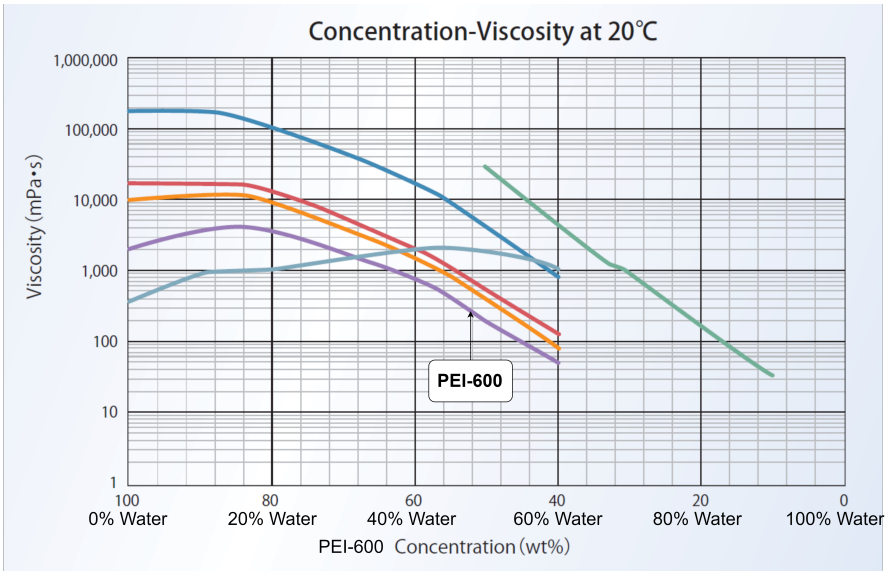

Figure 3.5: Viscosity of Epomin PEI-600 with varying water concentration [19]

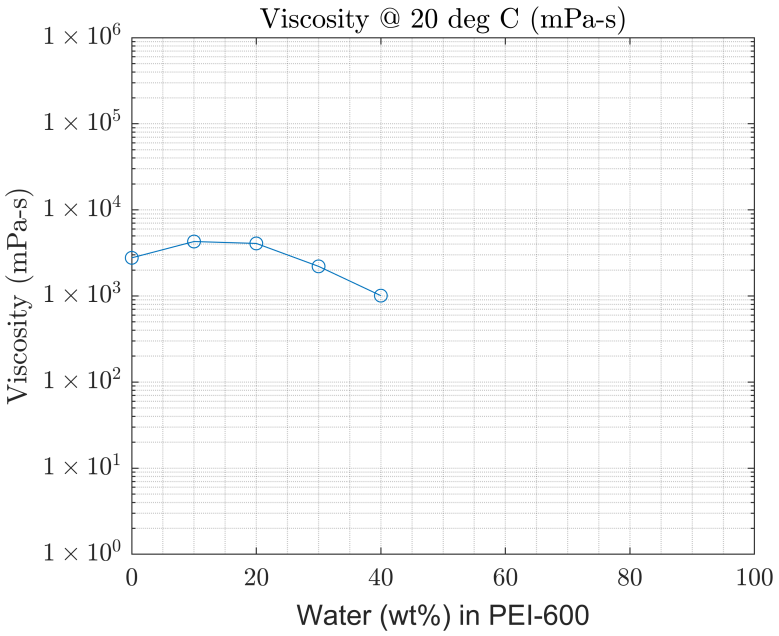

Figure 3.6: Viscosity of PEI-600 (this thesis) with varying concentration of water

3.2.2. EFFECT OF VARYING TEMPERATURE

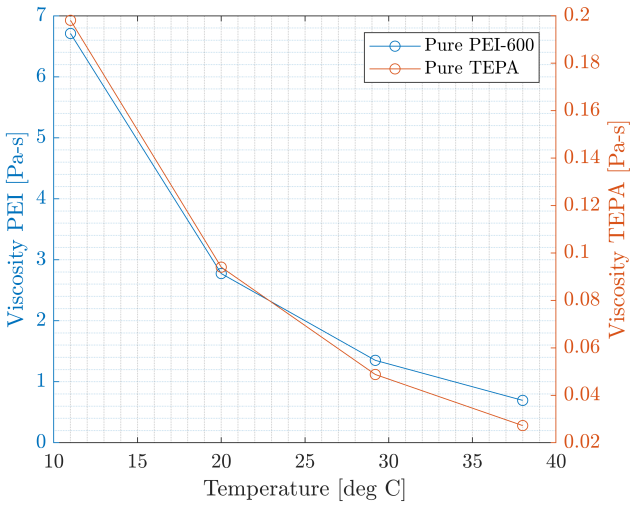

Figure 3.7: Viscosity of pure PEI-600 and TEPA with varying temperature

The viscosity of both PEI-600 and TEPA drops exponentially with temperature increase as seen in figure 3.7.

EFFECT OF VARYING H_2O CONCENTRATION

This result only applies if the samples measured have no CO_2 and only H_2O concentration is varied. It can be seen from figure 3.8 that as the water concentration increases, the viscosity increases till a point and then drops. This is true for both PEI-600 and TEPA. However, PEI-600 has its maximum viscosity at lower H_2O% than TEPA.

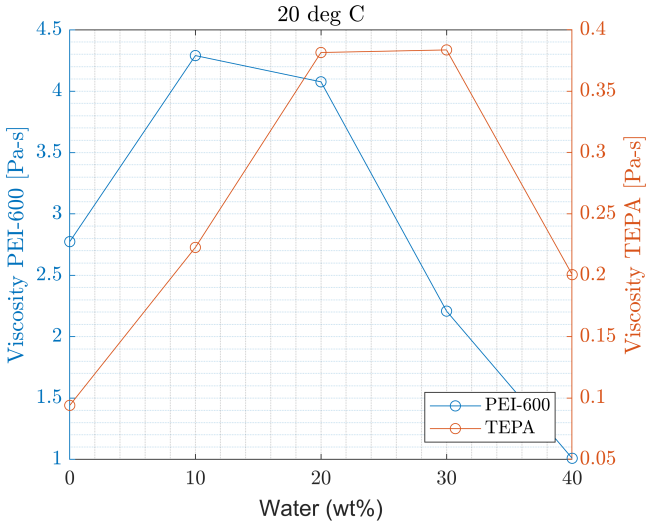

Figure 3.8: Viscosity of PEI-600 and TEPA with varying concentration of water at 20°C

3.2.3. EFFECT OF VARYING CO_2 CONCENTRATION

If the concentration of CO_2 is varied keeping the water concentration constant at 10%, 20% and 30%, we see a trend in viscosity as shown in figures 3.9 and 3.10. It is observed that the viscosity rise seems to be exponential with increasing CO_2 concentration for both PEI-600 and TEPA. In addition, when observed carefully, for PEI-600, this exponential rise is highest for 10% water and lowest for 30%. Observing figure 3.8 again, it correlates with highest viscosity at 10% water and lowest viscosity at 30% water. This trend is similar in TEPA as well.

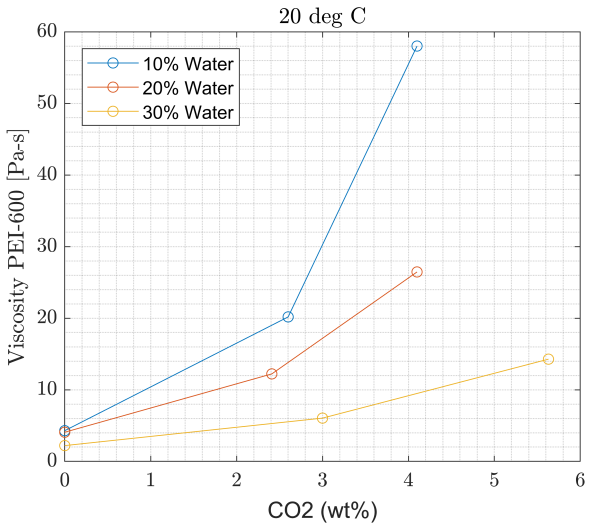

Figure 3.9: Viscosity of PEI-600 at 20°C with varying concentration of CO2 keeping water concentration constant

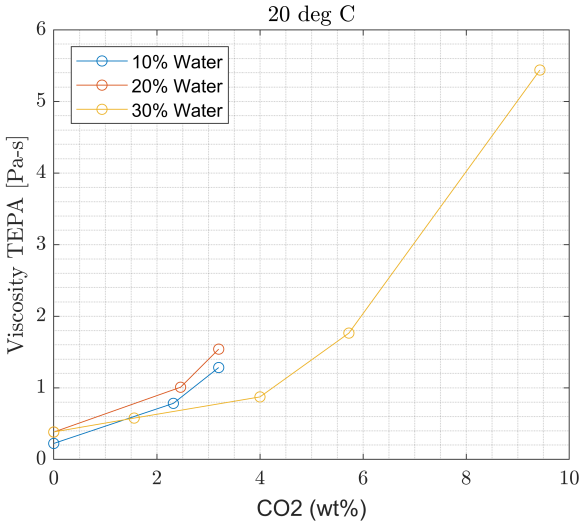

Figure 3.10: Viscosity of TEPA at 20°C with varying concentration of CO2 keeping water concentration constant

3.2.4. OTHER OBSERVATIONS

- In general, the viscosity of PEI-600 samples are much higher than that of TEPA samples. Taking an example of pure PEI-600, it is rougly 30 times more viscous than pure TEPA. Based on section 2.3.3 and this viscosity data, the diffusivity of TEPA is much higher than PEI-600.
- TEPA with 40% water and no CO_2 crystallizes at 11°C.
- Similar to literature on MEA,DEA and MDEA in section 2.4.2, viscosity of PEI-600 and TEPA decreases with increasing temperatures.
- The viscosity of both PEI-600 and TEPA increases initially with increasing water concentration, reaches a maximum and eventually decreases and water concentration is increased further. This trend is in agreement with literature studied on commonly used amines (figures 2.14 and 2.15). This effect can be associated with formation of hydrogen bonds with water and amine as discussed in section 2.4.2.
- Effects of change in CO_2 concentration also seem to be in accordance with literature (figure 2.16). The viscosity increase drastically with increase in CO_2 concentration for both PEI-600 and TEPA.
- An important observation comes from comparing the viscosity of PEI-600 and TEPA with commonly used MEA, DEA, TEA and MDEA. Comparing values with table 2.1, it can be seen that the viscosity of PEI-600 at 20°C is an order higher than TEA, which is the most viscous amine mentioned in the table whereas TEPA's viscosity is of the same order as MEA, which has the least viscosity among the commonly used amine mentioned. Considering the Stokes-Einstein equation in 2.3.3, it can be inferred qualitatively that TEPA's diffusivity is much higher than that of PEI-600.

3.2.5. MULTIPLE REGRESSION MODEL

Now that the trends in viscosity have been observed and all the viscosity experiments completed, these data can be fitted into a function using multiple regression such that the function takes temperature, CO_2 concentration and H_2O concentration as inputs and calculates the corresponding viscosity. This regression strategy can be divided into the following steps:

STEP-1

The idea behind this multiple regression was to get a final function like the function shown in equation 3.1.

$$\mu(CO_2, H_2O, T) = A_T(CO_2, H_2O) \exp^{-B_T(CO_2, H_2O)[T-25]} \tag{3.1}$$

where

μ	=	viscosity of sorbent [Pa-s] which depends on temperature [deg C], CO2 [wt%] and H2O [wt%]
A_T	=	a constant dependent on CO2 [wt%] and H2O [wt%]
B_T	=	a constant dependent on CO2 [wt%] and H2O [wt%]
T	=	temperature of sorbent [deg C]

Therefore, each sample with respective CO_2 and H_2O concentration was plotted against temperatures 11, 20, 29.2 and 38 °C since the viscosity was measured at these values. They were exponentially fit with a [T-25] offset since the mean of the temperatures was around 25°C. This was done separately for PEI-600 and TEPA. The coefficients A_T and B_T were obtained and can be seen in tables 3.4 and 3.5.

Table 3.4: A_T and B_T for PEI-600

H20 [wt%]	CO2 [wt%]	BT	AT
0	0	0.08272	1.92945
10	0	0.08919	2.815798
20	0	0.09809	2.582989
30	0	0.09843	1.400083
40	0	0.09132	0.661428
10.23	2.6	0.1036	12.3558
10.06	4.1	0.111	34.3795
20.21	2.41	0.1083	7.304018
20.06	4.1	0.1129	15.26859
29.911	1.5375	0.1137	1.95179
29.6	3	0.1025	3.744545
30.5	5.63	0.1126	8.338737

Table 3.5: A_T and B_T for TEPA

H2O [wt%]	CO2 [wt%]	BT	AT
0	0	0.07805	0.06606
10	0	0.08208	0.1557
20	0	0.09413	0.2524
30	0	0.09814	0.2472
40	0	0.07481	0.1375
10.32	2.32	0.09101	0.5127
15.55	5.17	0.1143	2.274
10.25	3.2	0.09496	0.8215
20.195	2.46	0.1031	0.6227
20.25	3.2	0.1059	0.9411
30	1.56	0.09565	0.37
30	4	0.09835	0.5498
30	5.725	0.1048	1.081
30	9.43	0.1232	3.084

STEP-2

As seen in equation 3.1, A_T and B_T are functions of concentration of CO_2 and H_2O. Therefore, they are individually plotted against CO_2 and H_2O concentration in a 3d plot and are fitted using a polynomial function. Figures 3.11 and 3.12 show the A_T and B_T values plotted against CO_2 and H_2O.

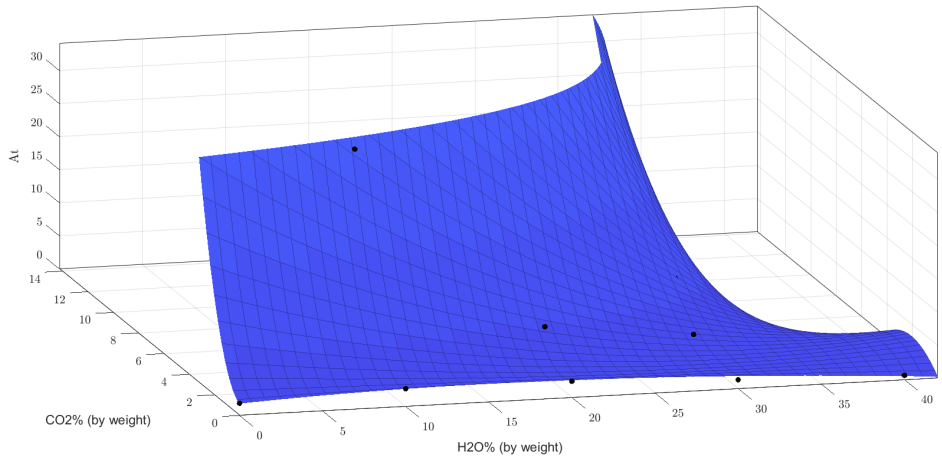

Figure 3.11: A_T values for PEI-600 varying with different CO_2 and H_2O concentrations

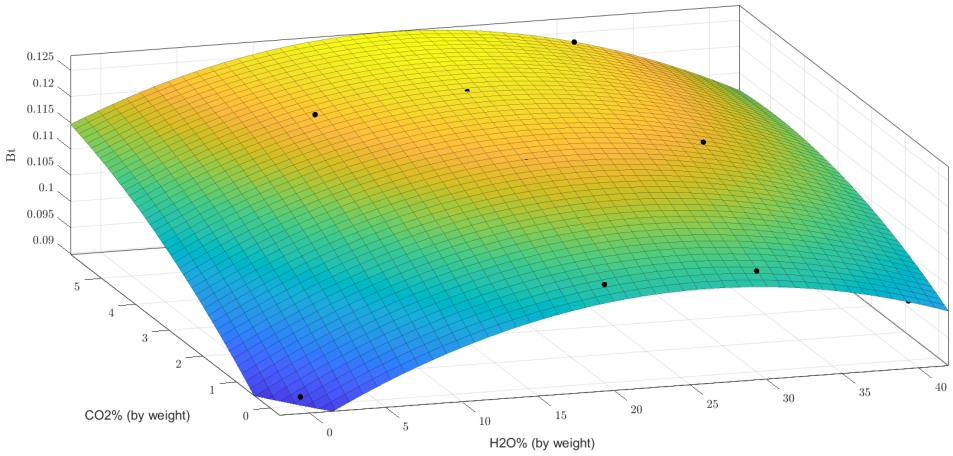

Figure 3.12: B_T values for PEI-600 varying with different CO_2 and H_2O concentrations

The H_2O concentration was denoted by x and CO_2 concentration by y. For PEI-600, A_T was best fit using a polynomial which was third degree in x and second degree in y. B_T was best fit using a second order polynomial in both x and y. The equations of A_T and B_T are shown below.

$$A_T = p00 + p10 * (x-25) + p01 * (y-2) + p20 * (x-25)^2 + p11 * (x-25) * (y-2) + p02 * (y-2)^2 + p30 * (x-25)^3 + p21 * (x-25)^2 * (y-2) + p12 * (x-25) * (y-2)^2 \quad (3.2)$$

$$B_T = b00 + b10 * (x-25) + b01 * (y-2) + b20 * (x-25)^2 + b11 * (x-25) * (y-2) + b02 * (y-2)^2 \quad (3.3)$$

where

p00	=	2.516	b00	=	0.1163
p01	=	1.656	b01	=	0.003672
p02	=	0.7825	b02	=	-0.0002347
p10	=	-0.1933	b10	=	-0.0002067
p11	=	-0.2289	b11	=	-0.0001029
p12	=	-0.08512	b20	=	-2.889e-05
p20	=	0.01296			
p21	=	0.008165			
p30	=	2.37e-05			

The equations 3.2 and 3.3 can be now used in equation 3.1, which defines an equation for PEI-600 to calculate viscosity taking temperature and concentrations of CO_2 and H_2O as inputs.
For TEPA, A_T was best fit using a polynomial which was third degree in x and second degree in y. B_T was best fit using a second order polynomial in x and first order in y.Figures 3.13 and 3.14 show the A_T and B_T values plotted against CO_2 and H_2O.

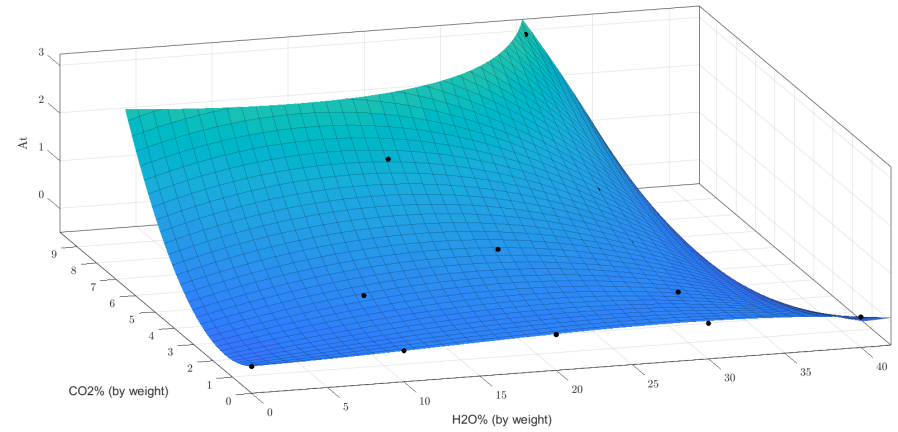

Figure 3.13: A_T values for TEPA varying with different CO_2 and H_2O concentrations

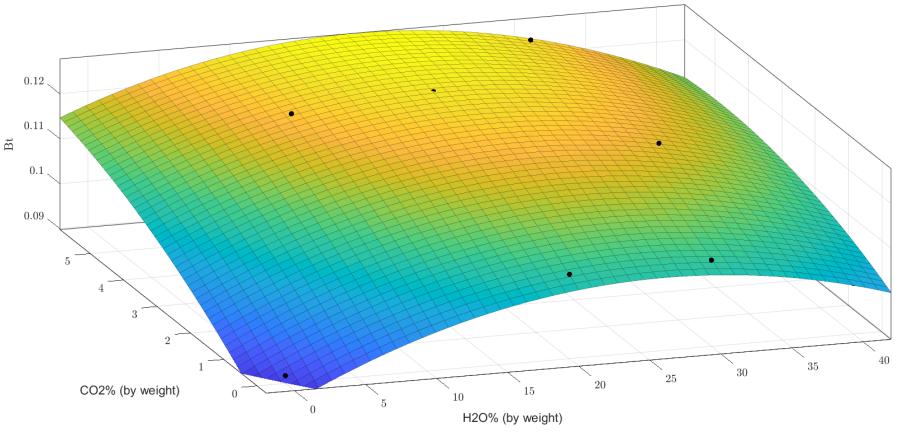

Figure 3.14: B_T values for TEPA varying with different CO_2 and H_2O concentrations

The equations of A_T and B_T are shown below.

$$A_T = p00 + p10 * (x-25) + p01 * (y-1.5) + p20 * (x-25)^2 + p11 * (x-25) * (y-1.5) + p02 * (y-1.5)^2 + p30 * (x-25)^3 + p21 * (x-25)^2 * (y-1.5) + p12 * (x-25) * (y-1.5)^2 \quad (3.4)$$

$$B_T = b00 + b10 * (x-25) + b01 * (y-1.5) + b20 * (x-25)^2 + b11 * (x-25) * (y-1.5) \quad (3.5)$$

where

p00	=	-9.719	b00	=	0.1163
p01	=	1.628	b01	=	0.003672
p02	=	0.05538	b10	=	-0.0003582
p10	=	-0.01458	b11	=	-6.641e-06
p11	=	-0.01655	b20	=	-4.591e-05
p12	=	-0.00287			
p20	=	-0.001893			
p21	=	-0.0008135			
p30	=	-1.835e-05			

Similar to PEI-600, for TEPA the equations 3.4 and 3.5 van be used in equation 3.1 to calculate viscosity with temperature and concentrations of CO_2 and H_2O as inputs.

3.2.6. ERROR ANALYSIS

The actual viscosity of PEI-600 and TEPA for different loadings of CO_2 and H_2O have been found out and using equation 3.1, the predicted model for the same concentrations and temperature can be calculated. However, before using this calculated data in future work its imperative to statistically analyse this data. Figures 3.15 and 3.16 show calculated vs actual viscosity of PEI-600 and TEPA respectively. These curves give a sense of accuracy to the viewer before moving on to the statistics.

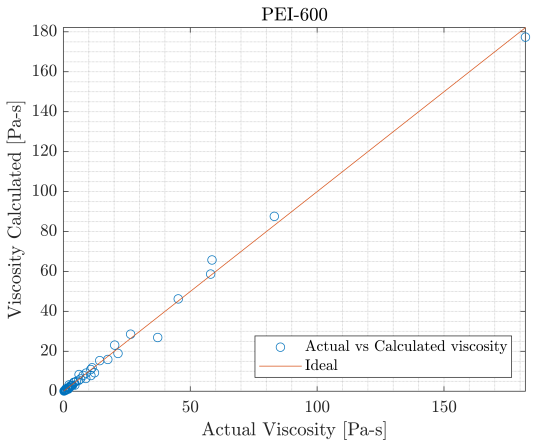

Figure 3.15: Calculated vs actual viscosity of PEI-600

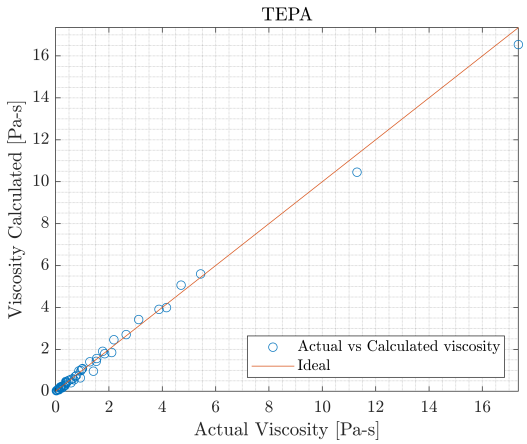

Figure 3.16: Calculated vs actual viscosity of TEPA

The accuracy metrics utilized to check this viscosity model were the mean absolute error (MAE) and coefficient of deviation, also called R^2 score. These metrics can be calculated using equations 3.6 and 3.7.

$$MAE = \frac{1}{n}\sum_{i=1}^{n}|a_i - c_i| \tag{3.6}$$

$$R^2 = 1 - \frac{\sum_{i=1}^{n}(a_i - c_i)^2}{\sum_{i=1}^{n}(a_i - a_{mean})^2} \tag{3.7}$$

where

MAE	=	mean absolute error
R^2	=	coefficient of deviation
a_i	=	actual value of viscosity found by experiments
c_i	=	viscosity values calculated by model
n	=	number of samples
a_{mean}	=	mean of actual values of viscosity

Although MAE gives an indication of the absolute deviation of the calculated data, knowing the relative magnitude of the raw data is essential. For data ranging from 0-100, an MAE of value 1 would be considered good. However, this MAE gives a less accurate prediction of deviation if the range of data analysed is from 0-5. Therefore, to indicate the relative size and spread of data analysed, the mean (a_{mean}) and standard deviation (σ_{act}) were also calculated. In addition, to compare how MAE would compare to spread of data, MAE as a percentage of standard deviation (MAE_{sd}%) is also calculated. These statistical values can be found in table 3.6.

Table 3.6: Statistical data describing error in the viscosity model

Sorbent	Data Range	MAE	R^2	a_{mean}	σ_{act}	MAE_{sd}%
PEI-600	[0.2101,182.1]	1.26	0.994	14.77	30.21	4.17
TEPA	[0.02723,17.35]	0.108	0.995	1.47	2.86	3.75

3.2.7. 3D PLOTS

Using the viscosity regression model made in this chapter, effects of viscosity can be view through informative 3D plots. Figures 3.17 and 3.18 represent the respective viscosity of PEI-600 and TEPA with variation in CO_2 and H_2O concentrations. Other 3D plots representing viscosity of PEI-600 and TEPA can be found in appendix B.2.

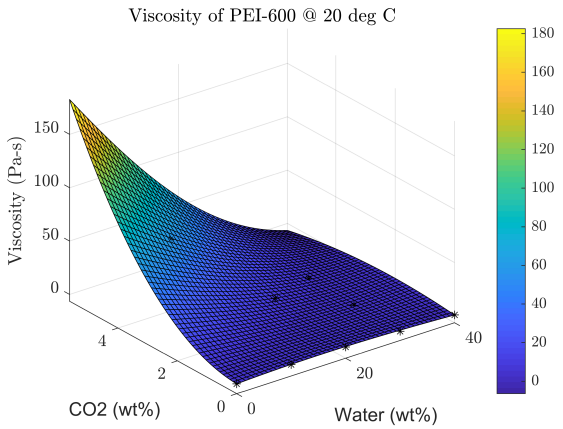

Figure 3.17: Viscosity of PEI-600 at 20°C

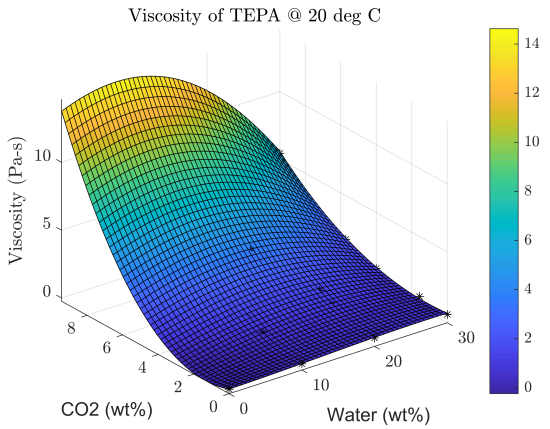

Figure 3.18: Viscosity of TEPA at 20°C

3.3. CO_2 LOADING EXPERIMENTS

This section discusses the second set of preliminary experiments considered as a requirement for this thesis. The idea behind CO_2 loading experiments was to load aqueous solutions of amines with pure CO_2 using the setup described in figure 3.1 to gain more knowledge based on the following points:

- Based on literature, aqueous amines performed better in terms of rate of CO_2 capture [70][75][65][71][72]. Therefore, samples of PEI-600 and TEPA with different H_2O concentrations were considered for this experiment in order to observe the effect of water on CO_2 loading rates.
- Since not much literature could be found on experiments on bulk amines, it was considered insightful to conduct such experiments. In addition, given the fact that each of such experiments was not as time consuming as sample preparation itself, it was decided to proceed with this experiment.
- It was also indicated by some of the literature that OH^- ions contribute significantly to the deprotonation of zwitterion [64], an important step in formation of carbamates. Therefore, it was also decided to premix pure sorbents with methanol, load them with CO_2 and compare results with aqueous samples to understand the importance of OH^- ions in absorption of CO_2.

3.3.1. METHODOLOGY

The methodology of conduction these loading experiments was fairly simple.

1. First, PEI-600 and TEPA were mixed with different water amounts to make various samples having different water concentrations.
2. Similarly, new samples of PEI-600 and TEPA samples were mixed with same amount of methanol to match water concentrations in earlier samples.

3. The loading setup shown in 3.1.1 was used to load these samples with CO_2 with a constant 15 litre/hour flow rate and 30 grams of sample at beginning to maintain consistency in loading of each sample.

4. The entire loading setup was weighed at t=0,2,5 and 10 minutes. The weight increase at each time interval was noted. This weight increase was associated to CO_2 being absorbed.

3.3.2. RESULTS

Insightful results were obtained from these loading experiments. First, PEI-600 with 0%, 10%, 20%, 30%, 40% and 70% water were loaded with CO_2. The results are shown in the figure 3.19 below where weight of CO_2 absorbed per weight of amine is plotted against time taken to load.

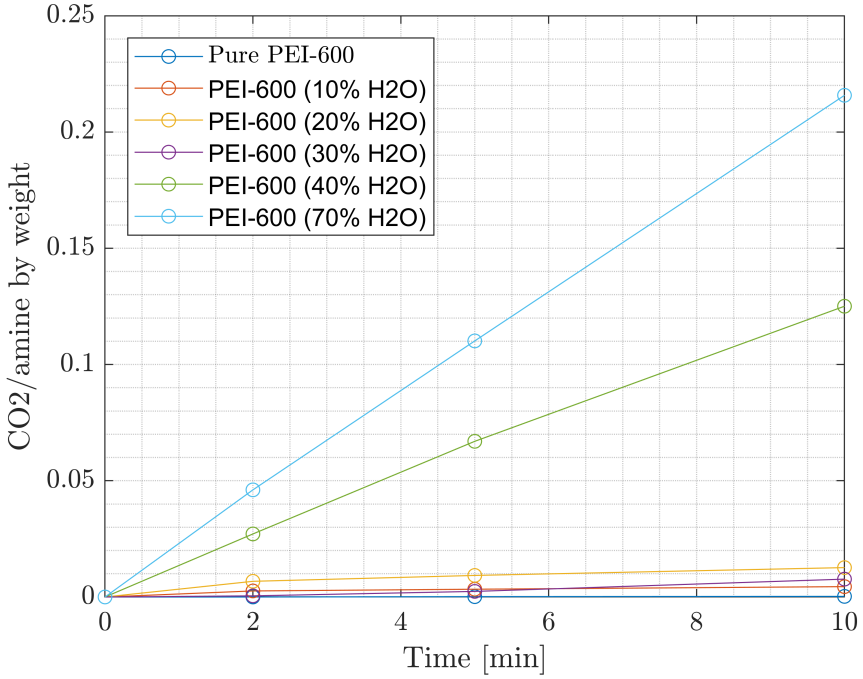

Figure 3.19: CO_2 loaded vs time taken for all PEI-600 samples premixed with water

It can be observed from figure 3.19 that higher concentrations of water resulted in a greater CO_2 capture rate which seems to be in adherence with the literature. However, the 10%-30% water range shows little promise when it comes to improving CO_2 absorption rates. Figure 3.20 zooms into the lower water concentrations for a better understanding.

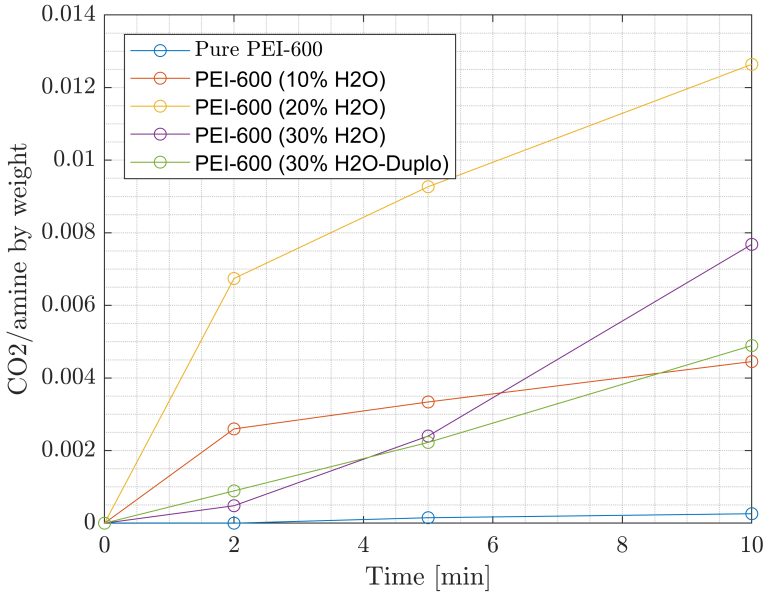

Figure 3.20: CO_2 loaded vs time taken for PEI-600 samples premixed with 0%,10%,20% and 30% water

It can be clearly seen from figure 3.20 that pure PEI-600 absorbs almost no CO_2 even though pure CO_2 is bubbled through it. This result was cross-checked by conducting a duplo which yielded the same result. This results points towards the fact that water has a role to play in increasing the absorption rate of CO_2. However, PEI-600 with 10%-30% are found to absorb significantly lesser CO_2 than higher water concentration samples.
Similarly for TEPA, samples of water concentrations of 0%,10%,20%,50% and 70% were made and the loading results can be seen in figure 3.21.

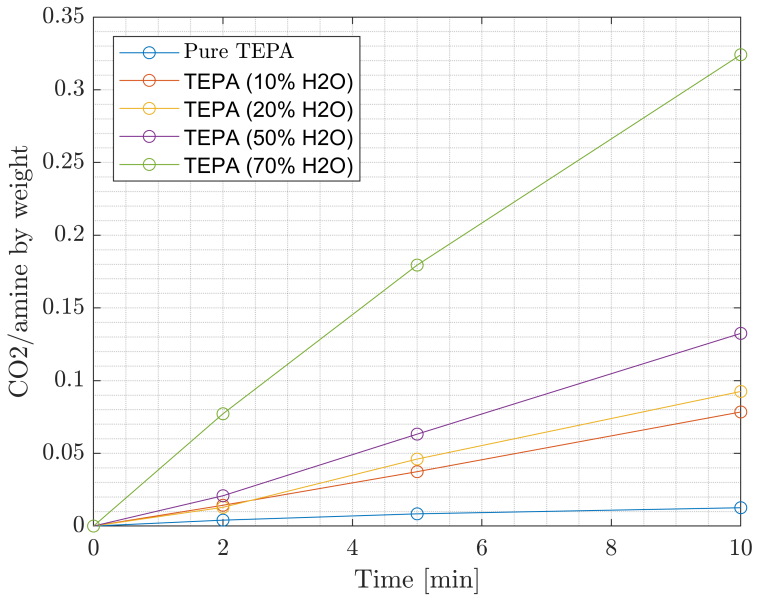

Figure 3.21: CO_2 loaded vs time taken for all TEPA samples premixed with water

With all TEPA samples premixed with water, the CO_2 capture rate increases with the increase in water concentration and similar to pure PEI-600, pure TEPA has the least CO_2 capture ability.
Another evident result from these experiments was that the performance of TEPA in terms of CO_2 capture rate was found to be better than PEI-600. A comparison of the two sorbents with different water concentrations can be seen in figures 3.22-3.25.

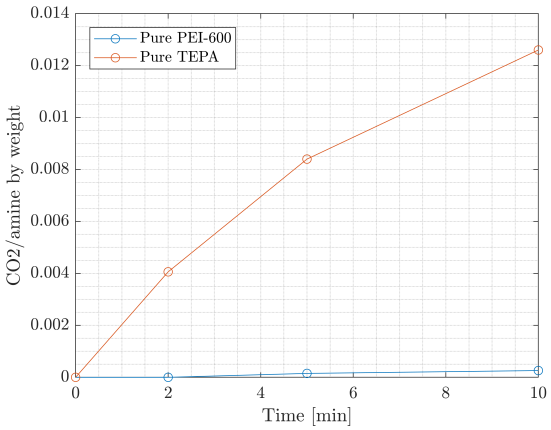

Figure 3.22: Pure PEI-600 vs Pure TEPA

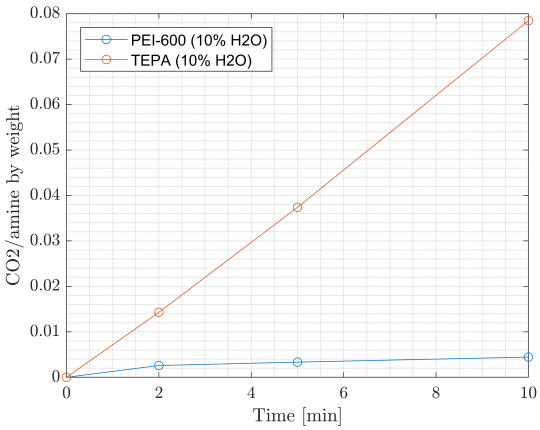

Figure 3.23: PEI-600 (10% H2O) vs TEPA (10% H2O)

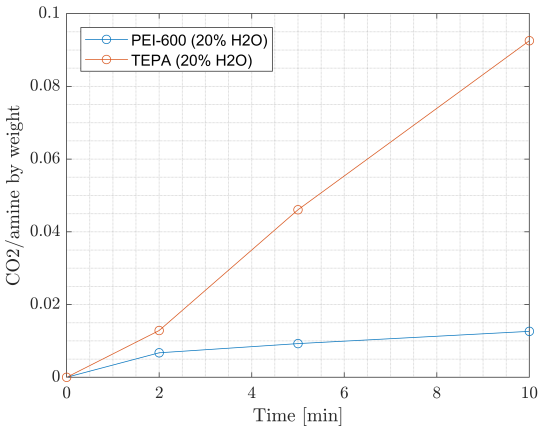

Figure 3.24: PEI-600 (20% H2O) vs TEPA (20% H2O)

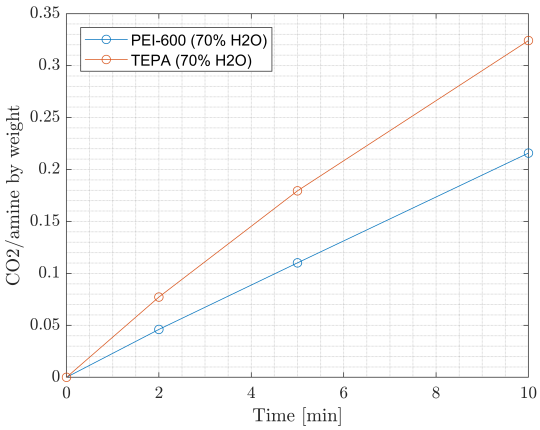

Figure 3.25: PEI-600 (70% H2O) vs TEPA (70% H2O). Concentrations in mass%

Interestingly, both PEI-600 and TEPA performed better with methanol in terms of CO_2 absorption rate as seen in figures 3.26-3.29.

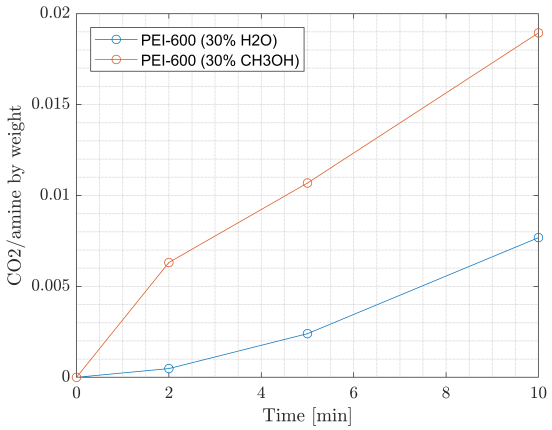

Figure 3.26: PEI-600 (30% H2O) vs PEI-600 (30% CH3OH). Concentrations in mass%

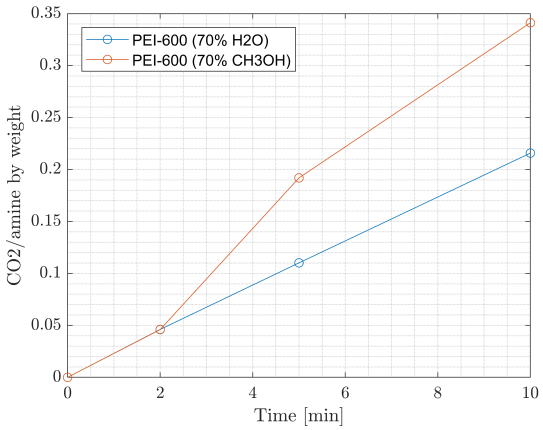

Figure 3.27: PEI-600 (70% H2O) vs PEI-600 (70% CH3OH). Concentrations in mass%

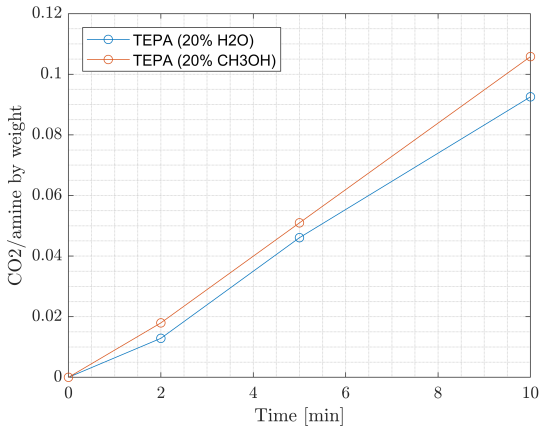

Figure 3.28: TEPA (20% H2O) vs TEPA (20% CH3OH). Concentrations in mass%

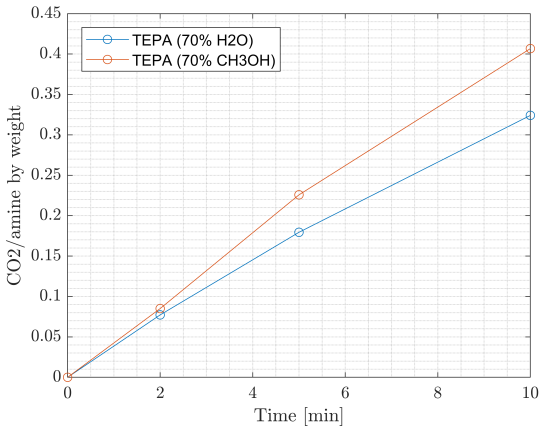

Figure 3.29: TEPA (70% H2O) vs TEPA (70% CH3OH). Concentrations in mass%

3.3.3. CONCLUSION

Many important conclusions were drawn based on these CO_2 loading experiments conducted on PEI-600 and TEPA with water and methanol.

- CO_2 capture rate of TEPA was found to be higher than PEI-600 both with no water and varying water concentrations.
- Both CO_2 capture rate and the amount of CO_2 captured per amine was found to be better with increasing water concentrations. This was found to be in agreement with the literature.
- The effect of OH^- ions and bases [64] could be justified with improved CO_2 capture abilities by addition of water. However, the claim becomes less relevant due the even better performance with just methanol. This could be explained by work done by Tamajón *et al.*[88] on MDEA systems with water and methanol. It was observed that

MDEA-methanol solution had significantly higher CO_2 absorption rate than MDEA-water solution. This was explained by the fact that solubility of CO_2 is significantly higher in methanol than in aqueous amine solutions [88][89].

- It was also observed that while loading pure CO_2, higher CO_2 loading corresponded with an increase in temperature of the sample being loaded. Although, the temperature was not measured since that wasn't the aim of these experiments, an investigation into such a temperature spike could be done using thermal imaging. If done in a systematic manner, these experiments could yield valuable results regarding heat of absorption.

Based on these experiments, it was considered worthwhile to investigate different water concentrations in PEI-600 and TEPA on a channel flow absorption setup.

4

EXPERIMENTAL SETUP

The goal of performing experiments on a sorbent flow through a channel is to study the absorption characteristics of a continuous absorption process. This chapter includes the description of the experimental setup, experiment methodology, calibration of most important measuring equipment, and, eventually, modelling techniques used in this thesis.

4.1. OVERVIEW OF EXPERIMENTAL SETUP

The first step in designing an experimental setup is to state the criteria for experiments based on questions that require investigation.

4.1.1. CRITERION/REQUIREMENTS

Based on literature, suggestions from previous researchers and preliminary experiments, the following criterion are considered before designing the experimental setup.

- The major requirement of this thesis is to characterize absorption in bulk amines in a channel flow (chapter 2.6). A scaled down version of a plate with a channel was made to perform an initial test to decide the channel dimensions. To meet the requirements of a uniform flow in a channel, a channel width (W) of 3-5 mm was considered enough given a sufficient mass flow rate of sorbent. The depth (2mm) remains the same for both. The basic schematic can be seen in figure 4.1.

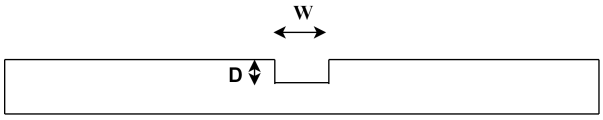

Figure 4.1: Basic schematic of a channel

- Given the fact that acrylic materials can be easily machined, a PMMA (Poly(methyl methacrylate)) of 5mm depth and 600 mm length was considered. The criteria for length was to have a sufficiently long channel to observe effects of absorption. Since Serrano Barthe[53] recommended to use a plate of 300 mm length for the design of absorption column in her research, a length of 600 mm was considered adequate for research pertaining to this thesis.

- Another requirement was a controlled mass flow rate of the sorbent. For such a small channel, it was decided that a syringe pump should be used as it is easily controlled for slow mass flow rates.
- Based on 3.3.3, a thermal imaging camera would be a valuable addition. Moreover, provisions were required to slide the camera from top to bottom of the plate observing a part of the flow at one time.
- A measuring technique was required to measure the concentration of CO_2 and H_2O at different intervals on the channel. Many techniques such as pH change, hue tests and conductivity measurements were tried but discarded due to the complexity of measurements, inaccuracy in calculations and time constraints. The details of these techniques are discussed in appendix C.1 and C.2. Based on section 2.6, it was decided to go ahead with spectroscopy using a calibration line of the FTIR machine. The calibration technique is mentioned in the subsequent sections.
- Finally, the setup should be mechanically robust and as modular as possible. In addition, provisions should be made such that the entire setup along with the plate, camera and syringe pump can be rotated to achieve an angle of 0-90° with the vertical.

4.1.2. SETUP DETAILS

The final experiment setup consists of a stand, main frame, thermal camera, syringe pump and a plate with a milled channel. The details of each part is mentioned systematically below. The sizes of the main frame and stand were decided by taking into account the size of plate, syringe pump and thermal camera.

MAIN FRAME

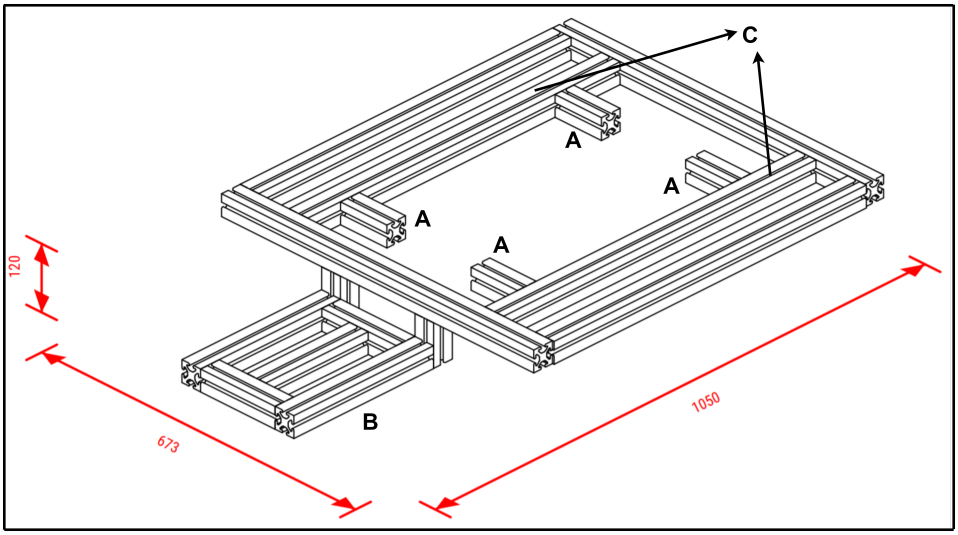

Figure 4.2: Isometric view of the main frame. The measurements shown are in mm.

Owing to its mechanical robustness and easy connection provisions, aluminium profiles (Profile-8 40*40mm, light, natural) were used to build the main frame (figure 4.2). To sup-

port the acrylic plate with a channel, 4 support structures (A) were provided. In addition, a base for fixing the syringe pump was added (B). Moreover, two profiles marked by C were equipped with sliders on which a camera stand could be mounted. This addition was made in order to facilitate the movement of the thermal camera with the flow, maintaining the plate and camera parallel at every instant. The weight of the main frame with all additions was approximated to be about 15 kg.

STAND FOR THE SETUP

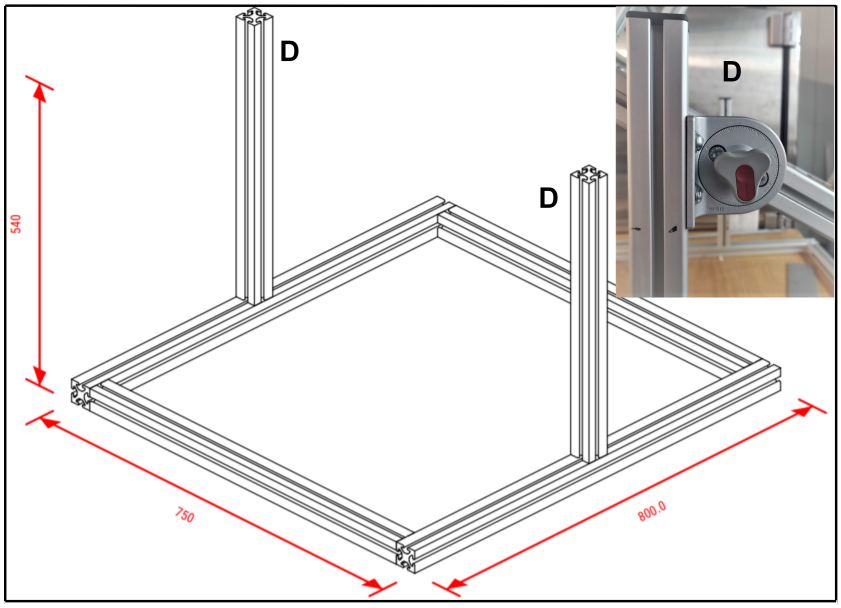

Figure 4.3: Isometric view of the stand to support the main frame. The measurements shown are in mm.

The stand or base of the entire experimental setup was build by using the same aluminium profiles (Profile-8 40*40mm, light, natural) bought from ITEM in Delft, Netherlands. The selection of aluminium profiles for the stand was made due to their high load-carrying capacity and mechanical robustness. The vertical profiles marked by D in figure 4.3 were each equipped with a swivel joint to facilitate the rotation of the mainframe at the required angle. The least count of the angle was 2.5°. Each of this joint, also shown in figure, could withstand a maximum of 250 kg of vertical static load. Since the weight of the main frame with the camera, syringe pump and plate was approximated to be a maximum of 15 kg, the swivel joint was considered adequate to bear the load of the entire setup.

PLATE AND CHANNEL

PMMA was selected as the material for the plate because of ease of machining as mentioned earlier. Two plates of 600*300 mm (length*width) were laser cut with provisions for bolts to fix it on the main frame. Both plates were milled using a milling machine to make a channel along the length of the plate. After machining, the channels were polished to achieve a smooth surface. One of the plates was machined to have a channel of 5*2 mm (width*depth) while the other had dimensions of 3*2 mm. Since, the objective was to conduct experiments on PEI-600 and TEPA using same mass flow rates, some preliminary ex-

periments on different channel width indicated that a 5mm wide channel should be used for PEI-600 and 3mm wide channel for TEPA to achieve homogeneous flow of both sorbents.

SYRINGE PUMP

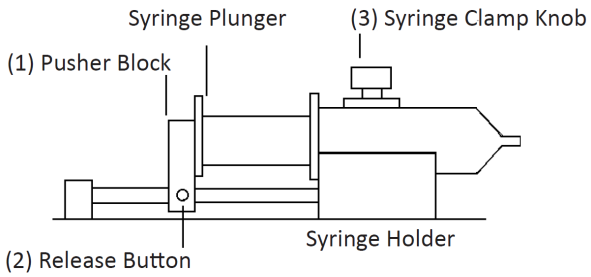

Figure 4.4: Schematic of a KDS100 syringe pump [20]

A KD Scientific syringe pump (KDS100 series) was used in this experimental setup [20]. Any syringe with a capacity of 10 microliter - 60 milliliter could be used in this type of pump. The software of this pump required the internal diameter of the syringe and flow rate as inputs. A BD Plastic 30 ml syringe was used in experiments pertaining to this thesis and the corresponding range of achievalble mass flow rates was from 0.1 ml/hr to 282 ml/hr. The syringe could be clamped on the pump and fastened using a clamp knob. Based on the internal diameter of the syringe and the flow rate selected, the speed of the pusher block was automatically adjusted. More information on this syringe pump can be found in appendix **??**.

THERMAL IMAGING CAMERA

Figure 4.5: TESTO 885 series thermal imaging camera

A TESTO 885 series thermal imaging camera (figure 4.5) with an infrared resolution of 320*240 pixels (76,800 temperature measuring points) was used in the experimental setup to capture thermal images [90]. This camera was equipped with a super resolution technology able to boost the image quality to 640*480 pixels. Moreover, its thermal sensitivity (< 30mK) made it accurate enough to observe even the smallest temperature differences. Similar aluminium profiles used for the main frame and stand were used to build a camera

stand that was mounted on sliders on the main frame. The stand was made such that the position of the camera was adjustable. It was fixed such that at a time it could capture an image of height of 50 mm. The aluminium profile had markings at every 50 mm to shift the camera with the flow of the sorbent.

FAN

An AD12038GP series, plastic fan of outer dimensions of 120*120 mm from the company ADDA was used in this experimental setup. With a rated voltage of 12V and corresponding current of 1.62A, this fan could provide a maximum air flow of 5.247 cubic meter per minute with a maximum pressure of 18.44 mmAq [91].

FINAL EXPERIMENTAL SETUP

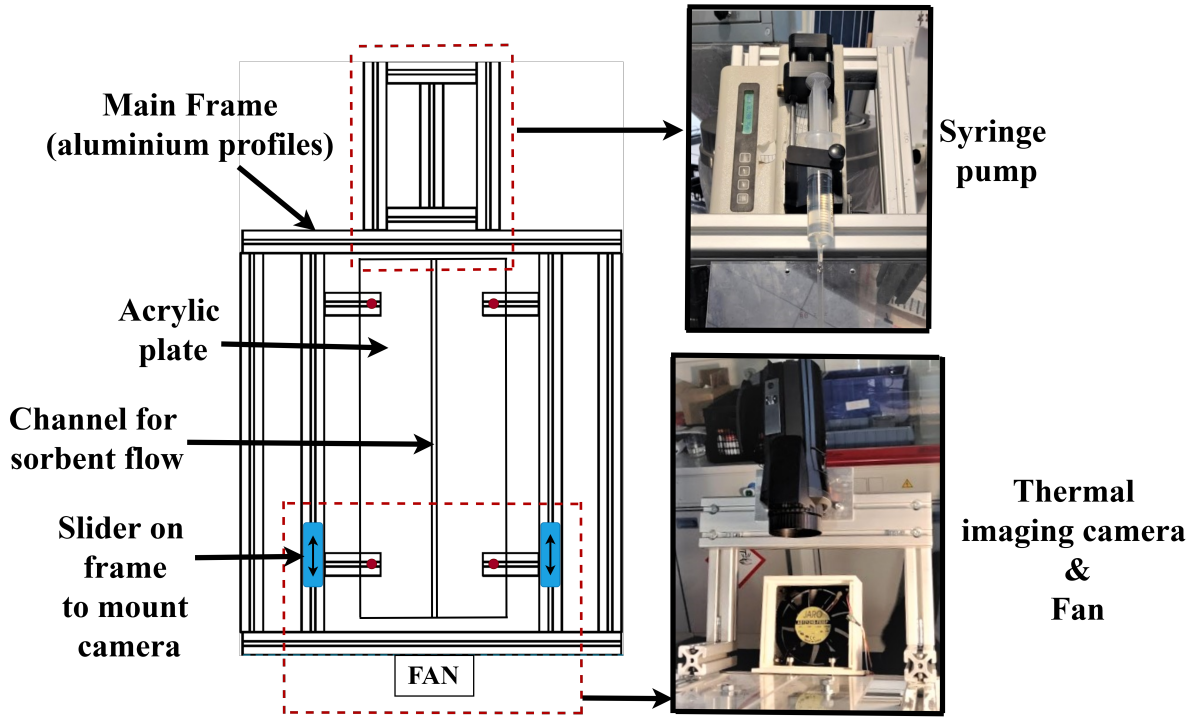

Figure 4.6: Top two-dimensional view of experimental setup

Figure 4.6 shows the main frame with provisions of additions described above. The PMMA plate rests on the 4 small aluminium profiles fastened by nuts and bolts to ensure rigidity. The plate has a channel milled right through the center along the length of the plate. The top red box marked by dotted lines is for fixing the syringe pump. It is adjusted in a manner such that the tip of the syringe rests on the channel as seen in the figure. The sliders are marked with a blue color on which the stand for the thermal camera is mounted as shown. The fan is enclosed in a 3d printed casing and fixed on the main frame. This entire setup shown in figure 4.6 is mounted on the stand and can be rotated to a preferred angle according to the experimental requirements. The original image of the final experimental setup with all provisions can be seen below in figure 4.7.

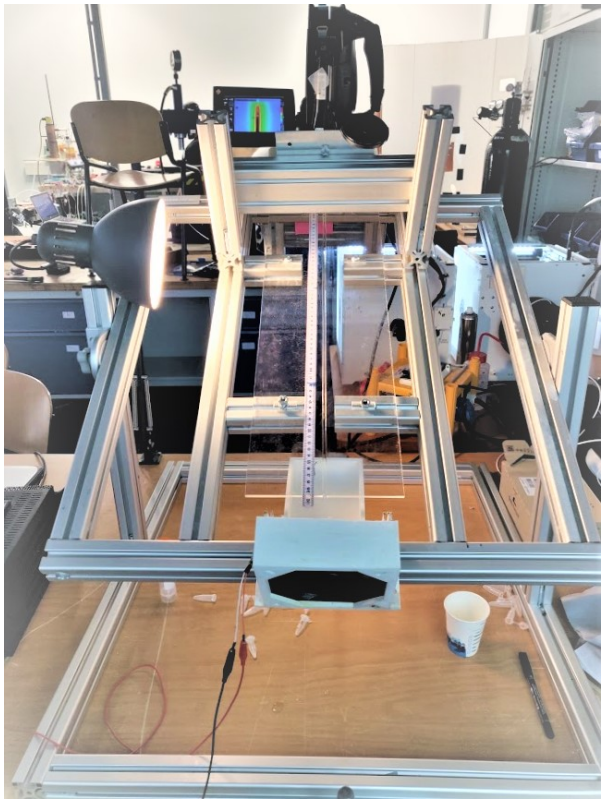

Figure 4.7: Original image of final experimental setup

MEASUREMENT EQUIPMENT

The setup shown in figure 4.7 was used to run the sorbent through the channel and collect samples at decided intervals. However, this was only the first part of the experiments. The second part was to measure the concentration of CO_2 and H_2O. This was done using a Nicolet iS50 FT-IR machine by Thermo Scientific shown in figure 4.8. The samples collected from the measurements were put into the spectrometer to achieve an output in the form of a graph of absorbance vs wave number through Thermo Scientific's spectrometry software called OMNIC. These graphs could be quantified through a calibration and analysis software known as TQ Analyst. The calibration procedure and more details on this can be found in appendix A.3.

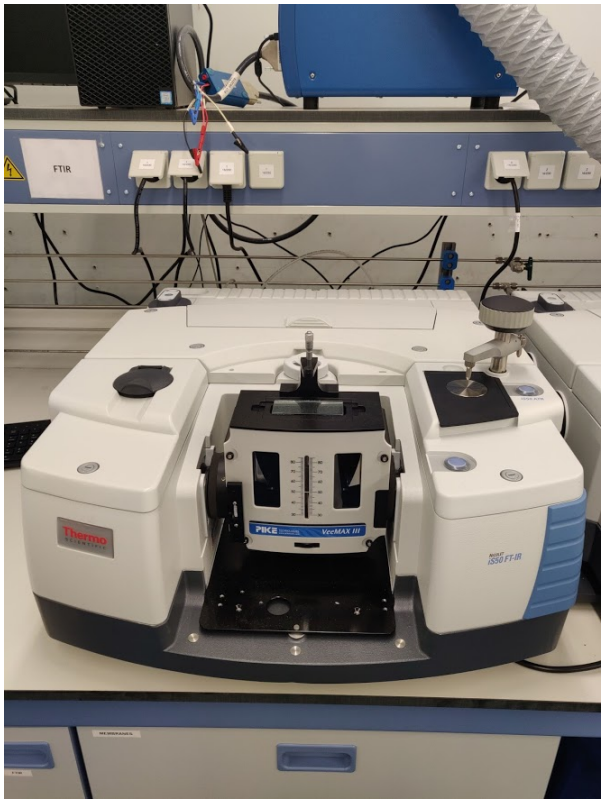

Figure 4.8: Nicolet iS50 FT-IR

4.2. EXPERIMENTAL METHODOLOGY

For this thesis and ease of understanding, the entire experimental procedure using the setup mentioned above can be divided into two parts - Flow experiments and Measurement of concentrations. Both parts require a meticulous and strict experimental methodology. Any deviation from the methodology or mistakes at any step might result in experimental errors, requiring the researcher to perform the entire experiment again. Keeping this in mind and also the time required to do each experiment, specific steps were decided upon and strictly followed with every experiment performed during this thesis to ensure repeatability and high quality of data produced. These steps are enumerated below separately for each part - *flow experiment* and *measurement of concentration*.

4.2.1. FLOW EXPERIMENT

1. The first step was choosing the inclination of the channel with respect to the vertical axis. This could be adjusted using the swivel joint that connected the stand to the main frame. An angle of 60° to the vertical axis was chosen for these experiments. Since the most important parameter in these experiments was the mass flow rate of the sorbent, the angle was selected based on ease of performing the experiment.

2. The second step was choosing the channel size to be used. the plate with a 5mm wide channel was selected if experimenting on PEI-600 and a 3mm one if the sorbent was TEPA. The plate and specifically the channel was cleaned by dried cloth, methanol and water and dried again before beginning the experiment. Once the plate was cleaned and dried, it was made sure that the plate is rigidly fastened to the main

frame at a specific position according to the markings on the frame.

3. After cleaning and fixing the plate, a new BD Plastic - 30 ml syringe was taken, filled with 20 ml of sorbent of interest while making sure that the syringe did not have any air bubbles. 20 ml of sorbent in the syringe was found to be enough to last hours with the range of mass flow rates used in the experiments. The syringe was cleaned well from the outside and a sample of around 0.1 ml was collected from it and stored in a small plastic bottle used to store chemicals. The concentration of this initial sample was considered to be the starting concentration of the sorbent and the amount of sample collected did not matter at this stage. To maintain consistency in experiments, 0.1 ml was collected at the beginning of each experiment.

4. Now, the syringe was mounted on the syringe pump making sure the tip of the syringe rested on the channel on the plate. The syringe pump was switched on and the required mass flow rate was fed in. In the experiments done in this thesis a mass flow rate range of 0.07-0.1 ml/min was generally used.

5. As soon as the syringe pump was switched on, the fan was also switched on. The fan was supplied 12 V at all times. This decision was made to satisfy the assumption of no depletion of CO_2 and H_2O in air at any point near the channel. It is explained in subsequent sections.

6. A stop watch was used to measure the time taken for the sorbent to flow through the channel. As soon as the first drop hit the channel, the timer was started. The time at every 50 mm was noted down without fail and it was attempted to note the time more frequently if possible. During the time between every 50 mm, the thermal camera was used just to observe the flow. Since the thermal camera was fixed such that it could capture an image of height of 50 mm, it was used after every 50 mm of the flow. Images were taken for 0-50 mm, 50-100 mm and so on.

7. After the first drop exited the channel, a waiting period 1.5 hours was observed. The flow and the mass transfer was assumed to be in steady state after this period. After this time interval, the thermal camera was used again to click thermal images at intervals of every 50 mm.

8. Now, while keeping the fan switched on, samples were collected upstream every 100 mm starting at the bottom of the plate. A small spatula was used to scoop the sorbent out of the channel. It was made sure that this step was meticulous and the entire 100 mm of channel was emptied of the sorbent which was stored in the same plastic container used earlier. As soon as each sample was collected, it was made sure that the cap of the container was closed immediately to avoid any absorption of CO_2 or H_2O from ambient air. The sample bottles were marked form 6 (500-600 mm) to 1 (0-100 mm). This step required practice in order to collect the samples neatly and efficiently and to make it repeatable in every experiment.

9. The samples pertaining to every experiment was stored in a separate box with the experiment code from which the details of the experiment could be traced back.

10. Finally, the fan and the syringe pump were switched off and the setup was cleaned. This step brought an end to the flow experiment.

4.2.2. MEASUREMENT OF CONCENTRATIONS

After the samples had been collected from multiple experiments, all samples were taken to the Nicolet iS50 FT-IR machine to be analysed. The steps for calibration and functioning of the software aren't covered in this section and are discussed in appendix A.3.4 due to their complexity. The mechanical steps and points to be kept in mind are described systematically below.

1. The first step in order to use the FTIR was to cool the detector using liquid Nitrogen. Before starting experiments, liquid Nitrogen was filled into a provision made into the FTIR machine. Standard safety procedures, use of thermal gloves, and masks were absolutely necessary. After filling the machine with liquid Nitrogen, standard waiting time of 1 hour was followed in order to let the detector cool down.

2. After the waiting period, the device was switched on and the software, OMNIC was run. Some standard tests were automatically run and the software gave a green light to proceed with the samples.

3. The sample to be analysed could be place on a small circular section provided on the machine. Before putting any sample, it was cleaned by using methanol at least twice. Prior to analysing any sample, first a background spectrum is collected.

4. After the background spectrum is collected and saved in the software, demi-water is used as a sample and analysed. This is done to check if the base line of the spectrum starts from a value of absorbance equal to zero, which is required to get accurate results later. If this is not the case of the spectrum produced by the software doesn't match the spectrum of water, it indicates that the sample collection section hasn't been cleaned properly. Thus, it is cleaned again, a new background spectrum is collected and demi-water is used again to ensure if the analyses is valid. Once the demi-water shows a valid spectrum with a base line at an absorbance value of zero, further analyses of other samples can be proceeded with.

5. Now, the first sample from the experiments done could be analysed. For a FTIR analysis, no more than a drop of each sample is required to produce a spectrum. However, the sample in a the plastic container is not mixed and the concentrations of each drop could vary since the FTIR only analyses the bottom few microns in contact with its surface. The aim of this measurement is to find the average concentration of any sample collected from a 100 mm region on the channel. Therefore, each of these samples is thoroughly mixed with a 1 ml syringe. The mixing is labour intensive, but also extremely necessary to achieve an average concentration. Usually each sample was mixed manually for 5-10 minutes.

6. After mixing the samples well, each sample is analysed multiple times on FTIR. It is recommended to analyze atleast 3-5 drops of each sample separately. Any air bubbles in the drop being analyzed could result in inaccurate results. Therefore, the samples were mixed during the waiting period for cooling of the detector so that the air bubbles, if any, would disappear. If the spectral graphs produced by these different droplets are identical, it would mean that the samples were well mixed and now have a homogeneous concentration of CO_2 and H_2O.

7. The same procedure was followed for all samples. Having said that, after every 60 minutes, a new background spectrum was taken and demi-water was analysed again to be sure of the results obtained.

8. Once all the spectral graphs are obtained, a pre-defined calibration was used to quantify each spectrum to obtain CO_2 and H_2O concentrations in each sample. Refer to appendix A.3.4 for details on calibration.

4.2.3. EXPERIMENTAL PLAN

Once the experimental setup and measurement methods were finalized, an experimental plan was made. The concentrations of PEI-600 and TEPA to be tested were chosen. Effect of change in mass flow rate of sorbent and air was taken into account in some of the experiments. All experiements were done at an inclination of 60° to the vertical.Some experiments were performed twice for validation. The design of experiments can be seen in table 4.1.

Table 4.1: Details of experiments performed in this thesis

Sorbent Type	**Starting H2O Concentration [mass %]**	**Starting CO2 concentration [mass%]**	**Mass Flow Rate [ml/min]**	**Fan Voltage**	**Inclination to vertical [deg]**
PEI-600	0%	0%	0.08	12V	60
PEI-600	0%	0%	0.08	0V	60
PEI-600	0%	0%	0.08	7V	60
PEI-600 (2)	0%	0%	0.08	12V	60
PEI-600	0%	0%	0.1	12V	60
PEI-600(2)	0%	0%	0.1	12V	60
PEI-600	10%	0%	0.08	12V	60
PEI-600	20%	0%	0.08	12V	60
PEI-600	30%	0%	0.08	12V	60
PEI-600	40%	0%	0.08	12V	60
TEPA	0%	0%	0.08	12V	60
TEPA	10%	0%	0.08	12V	60
TEPA	20%	0%	0.08	12V	60
TEPA	30%	0%	0.08	12V	60
TEPA(2)	0%	0%	0.08	12V	60

4.2.4. DATA COLLECTED FROM EXPERIMENT

After the experiments were performed and the samples analysed, a lot of different data could be collected. For the purpose of reader's understanding, the outputs or the useful data collected for each experiment are summarized below.

HEAT DATA

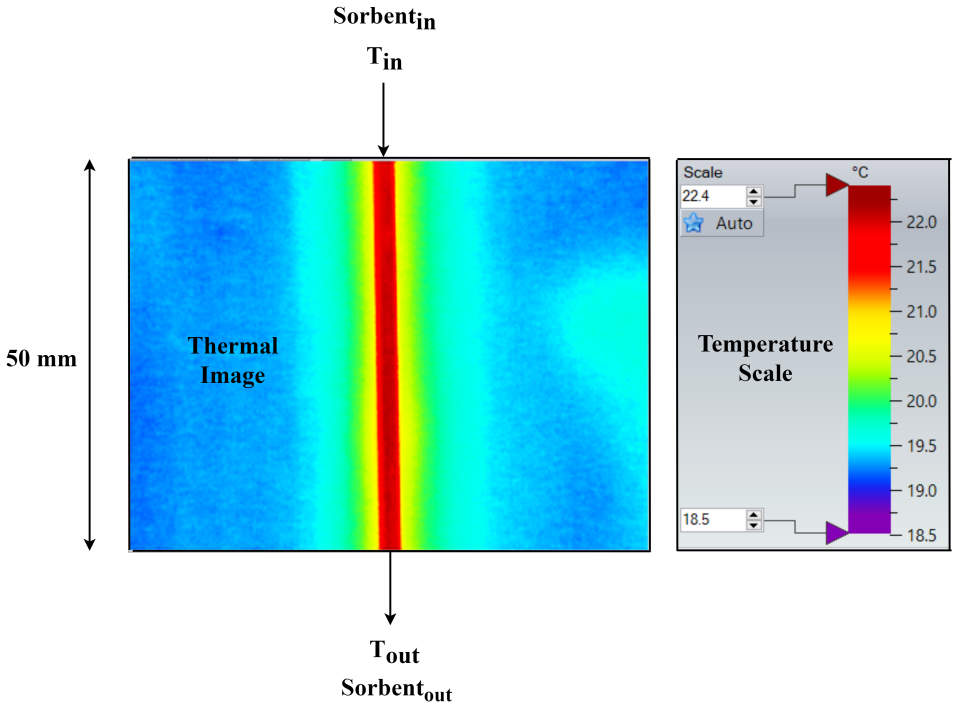

Figure 4.9: An example of thermal image captured as seen in the processing software - IRSoft

Every thermal image taken from the thermal imaging camera could be processed using TESTO's software called IRSoft. This software displays these thermal images as shown in figure 4.9. The software had various tools to analyze this image. The following useful data could be collected from these images.

- The **average temperature** of the sorbent flowing through the channel of every 50 mm of the flow.
- The **inlet and outlet temperatures** (T_{in}, T_{out}) of every 50 mm section on the channel.
- The **temperature profile** at any cross section of the plate.
- **Maximum or minimum temperature** at any specified area on the image.
- Apart from points mentioned above, a quantitative or qualitative analysis could be done performed while comparing the same section on the channel at different time intervals. The heat conduction through the plate could also be observed.

FLOW DATA

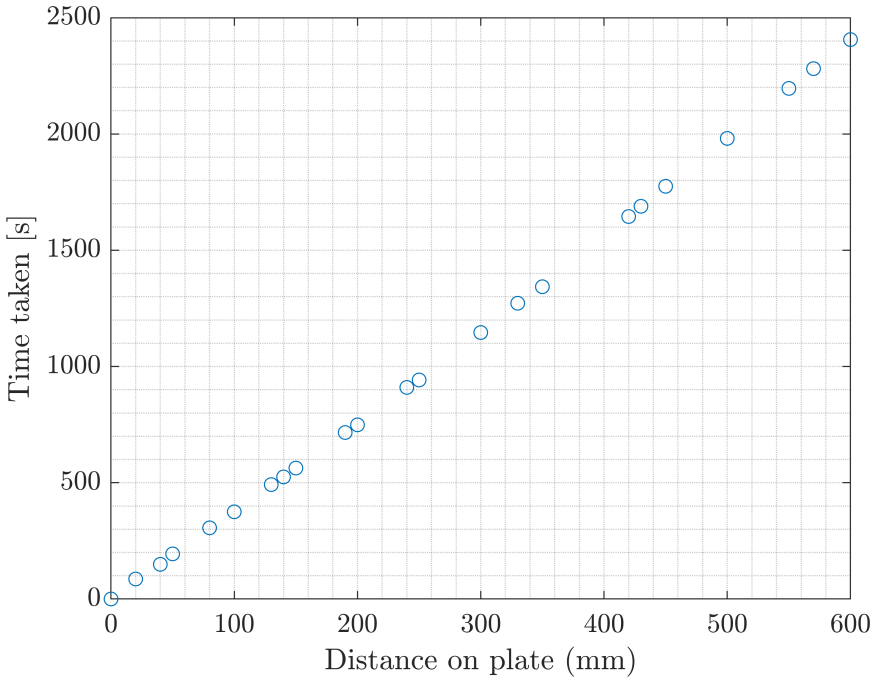

Figure 4.10: An example of flow rate measurement

The **average flow rate** of the sorbent in the channel can be found out with the data collected. An example of data collected on time taken for the sorbent to flow can be seen in figure 4.10. In addition, the **average viscosity** at every 100 mm can be calculated using the viscosity model described in 3.2.5 since the concentrations of CO_2 and H_2O and the average temperature of every 100 mm would be known through experiments. Finally, the **mass flow rate of sorbent** was also known as it was controlled by the syringe pump used in the experiments.

FTIR DATA

Qualitatively, the data from FTIR tells a lot about the reaction path taken for the capture of CO_2 - **carbamate or bicarbonate** formation. It could also point towards urea formation if the sorbent goes through degradation. Finally, it can be used to qualitatively compare two different samples to check which one has higher CO_2 or H_2O concentration. Quantitatively, if well calibrated with many known samples, the FTIR can give accurate predictions of the CO_2 and H_2O concentrations in a sample. Thus, amounts of CO_2 or H_2O absorbed per amount of sorbent can be easily found out.

4.2.5. DISCLAIMERS AND ASSUMPTIONS

Although, the amount of data collected from these experiments is colossal, it is imperative to point out the limitations of these data and validate major assumptions made during the experiments.

DISCLAIMER

Before analysing any data from this thesis, the following points should be kept in mind.

1. All experiments were performed at room temperature and atmospheric pressure. It took two and a half months to perform all the required experiments and it was observed that the room temperature variation was 0-2°C in this time frame. Except for the heat model (to be discussed in subsequent chapters), this temperature variation was assumed to have no affect on absorption rate.

2. Change in relative humidity in the time frame of these experiments was also not taken into account. In fact, the concentration of CO_2 and H_2O was assumed to be always constant in ambient air.

3. Any instabilities in the flow of sorbent that might arise due to viscosity change or reactions during absorption were not studied.

4. The objective of this thesis was to characterize the absorption in a bulk amine flow, and the points mentioned above were considered insignificant due to only small changes in the parameters mentioned above.

5. In addition to the points mentioned above, the average flow rate required to find a space time yield was measured by noting down the time taken for the flow front to travel from 0mm to 600 mm on the plate. The bulk velocity of the flow was not calculated.

ASSUMPTIONS

In order to prove the validity and quality of the data collected in this thesis, 3 key assumptions are mentioned below with their respective validation.

Assumption 1 (No local depletion of CO_2 and H_2O): Concentration of both CO_2 and H_2O wasn't depleted at any point on the channel while the experiment was running. In other words, CO_2 and H_2O were replenished at every point on the channel flow. Thus, the driving force or partial pressure of CO_2 and H_2O was always constant during an experiment.

Validation of assumption 1: Three experiments were done to validate the assumption mentioned above. Since the operating voltage of the fan being used was related to air mass flow rate. Identical experiments with the same sorbent mass flow of 0.08 ml/min were performed using pure PEI-600 on a 5 mm channel with a voltage of 0V, 7V and 12V. The angle of inclination of the channel to the vertical was kept constant at 60° for all three experiments. This was done to compare the amount of absorbed CO_2 and H_2O in the sorbent. The results can be seen in figures 4.11 and 4.12.

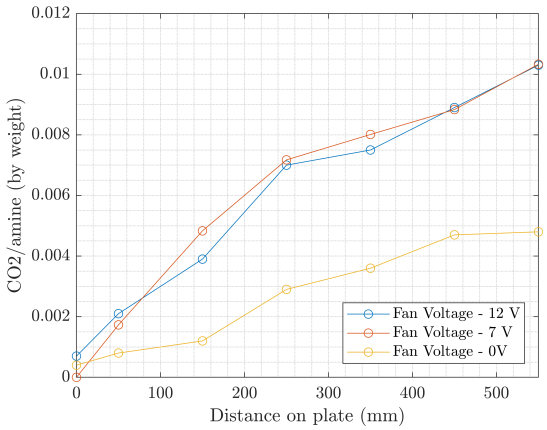

Figure 4.11: CO_2/amine absorbed during flow through channel with three different fan voltages

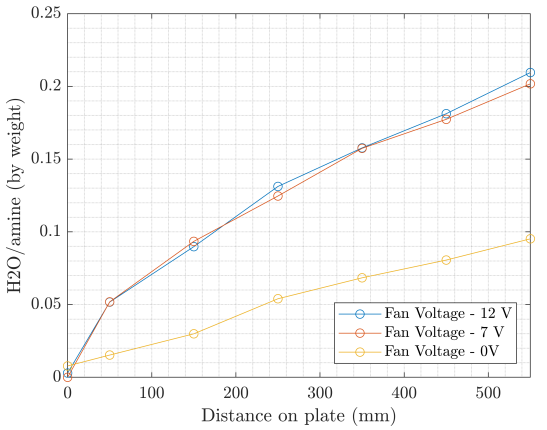

Figure 4.12: H_2O/amine absorbed during flow through channel with three different fan voltages

It can be observed from the figures above that without a fan (0V), the absorbed amount of CO_2 and H_2O are considerably less than the other two experiments. This indicates the depletion of CO_2 and H_2O due to the air not being replenished. In contradiction, the experiments performed with 7V and 12V yield similar results. This indicates that there is no depletion of CO_2 or H_2O with both of these experiments since the mass flow rate of air should be even larger when operating the fan at 12V. Since, all experiments done in this thesis are with a fan operating voltage of 12V, the assumption of no local depletion of CO_2 and H_2O seems valid.

Assumption 2 (Sample collection process is valid): Since sample collection in the flow experiments involves scooping the sorbent out with a spatula, the quality of the data depends on an efficient way of collecting and repeatable consistency by the experimentalist. This thesis assumes that the sample collection procedure is consistent, and experiments are repeatable.

Validation of assumption 2: Due to time constraints, duplos of all experiments were not possible. Therefore, during the early stages of experiments, some duplos were performed to assess the quality of data being produced. One such duplo was performed on pure PEI-600 with a sorbent mass flow of 0.08 ml/min and operating voltage of fan at 12V. The angle of inclination of the channel to the vertical was kept constant at 60°.
It can be seen from figures 4.13 and 4.14 that the two experiments yield similar results. The minute differences in the data points can be attributed to experimental errors. However, the similarity in data can be easily recognized. Therefore, the assumption of repeatable experiments is regarded as valid.

Assumption 3 (Average concentration is obtained from FTIR): Another big assumption is that the results from the FTIR represent the average concentration of the sample collected. In this thesis, this is assumed to be true.

Validation of assumption 3: Each sample collected from a section of the channel was well mixed before analysing it on the FTIR. In order for the analysed data to represent

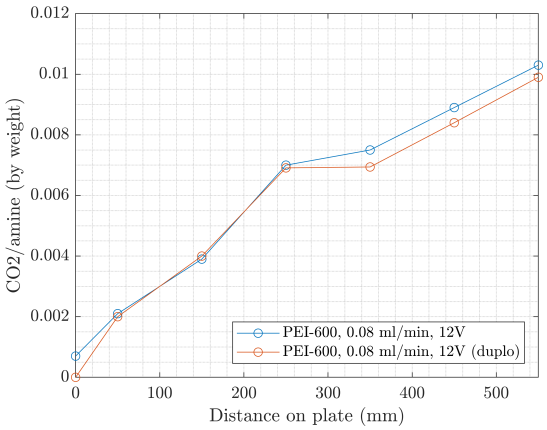

Figure 4.13: CO_2/amine absorbed during flow through channel and compared with a duplo

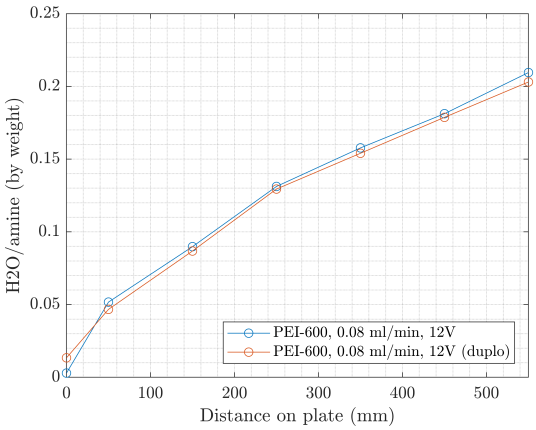

Figure 4.14: H_2O/amine absorbed during flow through channel and compared with a duplo

the average concentration of the sample collected, multiple drops from the same sample should have the same concentration of CO_2 and H_2O or in other words, the absorbance vs wavenumber graph obtained from OMNIC should overlap for each droplet analysed. This was in fact found to be true and can be seen in figure 4.15. Therefore, the mixing technique is valid and same is true for this assumption.

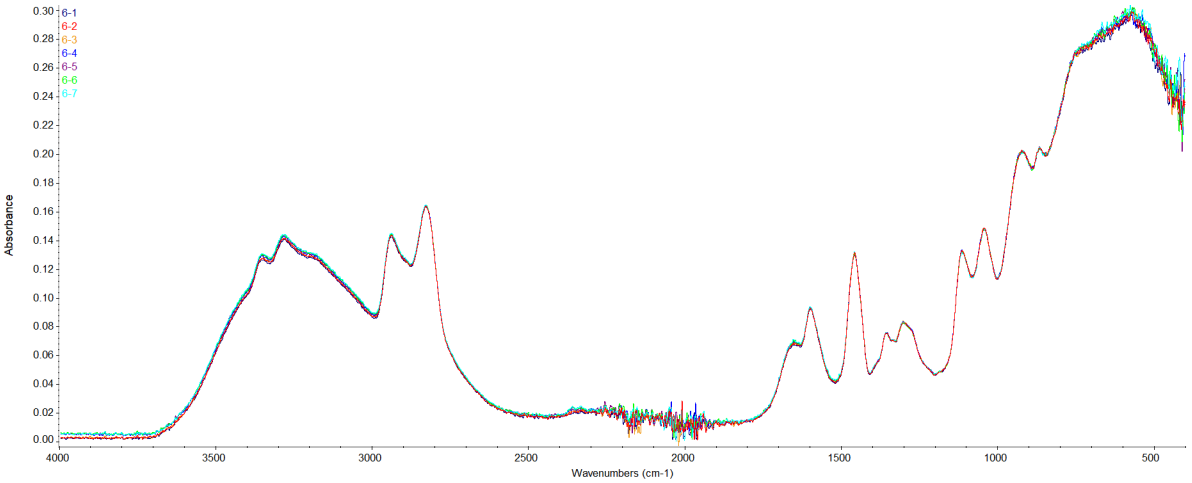

Figure 4.15: Absorbance vs wavenumber graph taken from OMNIC (software to process FTIR's data). These plots represent the sample taken from an experiment on PEI-600 from 500-600 mm section on the channel. The sample was well mixed and seven droplets from the same sample were used to analyse it, thus 6-1 represents sample taken from 500-600 mm section of the channel and the first drop of that sample being analysed after mixing the entire sample well

5

MODELLING FRAMEWORK

This chapter discusses the logic, conditions, assumptions, and overall framework of the models developed during this thesis. The chapter begins with insights into a model to calculate the heat of absorption derived from thermal data obtained during experiments. Subsequently, the chapter moves into discussion on modelling of an absorption column, which would be valuable to design one.

5.1. HEAT MODEL

Based on the thermal data collected during the experiments, a heat model was made to calculate the heat of absorption during the absorption process. This section describes the heat transfer phenomena, steps taken, assumptions made and guides through the entire process of this model.

5.1.1. INTRODUCTION

While conducting experiments on continuous absorption on the flow of bulk amines through a channel, the sorbent was expected to release heat due to the absorption of CO_2 and H_2O (2.4.3,3.3.3) as seen in figure 5.1 (A). The expectation were found to be true as seen in figure 5.1 (B).

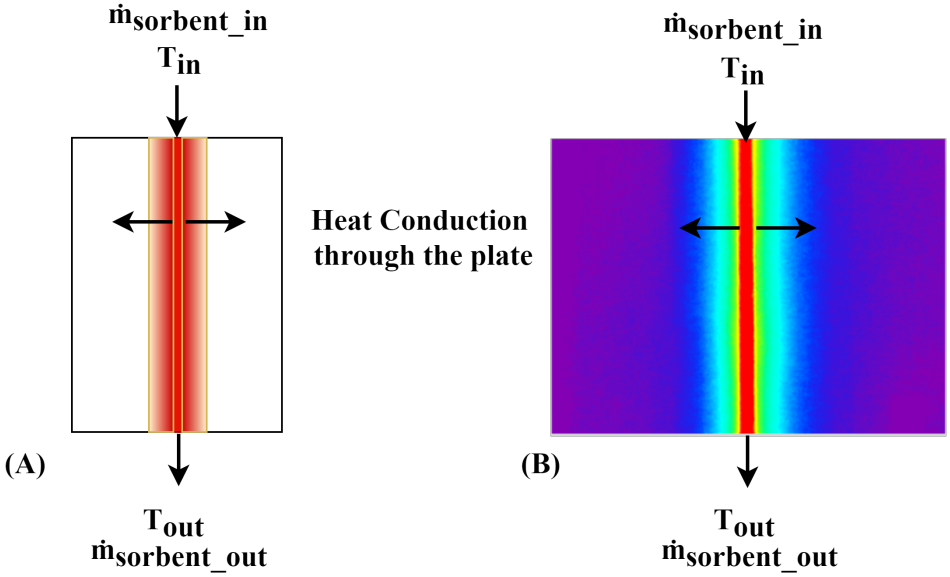

Figure 5.1: (A) Depiction of expected heat release while sorbent flows on a channel milled on a plate (B) Example of a thermal image collected during experiments depicting the same

The sorbent absorbed CO_2 and H_2O while flowing down the channel and due to their respective heat of absorption, the thermal imaging camera recorded an increase in temperature in the sorbent. Due to a temperature difference between the sorbent and the plate, heat was also being conducted to the plate. Moreover, other modes of heat transfer that couldn't be shown in figure 5.1 were also taking place. All three modes of heat transfer - conduction, convection and radiation were at play.

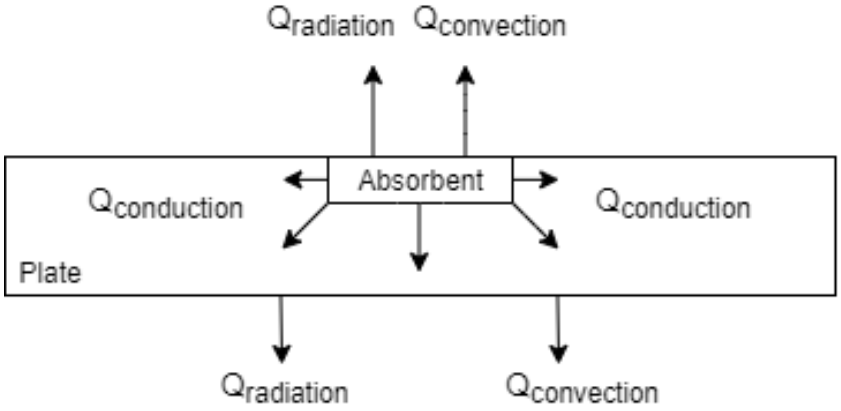

Figure 5.2: Depiction of heat transfer considering a cross-section of the plate. Note: the arrows are only a depiction and not the actual direction of the heat flux.

Figure 5.2 describes the heat transfer from the sorbent to the plate and surroundings. The heat through the sorbent was conducted through the plate while the top and bottom surfaces of the plate lost heat to the surroundings by convection and radiation. Since the top part of the plate experienced a forced air flow through the fan, the heat loss through the top was expected to be the greatest.

5.1.2. ENERGY BALANCE

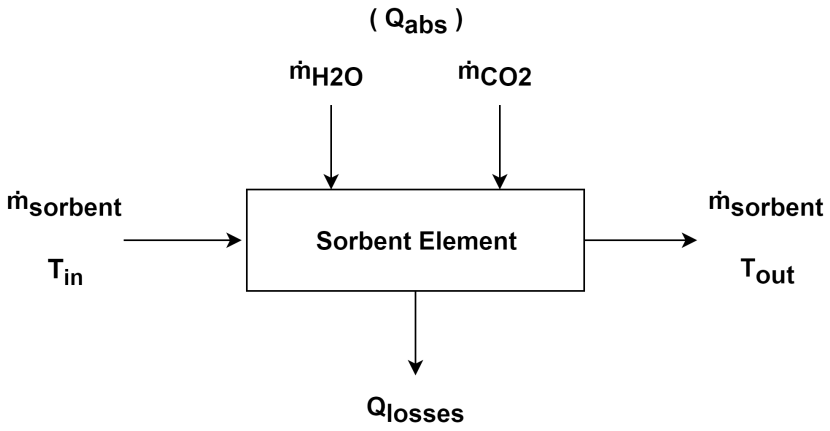

Figure 5.3: Depiction of inputs and outputs when a small element of sorbent is considered.

A small element of the sorbent was considered. Figure 5.3 describes that the sorbent flows with a fixed mass flow through a small element with an inlet and outlet temperature while the element is heated due to the heat of absorption of CO_2 and H_2O. Meanwhile, the element loses heat due to losses described in figure 5.2. According to the principle of conservation of energy [92], change in internal energy within the system is equal to the sum of heat transferred into the system and heat generated within the system. Considering steady state, equation 5.1 was formed for the sorbent element considered in figure 5.3.

$$Q_{abs} - Q_{losses} - \dot{m}c_p(T_{out} - T_{in}) = 0 \tag{5.1}$$

The first two terms in equation 5.1 have been expanded and can be seen in equation 5.2 and 5.3.

$$Q_{abs} = \dot{m}_{CO_2}\Delta H_{abs,CO_2} + \dot{m}_{H_2O}\Delta H_{abs,H_2O} \tag{5.2}$$

$$Q_{losses} = Q_{cond} + Q_{conv} + Q_{rad} \tag{5.3}$$

Therefore, the final equation expanding all terms in equation 5.1, takes the form of equation 5.4 as seen below.

$$\boxed{\dot{m}_{CO_2}\Delta H_{abs,CO_2} + \dot{m}_{H_2O}\Delta H_{abs,H_2O} - Q_{cond} - Q_{conv} - Q_{rad} - \dot{m}c_p(T_{out} - T_{in}) = 0} \tag{5.4}$$

where

$\dot{m}_{CO_2}$	=	molar flow rate of CO_2 into sorbent [mol/s]
$\dot{m}_{H_2O}$	=	molar flow rate of H_2O into sorbent [mol/s]
$\Delta H_{abs,CO_2}$	=	heat of absorption of CO_2 [J/mol CO_2]
$\Delta H_{abs,H_2O}$	=	heat of absorption of H_2O [J/mol H_2O]
Q_{cond}	=	heat loss through conduction [W]
Q_{conv}	=	heat loss through convection [W]
Q_{rad}	=	heat loss through radiation [W]
$\dot{m}$	=	mass flow rate of sorbent [kg/s]
c_p	=	constant pressure specific heat [J/kgK]
T_{in}	=	inlet temperature of sorbent [° C]
T_{out}	=	outlet temperature of sorbent [° C]

The aim of this model was to solve the equation 5.4 in order to calculate the heat of absorption. To be able to achieve the desired results, all the unknown parameters were needed to be found.

5.1.3. UNKNOWN PARAMETERS

This subsection discusses the methods used to calculate or estimate each of the parameters in equation 5.4.

$\dot{m}/T_{in}/T_{out}$

Since the mass flow rate was controlled by the syringe pump used in the experiments, this value was known. T_{in} and T_{out} were also known from the thermal data collected (4.2.4).

CONSTANT PRESSURE SPECIFIC HEAT (c_p)

Based on literature (table 2.4), the specific heat values of PEI-600 and TEPA were considered to be 2440 J/kgK and 1890 J/kgK respectively.

$\dot{m}_{CO_2}$ AND $\dot{m}_{H_2O}$

Both these values could easily be calculated. The mass flow rate of sorbent (kg/s) was known and for a section on the plate, the weight of CO_2 or H_2O absorbed per weight of sorbent was found out from experiments. Multiplying these two quantities would result in amount of CO_2 or H_2O being absorbed in grams/s. Dividing by the respective molecular weight of CO_2 and H_2O, $\dot{m}_{CO_2}$ and $\dot{m}_{H_2O}$ could be calculated with the required units in mols/s.

$\Delta H_{abs,CO_2}$

It was found out that the ratio of H_2O to CO_2 absorbed was high. Therefore, the amount of water being absorbed by the sorbents used was much more than CO_2. Therefore, $\dot{m}_{CO_2}$ was in the order of 10^{-8} mol/s whereas $\dot{m}_{H_2O}$ was two orders higher at 10^{-6}. Since the contribution of $\dot{m}_{H_2O}\Delta H_{abs,H_2O}$ was very small, it was decided to use a value of -80 kJ/molCO_2 and -85 kJ/molCO_2 for PEI-600 and TEPA respectively based on literature (table 2.5). This decision was made considering the fact that since the concentration of CO_2 absorbed was very small, accurate values of heat of absorption of CO_2 would be difficult to find. The aim of the heat model was now be find the heat of absorption of water.

Q_{losses}

The heat losses due to conduction, convection and radiation were more complex to calculate. Therefore it was decided to model a cross-section of the plate and analyse the heat losses and apply the results to obtain these values.

5.1.4. MODEL TO CALCULATE HEAT LOSSES

In order to calculate the heat loss across the cross-section of the plate, a finite difference method for two dimensional steady conduction was applied by creating a mesh grid using MATLAB as shown in figure 5.4.

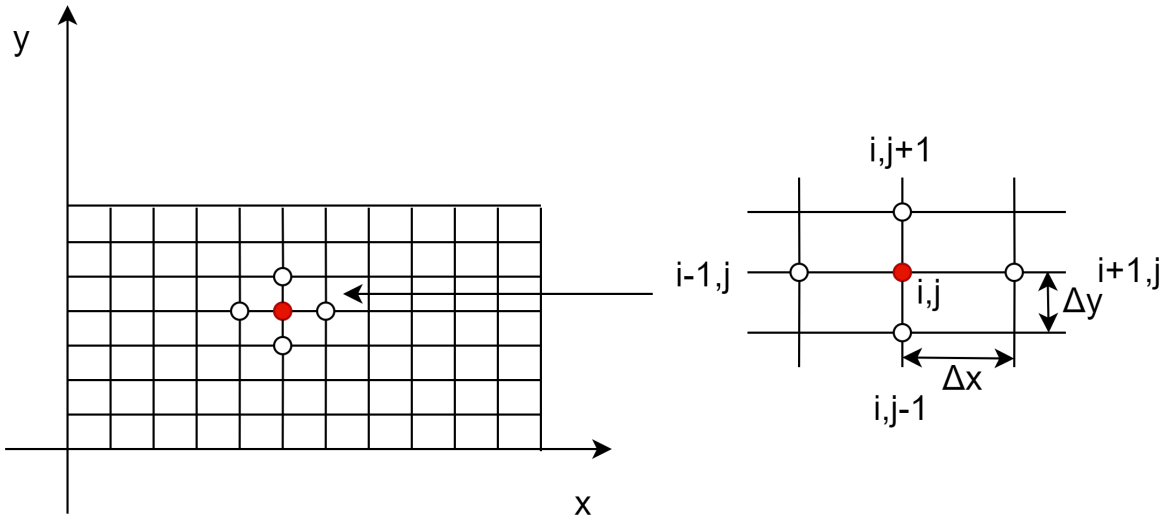

Figure 5.4: A depiction of a mesh grid similar to the one created in MATLAB

A similar grid matching the plate dimensions was made in MATLAB with the plate and grid factors shown in table 5.1.

Table 5.1: Plate and grid factors used

Plate and Grid Factors	
Plate width (a)	0.1 m
Plate height (b)	0.005 m
Resolution in x-direction	200
Resolution in y-direction	25
x	5e-4 m
y	2e-4 m
Thickness into the plane	1 m
Thermal conductivity of acrylic plate (k)	0.2 W/mK[93]
Top hc (convective + radiative)	calculated below
Bottom hc (convective + radiative)	10 $W/m2K$ (assumed 5 + 5)
T_external (T_e)	lab air temperature (deg C)

INITIAL CONDITIONS

As an initial condition, the entire grid was made to be equal to the temperature of the plate. This temperature could be found using the thermal image data collected during experiments. In addition, Dirichlet condition was applied at the cross-section of the channel [92]. The part of the grid representing the channel was made to be set at a temperature equal to the temperature of the sorbent. This temperature could also be found using the thermal data. As an example, the initial conditions can be seen in figure 5.5.

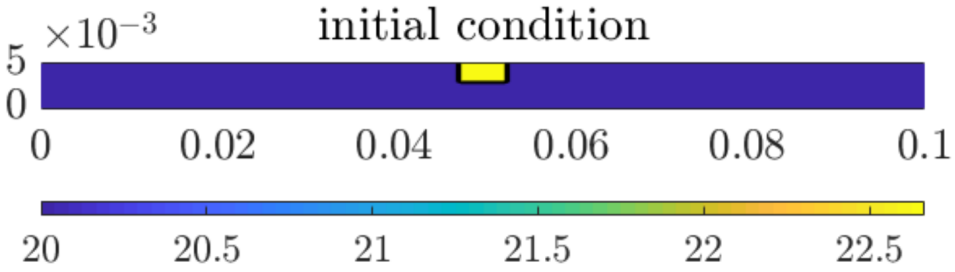

Figure 5.5: An example of initial condition applied in model with a colour map indicating temperature values

BOUNDARY CONDITIONS

While the loop to run the code was iterated, the Dirichlet condition on cross-section of the channel was satisfied each time. In addition, a convective boundary condition (mixed) was applied at the top and bottom part of the grid except the corners. As an example, consider figure 5.6 showing a section of the top part of the grid with convective boundary.

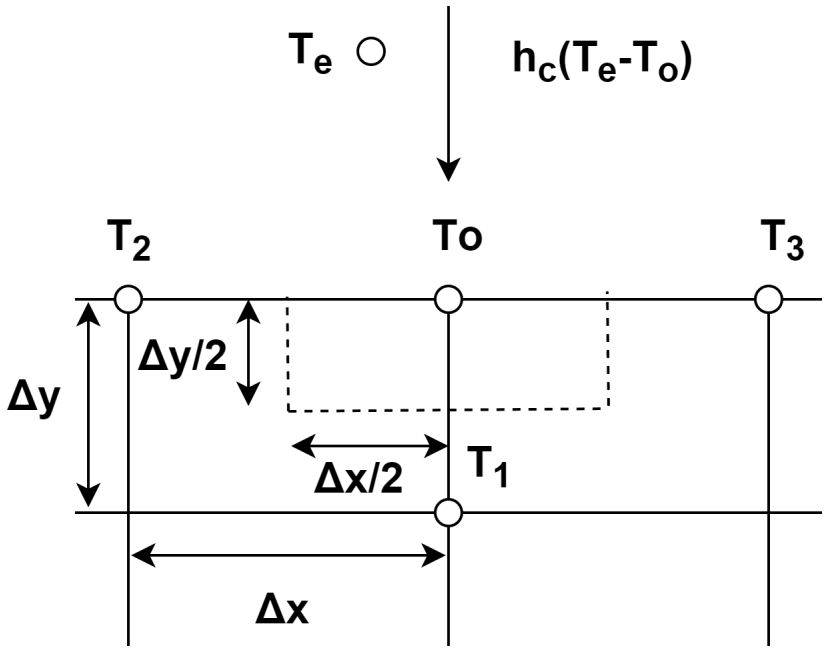

Figure 5.6: Top part of the grid depicting the boundary condition. For simplicity, temperatures are denoted as T_o, T_1, T_2 and T_3.

Considering point at T_o, the derivative of T(x,y) could be approximated by a linear temperature gradient between the nodes shown. Therefore, the heat transfer for each face could be written as follows [94][95].

$$\dot{Q}_x|_W = \frac{-k(T_o - T_2)}{\Delta x} . \frac{\Delta y.1}{2} \tag{5.5}$$

$$\dot{Q}_x|_E = \frac{-k(T_3 - T_o)}{\Delta x} . \frac{\Delta y.1}{2} \tag{5.6}$$

$$\dot{Q}_y|_S = \frac{-k(T_o - T_1)}{\Delta y} . \Delta x.1 \tag{5.7}$$

and

$$\dot{Q}_y|_0 = h_c(T_e - T_o).\Delta x.1 \tag{5.8}$$

Considering internal heat generation ($\dot{Q}_v'''$) to be zero, the energy balance states that the sum of the net heat conducted into the volume and heat convection across the face at y=0 should be equal to zero. Therefore, the following equation 5.9 was achieved.

$$\dot{Q}_x|_W + \dot{Q}_y|_S - \dot{Q}_x|_E + \dot{Q}_y|_0 = 0 \tag{5.9}$$

Solving equation 5.9, the value of T_0 satisfying the convective boundary condition can be achieved as shown in equation 5.10.

$$\boxed{T_o = \frac{1}{[(1+B_i)\Delta x^2 + \Delta y^2]}[(\frac{T_2+T_3}{2})\Delta y^2 + (T_1 + T_e.B_i)\Delta x^2]} \tag{5.10}$$

where $B_i = \frac{h_{ctop}\Delta y}{k}$ for the top boundary and $B_i = \frac{h_{cbot}\Delta y}{k}$ for the bottom boundary.

LOGIC

Once the plate and grid factors were fixed and the initial and boundary conditions were applied, the steady heat equation assuming no internal heat generation given in equation 5.11 below was applied to update all interior nodes in each iteration [94].

$$\frac{\partial^2 T}{\partial x^2} + \frac{\partial^2 T}{\partial y^2} = 0 \tag{5.11}$$

Considering an equidistant rectangular grid (x,y) of steps Δx and Δy shown in figure 5.4, Taylor series expansion can be used to approximate the terms mentioned in equation 5.11 such that

$$\frac{\partial^2 T(x,y)}{\partial x^2} = \frac{[T(i-1,j) + T(i+1,j) - 2T(i,j)]}{\Delta x^2} \tag{5.12}$$

and

$$\frac{\partial^2 T(x,y)}{\partial y^2} = \frac{[T(i,j-1) + T(i,j+1) - 2T(i,j)]}{\Delta y^2} \tag{5.13}$$

Substituting the values from equations 5.12 and 5.13 in equation 5.11, the equation to calculate $T(i.j)$ was found and is shown as equation 5.14.

$$\boxed{T(i,j) = \frac{[T(i,j-1) + T(i,j+1)].w_x + [T(i-1,j) + T(i+1,j)].w_y}{w_{xy}}} \tag{5.14}$$

where

$$\begin{aligned} w_x &= \frac{1}{\Delta x^2} \\ w_y &= \frac{1}{\Delta y^2} \\ w_{xy} &= \frac{2}{\Delta x^2} + \frac{2}{\Delta y^2} \end{aligned}$$

With each iteration, equation 5.14 was used to update all interior nodes in the grid while the corners nodes were smoothed simultaneously by averaging the adjacent nodes. Once a

steady state was achieved and each node assumed a constant temperature value, the model converged. A graph depicting convergence is shown in figure 5.7.

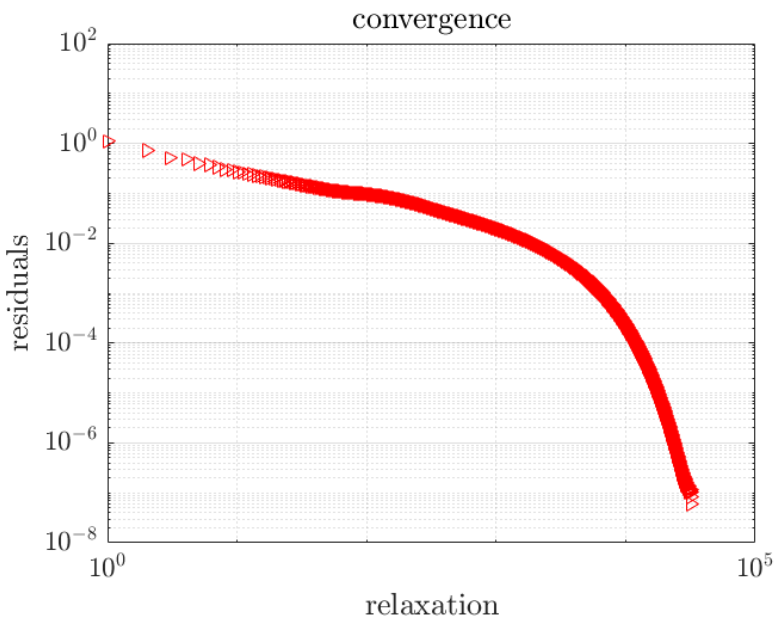

Figure 5.7: Graph depicting convergence of model

After convergence, an image similar to figure 5.5 was displayed depicting the heat transfer through the cross-section of the plate due to the sorbent flow in the channel. This is shown in figure 5.8.

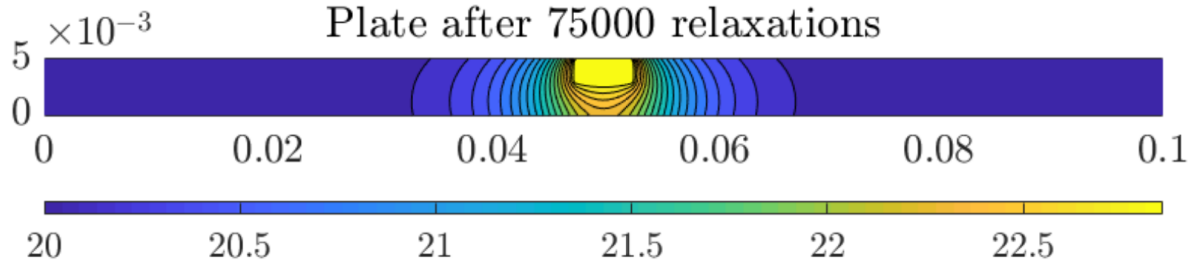

Figure 5.8: Depiction of heat transfer through the plate due to sorbent flow in the channel. A colour map is included which indicates temperature values

CALCULATION OF HEAT FLUX AND TOTAL HEAT TRANSFER

Once the model converged, the final temperatures of all the nodes in the grid were known. Now, the heat fluxes in the top, bottom, left and right direction were calculated. An example for calculation of outward boundary heat flux from left side of the plate cross-section is described below. Since $\Delta y \neq \Delta x$, equation 5.15 was used to calculate the outward boundary heat flux from the left boundary except for the corner points [94][95].

$$q_x = \frac{k\Delta x}{2}.[w_{xy}T(1,j) - 2w_xT(2,j) - w_y[T(i,j-1) + T(i,j+1)]] \tag{5.15}$$

For the corners, a different equation was applied. An example for the left bottom corner is shown in equation 5.16.

$$q_x(corner) = \frac{-k}{\Delta x}.[T(1,2) - T(1,1)] \tag{5.16}$$

Subsequently, the heat transfer through the left side was found out by adding all the flux and multiplying by the cross sectional area in the direction on the flux as shown in equation 5.17 where L was the chosen distance into the plane in meters.

$$Q_x = [\sum q_x].\Delta y.L \tag{5.17}$$

Similarly, the heat transfer from all the 4 sides was calculated and added with respective psoitive or negative signs to obtain the total heat transfer on a section of the plate (Q_{total}). This represented the total heat losses as $Q_{total} = Q_{losses}$ and therefore, it could be substituted in equation 5.4 to finally calculate the heat of absorption.

CONVECTIVE HEAT TRANSFER COEFFICIENT

During experiments, the top of the plate had a continuous air flow due to the fan and therefore, the heat transfer coefficient for the top surface of the plate was needed to be estimated in order to input it into the model described above. In order to estimate the convective heat transfer coefficient, a TESTO 445 flow sensor shown in figure 5.9 was used to measure the velocity of air flow at every 50 mm close to the channel on the plate used for experiments.

Figure 5.9: Flow sensor

The tip of the probe of flow sensor is heated and as air flows by, it is cooled and energy is lost. The circuit balance is disrupted and immediately, the circuit restores the lost energy by heating the flow sensor to compensate for the heat lost. The electrical power required to sustain the overheat is calibrated such that the air flow at that point is measured and displayed on the screen [96]. The air flow velocity as measured by this sensor is displayed in figure 5.10.

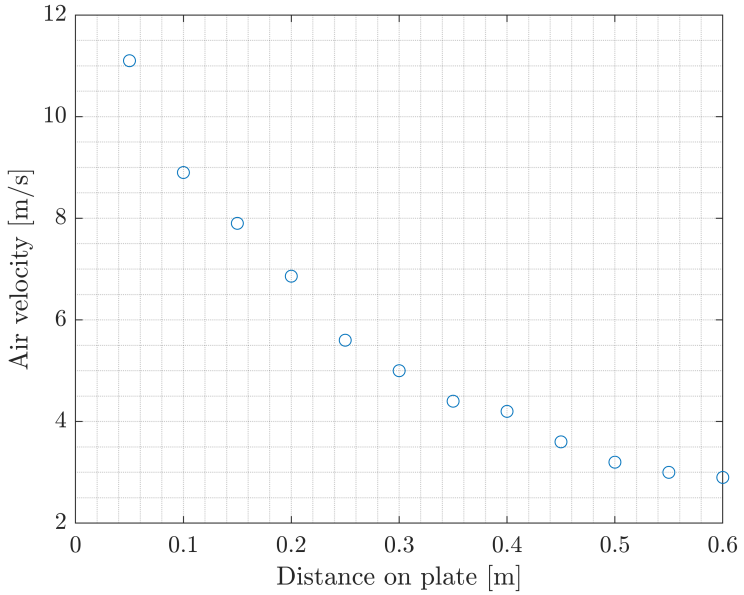

Figure 5.10: Air velocity measured at different points on the plate using TESTO 445 flow sensor. Note: the distance 0 m corresponds to the side at which the fan is situated and 0.6 m is where the channel connects to the syringe pump.

The air velocity was measured and in order to calculate convective heat transfer coefficient, the flow was considered to be a turbulent boundary layer flow. It was assumed that the velocity measured was the free stream velocity outside the boundary layer. Therefore, a corresponding Reynolds number was calculated for each data point from equation 5.18 [97].

$$Re_x = u_e x/\nu \tag{5.18}$$

where

Re_x	=	Reynold number at distance x on the plate
u_e	=	free stream velocity [m/s]
x	=	distance on the plate [m]
ν	=	kinematic viscosity of air $[m^2/s]$

Subsequently, the local skin friction coefficient (C_{fx}) for turbulent flow was calculated using equation 5.19 for $10^5 < Re_x < 10^7$ [97].

$$C_{fx} = 0.0592 Re_x^{-1/5} \tag{5.19}$$

With the values of local skin friction coefficients, for a range of Prandtl number $0.7 < Pr < 400$, local Stanton number could be calculated using equation 5.20 [97].

$$St_x = (\frac{C_{fx}}{2}) Pr^{-0.57} \tag{5.20}$$

From this local Stanton number, a local convective heat transfer coefficient was calculated for each data point from equation 5.21 [97].

$$h_c = St_x \rho c_p V \tag{5.21}$$

where

h_c = local convective heat transfer coefficient $[W/m^2K]$
St_x = local Stanton number
ρ = density of air $[kg/m^3]$
c_p = specific heat capacity of air [J/kgK]
V = local air velocity same as u_e [m/s]

Note: all fluid properties were obtained at 293.15 K [98]
Therefore, the local convective heat transfer coefficient was calculated and can be seen in figure 5.11.

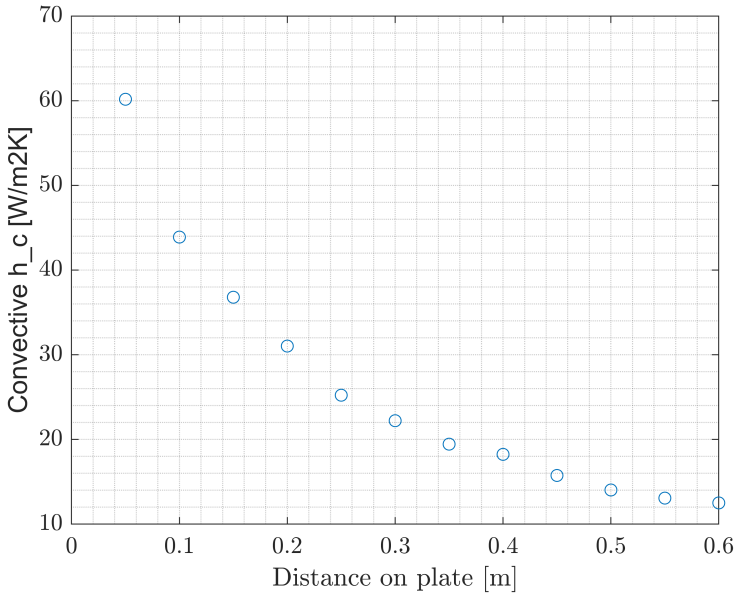

Figure 5.11: Calculated convective heat transfer coefficients at different points on the plate. Note: the distance 0 m corresponds to the side at which the fan is situated and 0.6 m is where the channel connects to the syringe pump.

5.1.5. ASSUMPTIONS

The heat model described in the sections above was intricate and some assumptions were made are listed below:

- An assumption of steady state was considered while formulating energy balance equations 5.1 and 5.11.
- The temperature at any cross-section of the sorbent in the channel was assumed to be constant throughout its fluid layer. A scaling using the Fourier number (F_o) was done to check the validity of this assumption. Fourier number is the the ratio of diffusive transport rate to the storage rate of heat and when $F_o = 1$, an equation, $t = L^2/\alpha$ can be achieved where

  t = characteristic time [s]
  L = length through which conduction occurs [m]
  α = thermal diffusivity $[m^2/s]$

An estimated layer thickness of sorbent (1 mm) was considered as a value for L and the thermal diffusivity of sorbent was estimated to be of the same order as that of water. This resulted in a characteristic time scale in the order of 1 second. Thus, it was inferred that it took the sorbent a matter of seconds to conduct heat through it's layer and since the time taken for the sorbent to flow through a section on the plate was in the order of minutes, this assumption was considered acceptable.

- The values of temperature used in the model were averages taken from the thermal data. For instance, for the initial condition of the MATLAB model, the temperature of the plate was found using the thermal data by taking the average of the plate section used to be analysed in the model. Similarly, the temperature of the sorbent used to enforce the Dirichlet boundary condition was also averaged over a section of the plate being considered in the model.

- In reality the sorbent flowing on the channel has a meniscus and is not flat at the top. However, since this meniscus was small and couldn't be measured, the model considers only a flat profile for the calculations.

- In reality, the channel was not filled entirely by the sorbent. However, for the ease of modelling, the entire channel height was considered full of sorbent.

- The convective heat transfer coefficient was calculated considering a turbulent boundary layer flow of air and the air velocity measured by the flow sensor was assumed to be free stream velocity. This was done to simplify the otherwise complex air flow through the fan. Since the values of convective heat transfer coefficient obtained were within the range of average heat transfer coefficients for forced convection through air (10-200 W/m^2K), the method used was considered acceptable [92][99].

- A radiation heat transfer coefficient of 5 W/m^2K was assumed for the top and bottom surfaces while a convective heat transfer coefficient of 5 W/m^2K was assumed for the bottom surface. These convective and radiative coefficients were added on the top and bottom surfaces and treated as an overall heat transfer coefficient in the model.

- The value for the heat of absorption selected for CO_2 for both PEI-600 and TEPA was considered to be constant throughout the model. However, literature (2.4.3) states that it can vary with temperature and loading of CO_2. Since the amount of CO_2 absorbed was very small as compared to water, this was also considered acceptable since it would not have much affect on the final value of heat of absorption of water that would be calculated.

5.2. MODELLING OF ABSORPTION COLUMN

To answer the final research question on designing an absorption column, a model depicting the absorption process was made. This section starts with the basic strategies used to model the absorption process and eventually goes in-depth into the assumptions and validation.

5.2.1. FUNDAMENTALS

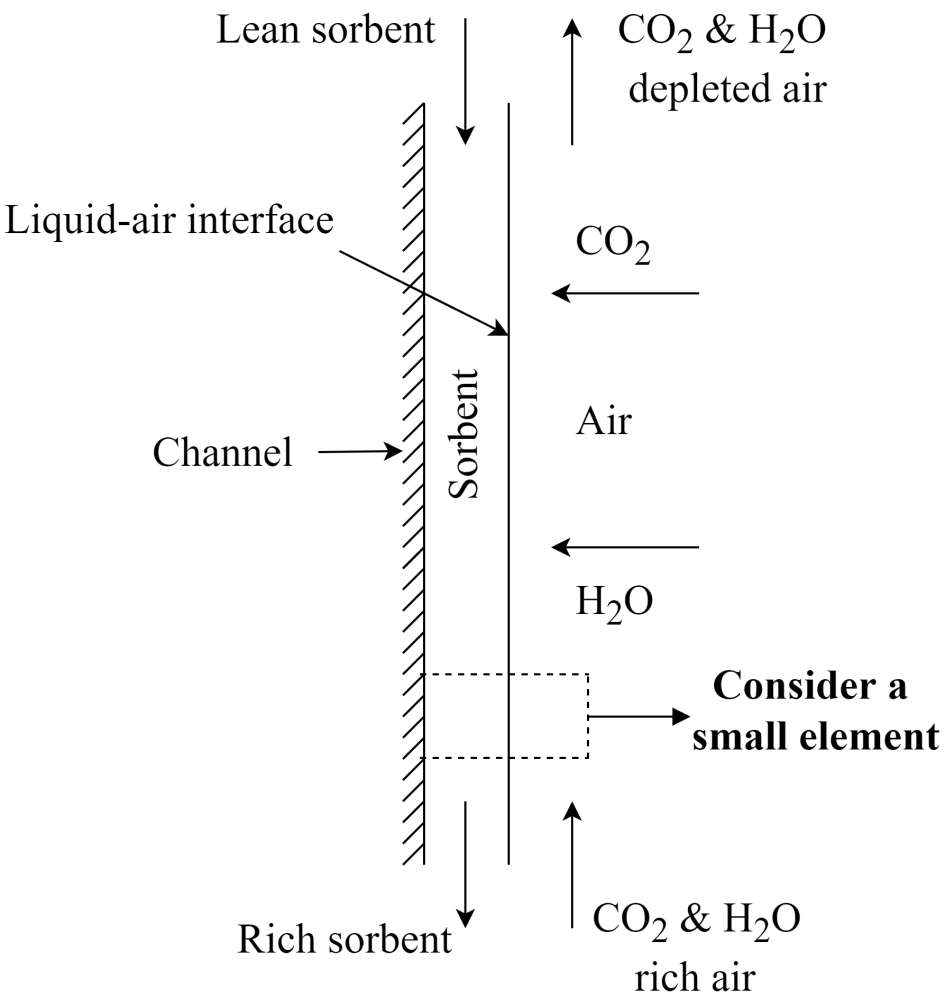

Figure 5.12: A basic schematic description of the absorption process

To model an absorption column, the fundamental aspects of the process are first discussed. Figure 5.12 schematically shows the downwards flow of a sorbent on a vertical channel with a counter-current airflow. The lean sorbent enters at the top of the channel absorbing CO_2 and H_2O from the air as it flows down, finally exiting as a rich sorbent. Similarly, the ambient air enters from the bottom and subsequently, drier air exits the system which is depleted of CO_2. Considering a small element shown in figure 5.12, a mass balance approach can be applied which is the foundation of this model.

5.2.2. MASS BALANCE

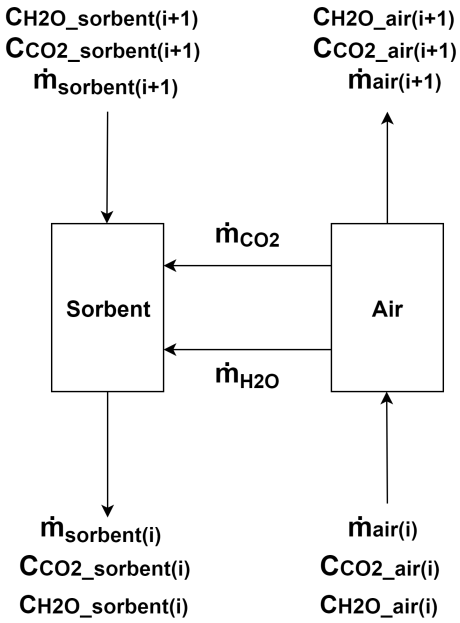

Figure 5.13: Zooming into the small element shown in figure 5.12

According to the law of conservation of mass, for any closed system, the net mass of the system remains constant over time. In other words, the quantity of mass is always conserved over time in a closed system [100][11]. The small element in figure 5.12 can be divided into two blocks - sorbent and air as shown in figure 5.13. The expansion of the notations used in figure 5.13 are given in table 5.2.

Table 5.2: Notation full forms

Notation	Full Form	Units
$\dot{m}_{sorbent}$	Mass flow rate of sorbent	kg/s
$\dot{m}_{air}$	Mass flow rate of air	kg/s
$\dot{m}_{CO_2}$	Mass flow rate of CO_2 from air into sorbent	kg/s
$\dot{m}_{H_2O}$	Mass flow rate of H_2O from air into sorbent	kg/s
$C_{H_2O\_sorbent}$	Concentration of water in sorbent	weight %
$C_{CO_2\_sorbent}$	Concentration of carbon dioxide in sorbent	weight %
$C_{H_2O\_air}$	Concentration of water in air	weight %
$C_{CO_2\_air}$	Concentration of carbon dioxide in air	weight %

Applying mass conservation on the element shown in figure 5.13, the sum of inputs of the system should be equal to the sum of outputs as seen in equation 5.22

$$\dot{m}_{sorbent(i+1)} + \dot{m}_{air(i)} = \dot{m}_{sorbent(i)} + \dot{m}_{air(i+1)} \tag{5.22}$$

For equation 5.22 to be true, the quantity of $\dot{m}_{air}$ and $\dot{m}_{H_2O}$ leaving the air should be equal to what is being absorbed by the sorbent. Therefore the following two equations hold true.

$$\dot{m}_{air(i+1)} = \dot{m}_{air(i)} - \dot{m}_{air} - \dot{m}_{H_2O} \tag{5.23}$$

$$\dot{m}_{sorbent(i)} = \dot{m}_{sorbent(i+1)} + \dot{m}_{air} + \dot{m}_{H_2O} \tag{5.24}$$

5.2.3. MODELLING STRATEGY

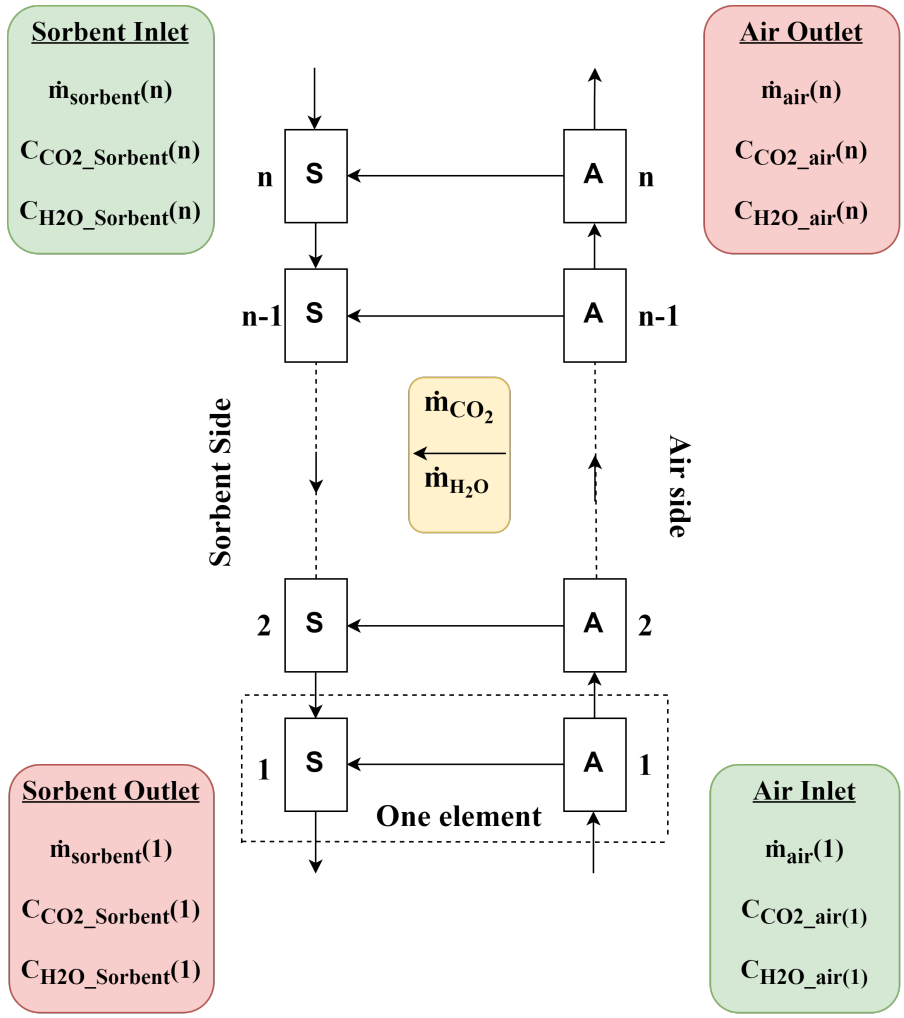

Figure 5.14: Visualisation of model through a schematic diagram

To model the absorption process, the flow depicted in figure 5.12 can be divided into multiple elements as seen in figure 5.14. The blocks named "S" correspond to the sorbent while "A" stands for air. The model starts with the last element marked with a dotted rectangle. Each element is made is to satisfy conservation of mass by applying equations 5.23 and 5.24, the outputs are updated and the model moves to the next element applying the same procedure. The process continues until a steady state is detected. To achieve this certain initial and boundary conditions are applied. Before describing these conditions, first the assumptions pertaining to this particular model are mentioned.

5.2.4. ASSUMPTIONS

The following assumptions should be kept in mind before understanding the model.

- The air flow is considered well mixed. In other words, the concentration of CO_2 and H_2O in air is considered to be homogeneously spread in air in each element.
- A concentration of 412 ppmv (parts per million by volume) [3] for CO_2 and 19536 ppmv for water is considered in ambient air. The value of ppmv of water comes from assuming an average relative humidity of 83% in Netherlands [101].
- $\dot{m}_{air}$ and $\dot{m}_{H_2O}$ in each element is calculated using the space time yield found by experiments done earlier. Although, as air would move up the column, the concentration of CO_2 and H_2O will gradually deplete in the airside due to absorbtion by the sorbent resulting in the decrease of their respective partial pressures. Thus, the mass transfer to the sorbent side should decrease according to Henry's law (section 2.3.1). Since the space-time yield found using experiments was under conditions where CO_2 and H_2O were not being depleted, using the same space-time yield here would not yield accurate results. Therefore, since Fick's law of diffuson dictates that mass transfer in molecular diffusion is proportional to the concentration gradient [11], a linear correction factor is employed to correct the space-time yield governing the mass transfer to account for mass transfer loss due to Henry's law (section 2.3.2).
- Viscosity changes due to absorption of CO_2 and H_2O and concentration gradients within the sorbents are not considered and it is assumed at all times that the concentration of CO_2 and H_2O are homogeneous within a sorbent element. Therefore, this model doesn't look into the diffusion of CO_2 into the sorbent layers. This assumption can be validated by the fact that the experiments were done by finding the average concentration and not layer-wise concentration in each element considered in the experiments.

5.2.5. CONDITIONS

Some conditions need to be applied in order to make a physically correct model.

BOUNDARY CONDITIONS

The mass flow of the air inlet is always constant and the same is true for the sorbent inlet. In addition, the concentration of CO_2 and H_2O in the air and sorbent inlet are also constant. Considering n number of elements as shown in figure 5.14, we have the following boundary conditions describing the air inlet:

$$\dot{m}_{air}(1) = \dot{m}_{air}(inlet) \tag{5.25}$$

$$C_{CO_2\_air}(1) = C_{CO_2\_air}(inlet) \tag{5.26}$$

$$C_{H_2O\_air}(1) = C_{H_2O\_air}(inlet) \tag{5.27}$$

Similarly, the boundary conditions for the sorbent inlet are as shown below.

$$\dot{m}_{sorbent}(n) = \dot{m}_{sorbent}(inlet) \tag{5.28}$$

$$C_{CO_2\_sorbent}(n) = C_{CO_2\_sorbent}(inlet) \tag{5.29}$$

$$C_{H_2O\_sorbent}(n) = C_{H_2O\_sorbent}(inlet) \tag{5.30}$$

INITIAL CONDITIONS

The initial condition in this model implies that the mass flow, concentration of CO_2 and H_2O are same for the first iteration in the air side and sorbent side respectively.

$$\dot{m}_{air}(1,2...n) = \dot{m}_{air}(inlet) \tag{5.31}$$

$$C_{CO_2\_air}(1,2...n) = C_{CO_2\_air}(inlet) \tag{5.32}$$

$$C_{H_2O\_air}(1,2...n) = C_{H_2O\_air}(inlet) \tag{5.33}$$

$$\dot{m}_{sorbent}(1,2...n) = \dot{m}_{sorbent}(inlet) \tag{5.34}$$

$$C_{CO_2\_sorbent}(1,2...n) = C_{CO_2\_sorbent}(inlet) \tag{5.35}$$

$$C_{H_2O\_sorbent}(1,2...n) = C_{H_2O\_sorbent}(inlet) \tag{5.36}$$

LOGIC

The model takes the length of channel, total area of flow and the space-time yields of CO_2 and H_2O as inputs. Once the initial and boundary conditions are employed, the model iterates starting from the bottom element to the top one. This process continues until a steady state is reached implying that the concentrations and the mass flow of both the air and sorbent side don't change anymore.

A space-time yield for CO_2 and H_2O, obtained from the experiments is used to calculate the mass transfer of carbon dioxide ($\dot{m}_{CO_2}$) and water ($\dot{m}_{H_2O}$) in each element. This space-time yield has the unit of $mols/m^2s$ and is converted into kg/s by multiplying by the molecular weight of the species and the area of each element. In addition, a correction factor following Fick's law of diffusion, mentioned in **??**, is multiplied to account for loss in mass transfer due to decreasing concentration of CO_2 and H_2O on the air side. This factor is $\frac{C_{CO_2\_air}(i)}{C_{CO_2\_air}(inlet)}$ and $\frac{C_{H_2O\_air}(i)}{C_{H_2O\_air}(inlet)}$ at the i^{th} element for space-time yield of CO_2 and H_2O respectively. Thereafter, equations 5.23 and 5.24 are applied and concentrations of CO_2 and H_20 are updated after each iteration in air and sorbent side.

5.2.6. MODEL VALIDATION

The experiments done by using Pure TEPA as a sorbent yielded the best space-time yield and thus, it will be used to design the absorption column. Before designing the absorption column, it is wise to validate the model with the experimental results. The experiment was done by a continuous fan air flow such that there was no local depletion of CO_2 or H_2O in the air. In order to imitate the same conditions in the model, a very large mass flow of air equal to 55.55 kg/s is applied to the model to make sure that the depletion of CO_2 and H_2O is neglible. The model verifies this assumption and it can be seen in figure 5.15 that the depletion of the two species is miniscule enough to neglect.

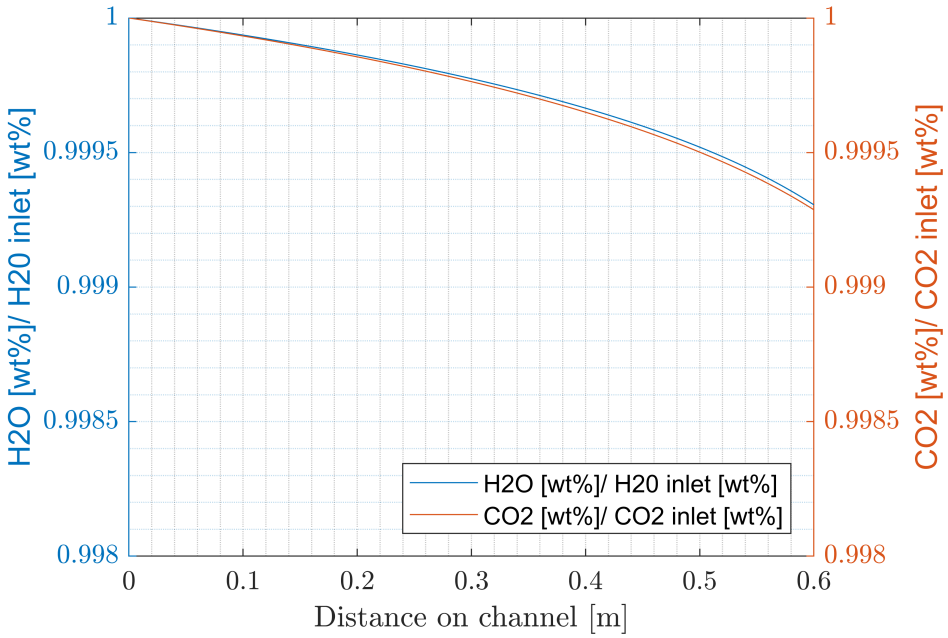

Figure 5.15: Graph depicting depletion of CO_2 and H_2O in air side along the channel

The starting concentration for the test done on Pure TEPA was 0% H_2O and 0.13% CO_2 as weight percentages. The same concentrations were fed to the model, with the length of the channel equal to 0.6 meters and mass flow of sorbent similar to the experiment. The results in comparison are shown in table 5.3 below.

Table 5.3: Model predictions vs experimental results in case of Pure TEPA as a sorbent

Distance on channel(m)	**Experimental Results**		**Model Predictions**	
	H2O (wt%)	**CO2 (wt%)**	**H2O (wt%)**	**CO2 (wt%)**
0	0	0.13	0	0.13
0.05	5.01	0.54	4.44	0.34
0.15	8.43	0.74	10.09	0.62
0.25	10.56	0.85	13.76	0.81
0.35	14.12	1.05	16.44	0.94
0.45	18.11	1.01	18.5	1.05
0.55	20.7	0.98	20.17	1.14

Figures 5.16 and 5.17 show the experimental results vs model predictions for H_2O and CO_2 concentrations respectively. In figure 5.16, the mean absolute error (MAE) is 1.23 and coefficient of deviation (R^2) is 0.94. In figure 5.17, MAE is 0.095 and R^2 is 0.853.

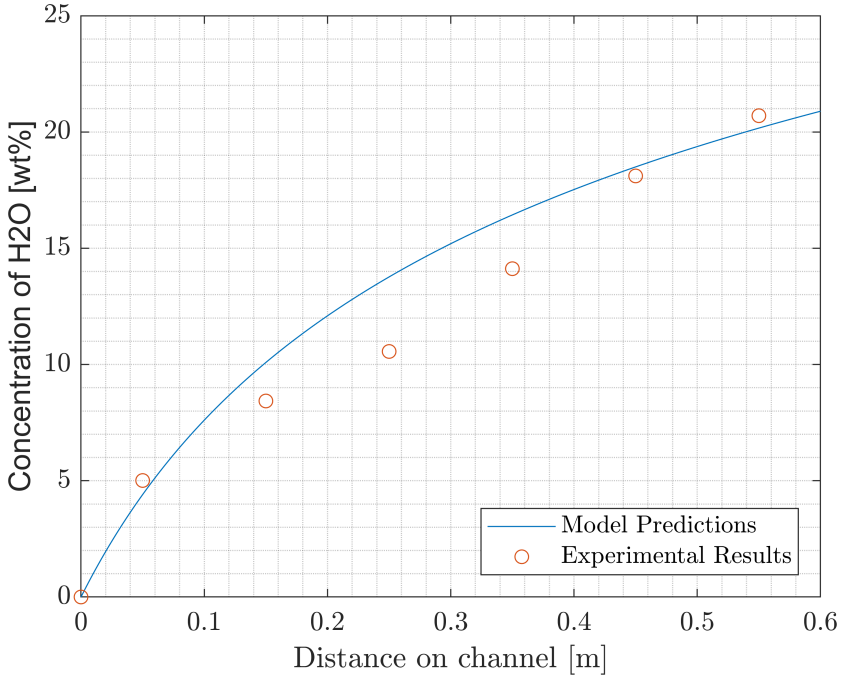

Figure 5.16: Model vs Predictions (H2O)

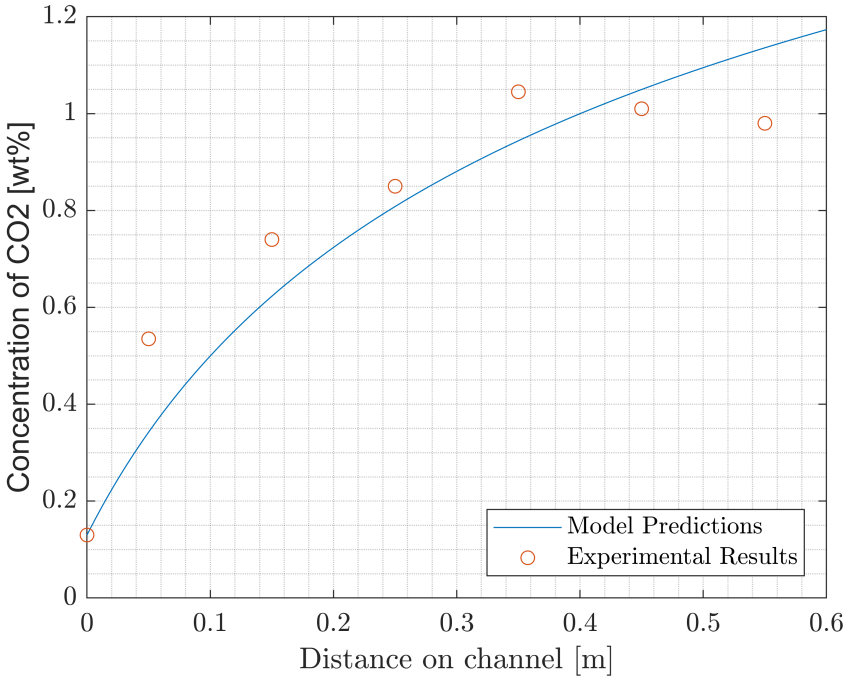

Figure 5.17: Model vs Predictions (CO2)

6

RESULTS AND CONCLUSIONS

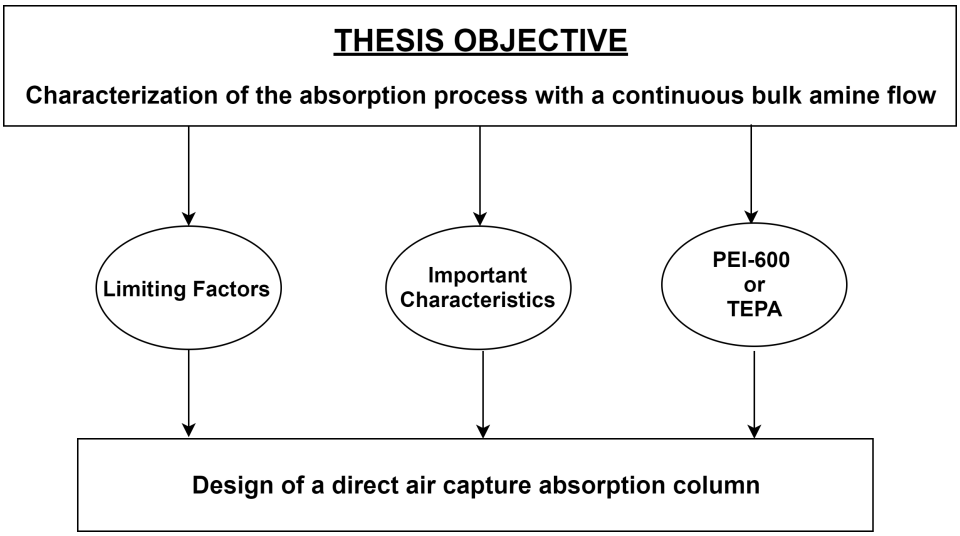

Figure 6.1: Research objectives

The main objective of this thesis was to characterize the absorption process in a continuous bulk amine flow. This thesis aimed at finding the important characteristics of a novel direct air capture process, the limiting factors and making a choice between the two sorbents being used by ZEF. Based on all the knowledge obtained, the final goal was to design an absorption column meeting ZEF's requirement. The flow of knowledge accumulation pertaining to this thesis is depicted in figure 6.1. This chapter discusses the results obtained during this thesis and draws conclusions based on the data. Each section in this chapter discusses a subsection of the research objective in detail in order to make it very clear to the reader and future researchers.

6.1. IMPORTANT CHARACTERISTICS

This section discusses many important characteristics of absorption that were studied in this thesis.

6.1.1. ABSORPTION PERFORMANCE PARAMETERS

During absorption the sorbents are used capture both CO_2 and H_2O. Therefore, the performance of PEI-600 and TEPA with regards to the absorption process can be described by the following parameters:

1. **CO_2 or H_2O absorbed per sorbent used (weight ratio).**
   This performance parameter decreases with increasing mass flow rate of sorbent and increases with decreasing mass flow rate of the sorbent. **Since the mass flow of sorbent can be controlled, this parameter can be controlled for any specific sorbent in an absorption column.** Considering a fix mass flow rate of sorbent of 0.08 ml/min ($1.33e^{-6}$ kg/s), table 6.1 summarizes this data for all sorbents used at 600 mm (end of channel).

2. **Space time yield - CO_2 ($molCO_2/m^2s$) and H_2O ($molH_2O/m^2s$)**
   This parameter is specific for each type of sorbent and unless the sorbent is continously mixed while flowing in the channel, the average space time yield for any specific sorbent would be the same. This parameter is not affected by the mass flow rate of the sorbent. **This parameter can be viewed as a mass transfer coefficient necessary in designing an absorption column.** The average space time yields for all sorbents used are summarized in table 6.2.

Table 6.1: CO_2 and H_2O per sorbent captured with different types of sorbents used. This data is calculated through identical experiments with a mass flow rate of sorbent of $1.33e^{-6}$ kg/s

Sorbent Details		**Weight Ratio at 600 mm**	
Type	**Initil concentration of sorbent**	**CO_2/sorbent**	**H_2O/sorbent**
PEI-600	0% H2O , 0% CO2	0.01	0.21
PEI-600	10% H2O , 0% CO2	0.009	0.33
PEI-600	20% H2O , 0% CO2	0.0075	0.55
PEI-600	30% H2O , 0% CO2	0.0065	0.502
TEPA	**0% H2O , 0% CO2**	**0.012**	**0.264**
TEPA	10% H2O , 0% CO2	0.0075	0.381
TEPA	20% H2O , 0% CO2	0.0063	0.523
TEPA	30% H2O , 0% CO2	0.005	0.608

Table 6.2: Average Space Time Yields for CO_2 and H_2O for all sorbents experimented upon

Sorbent Details		**Average Space Time Yields**	
Type	**Initial concentration of sorbent**	**$[molCO_2/m^2s]$**	**$[molH_2O/m^2s]$**
PEI-600	0% H2O , 0% CO2	$1e^{-4}$	0.006
PEI-600	10% H2O , 0% CO2	$1e^{-4}$	0.005
PEI-600	20% H2O , 0% CO2	$0.85e^{-4}$	0.005
PEI-600	30% H2O , 0% CO2	$0.6e^{-4}$	0.0014
TEPA	**0% H2O , 0% CO2**	$2e^{-4}$	**0.012**
TEPA	10% H2O , 0% CO2	$1.3e^{-4}$	0.01
TEPA	20% H2O , 0% CO2	$1.1e^{-4}$	0.008
TEPA	30% H2O , 0% CO2	$0.85e^{-4}$	0.003

CONCLUSION

Based on the absorption performance parameters, the following conclusions can be drawn:

1. TEPA with initial concentration of 0% CO_2 and 0% H_2O showed the best space time yield for both CO_2 and H_2O capture among all sorbents that were experimented upon.

2. TEPA with different initial concentrations was found to have a better CO_2 space time yield as compared to PEI-600 with corresponding initial concentrations.

3. Comparing all initial concentrations of PEI-600 and TEPA, TEPA with 0% CO_2 and 0% H_2O yielded the highest amounts of CO_2 captured per amine used while the mass flow rate of sorbent was kept constant for all experiments.

4. Similar to the CO_2 loading experiments (3.3.3), the overall performance of TEPA was found to be better than PEI-600 pertaining to rate of CO_2 capture.

5. Contrary to the CO_2 loading experiments performed in section 3.3, addition of water to the sorbents does not aid in significant CO_2 capture. In fact, a decreasing trend in the space time yields is observed as the initial water concentration is increased. This results can be attributed to a significant difference in the two experiments. The CO_2 loading experiments were a bulk phenomena where pure CO_2 was bubbled through the sorbents and physical solubility of CO_2 played a major role. However, the channel experiments was a surface phenomena where the absorption was taking place only at the surface and not in the bulk of the sorbent. Due to the limitations of data, further research is required to investigate this phenomena.

6.1.2. SENSITIVITY ANALYSIS

Apart from the absorption performance parameters described in 6.1.1, other factors like mass flow of air and sorbent were also found to influence absorption. In order to describe how these parameters influence absorption, consider a base case scenario for TEPA where all parameters are fixed in the absorption model. The effects of varying the mass flow rate of sorbent and air are described in the sections below by varying only the mass flow rate of sorbent and air respectively.

VARYING MASS FLOW RATE OF SORBENT

To describe the effects of varying the mass flow rate of air, the base case is compared with the same system with a 10 times higher mass flow rate of sorbent.

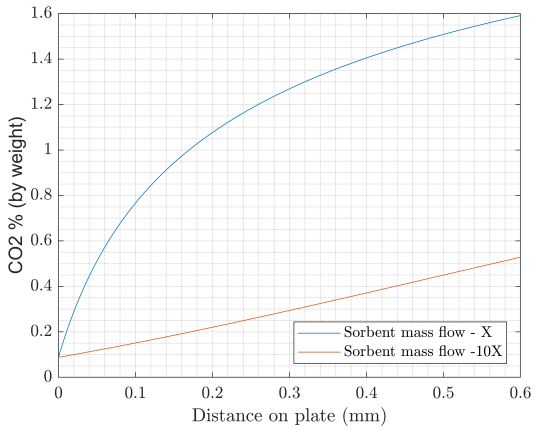

Figure 6.2: CO_2 concentration in sorbent through 0.6 m column with 2 different mass flow rates of sorbent

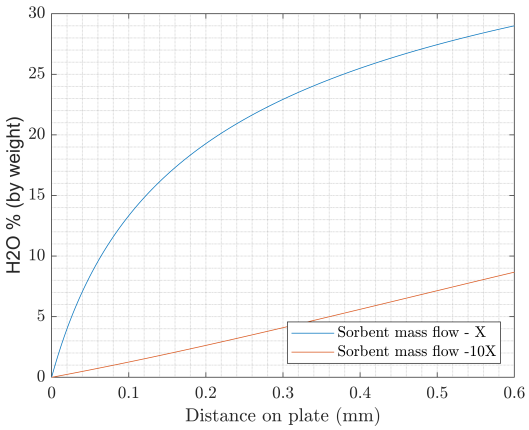

Figure 6.3: H_2O concentration in sorbent through 0.6 m column with 2 different mass flow rates of sorbent

It can be seen from figures 6.2 and 6.3 that the concentration of both CO_2 and H_2O decreases in the sorbent if the mass flow rate of the sorbent is increased. However, the absolute amount of CO_2 and H_2O absorbed is found to be higher for a higher mass flow rate of sorbent.

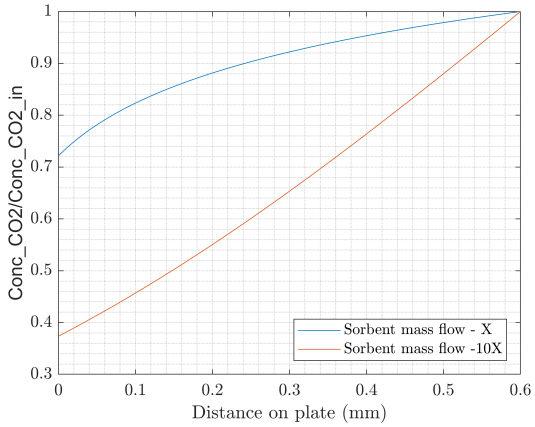

Figure 6.4: The ratio of current CO_2 concentration to the inlet CO_2 concentration in air through 0.6 m column with 2 different mass flow rates of sorbent

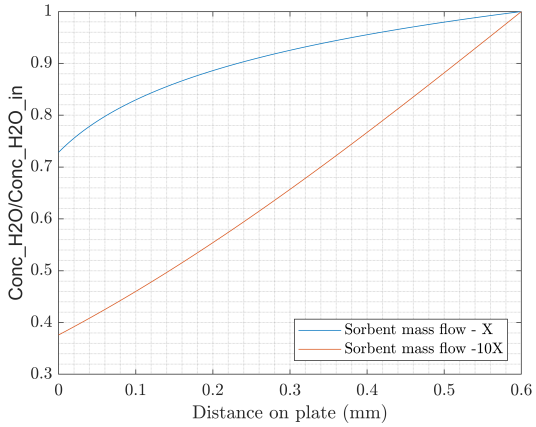

Figure 6.5: The ratio of current H_2O concentration to the inlet H_2O concentration in air through 0.6 m column with 2 different mass flow rates of sorbent

Since the absolute amount of CO_2 and H_2O increases with increasing mass flow rate of sorbent, it was found that the depletion of CO_2 and H_2O in the air is higher when the mass flow rate of air is kept constant and the mass flow rate of sorbent is increased. This can be seen in figures 6.4 and 6.5.

VARYING MASS FLOW RATE OF AIR

To describe the effects of varying the mass flow rate of air, the base case is compared with the same system with a 10 times lesser mass flow rate of air.

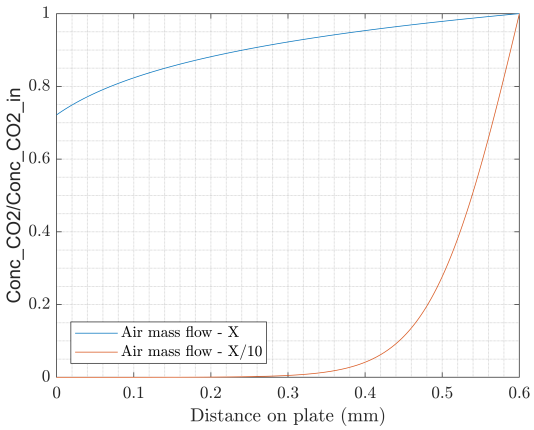

Figure 6.6: The ratio of current CO_2 concentration to the inlet CO_2 concentration in air through 0.6 m column with 2 different mass flow rates of air

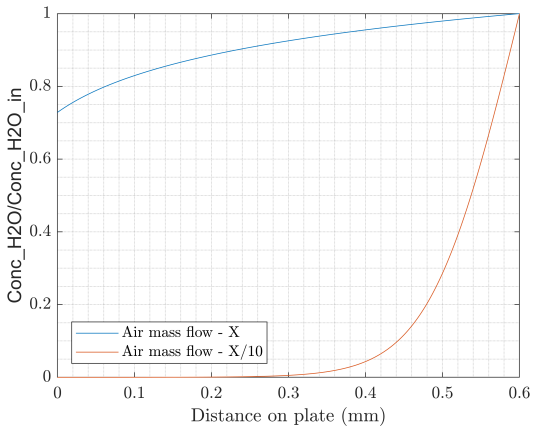

Figure 6.7: The ratio of current H_2O concentration to the inlet H_2O concentration in air through 0.6 m column with 2 different mass flow rates of air

It can be seen from figures 6.6 and 6.7 that the decreasing the mass flow rate of air and keeping other parameters constant, the air becomes more depleted with CO_2 and H_2O and as a result the driving force required for absorption goes down.

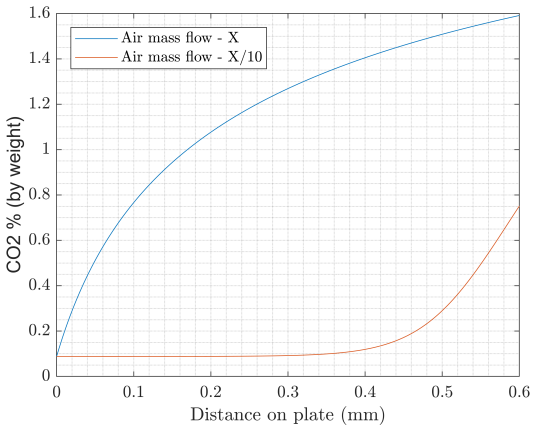

Figure 6.8: CO_2 concentration in sorbent through 0.6 m column with 2 different mass flow rates of air

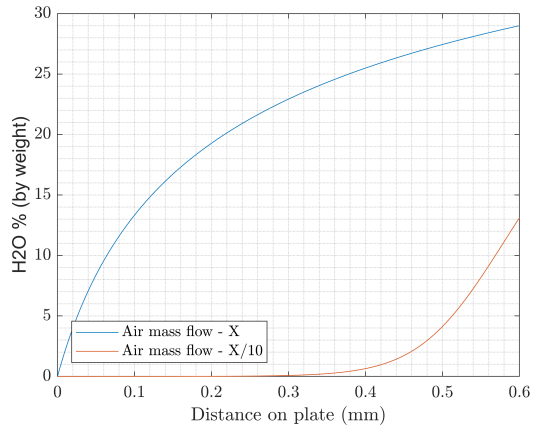

Figure 6.9: H_2O concentration in sorbent through 0.6 m column with 2 different mass flow rates of air

As a result of depletion of air, the concentrations of CO_2 and H_2O in the sorbent decreases. In fact, if the mass flow of air is lowered enough, the top part of the channel would not be able to absorb any CO_2 or H_2O due to depletion of air in the bottom part of the channel. This can be seen in figures 6.8 and 6.9.

6.1.3. HEAT OF ABSORPTION OF WATER

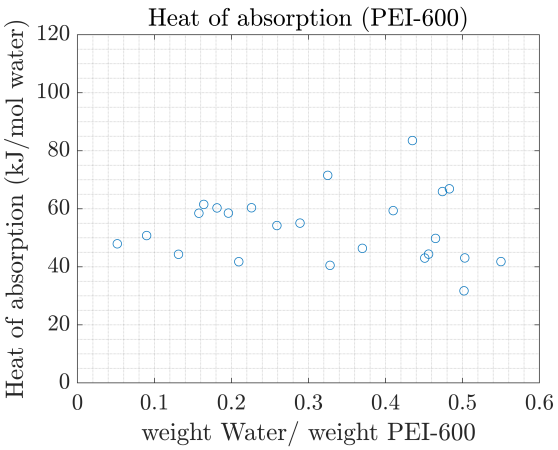

Figure 6.10: Heat of absorption of water in PEI-600 at all water concentrations pertaining to the experiments conducted

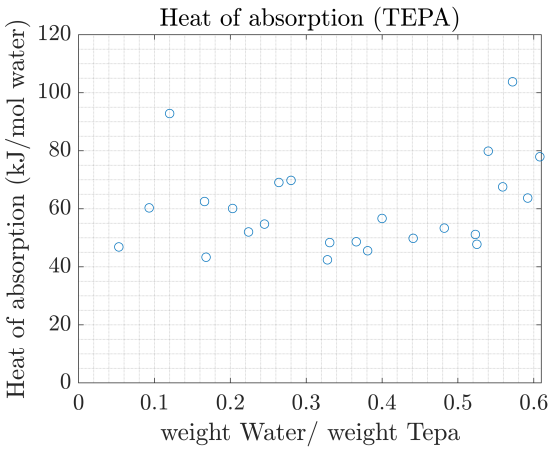

Figure 6.11: Heat of absorption of water in TEPA at all water concentrations pertaining to the experiments conducted

Based on section 5.1, heat of absorption of water was calculated for PEI-600 and TEPA at different weight ratios of water to sorbent which can be seen in figures 6.10 and 6.11. The average values with the errors can be seen in table 6.3.

Table 6.3: Average heat of absorption of water with standard error and error percentage

Average Heat of absorption of water [kJ/molH2O]	53.4 (PEI-600)	60.3 (TEPA)
Standard Error [kJ/molH2O]	2.4	3.2
Error %	4.5	5.3

CONCLUSION

Since the values of heat of absorption of water obtained for PEI-600 and TEPA are higher than the latent heat of water (table 2.3), this indicates that heat of mixing, forming and breaking of hydrogen bonds also add to the heat of absorption of water. Although, this might not be as useful for absorption point of view, while desorbing this would have direct influence on the heat required to regenerate the amine.

6.2. LIMITING FACTORS OF THE ABSORPTION PROCESS

This section discusses the major limiting factors of the absorption process found during this thesis.

6.2.1. DIFFUSION OF CO_2 IN THE SORBENT LAYERS

One of the most crucial factor that was found to affect the absorption process during this thesis was diffusion of CO_2 into the sorbent layers.

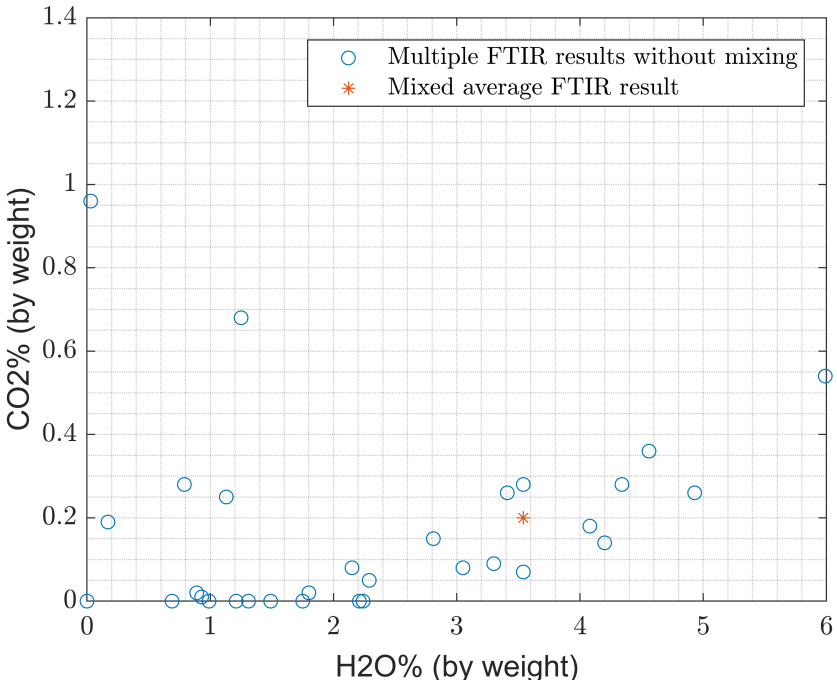

Figure 6.12: FTIR results of PEI-600 over a section of 0-100 mm on the channel: Figure depicts average concentration vs a layered concentration for two identical experiments on PEI-600

Figure 6.12 represents the CO_2 and H_2O concentrations of PEI-600 in the first 100 mm section of the plate through two identical experiments. One of these experiments was done following the usual methodology of experiments and an average concentration was found out by mixing the entire sample from the 100 mm section beforehand and performing FTIR measurement to obtain an average concentration of CO_2 and H_2O over the 100 mm section considered. However in the second experiment, the entire sample collected from the 100 mm section of the channel was not mixed and was measured in the FTIR drop by drop. Thus, multiple measurements yielded multiple concentrations of CO_2 and H_2O for the same 100 mm section of the channel.

CONCLUSION

Although, there are a few outliers in the figure 6.12, it can be concluded that the absorption of CO_2 is a layered effect. In other words, CO_2 and H_2O are absorbed in the top surface and are slowly diffused through the layers of the sorbent. Since, there are many data points lower that the average concentration and in fact, even with no CO_2 or H_2O, it indicates that a significant part of the bottom layer of the sorbent is not being used to absorb CO_2 or H_2O. Similarly, some data points are above the average concentration of sorbent indicating a higher concentration of CO_2 and H_2O in the top layers of the sorbent. **Therefore, it can be concluded that the absorption process is limited by diffusion on the sorbent side.**
In order to give further merit to the conclusion made above, an experiment was done using the same setup on TEPA with one key difference. 3D printed blocks were used as bridges or obstacles every 100 mm on the channel, covering a certain depth of the channel as shown in figure 6.13.

Note: This experiment was only performed to prove that the absorption process was limited due to diffusion on the sorbent side.

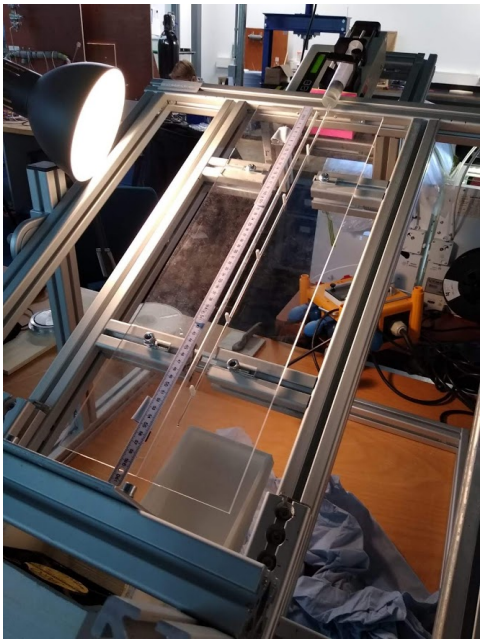

Figure 6.13: Experimental setup with 3d printed bridges or obstructions to induce mixing

It was expected that the top layer of the sorbent might be blocked by the 3D printed bridges giving way to a fresher layer on the top surface. Therefore, if the experiment was a success, diffusion could be countered by induced mixing effects.

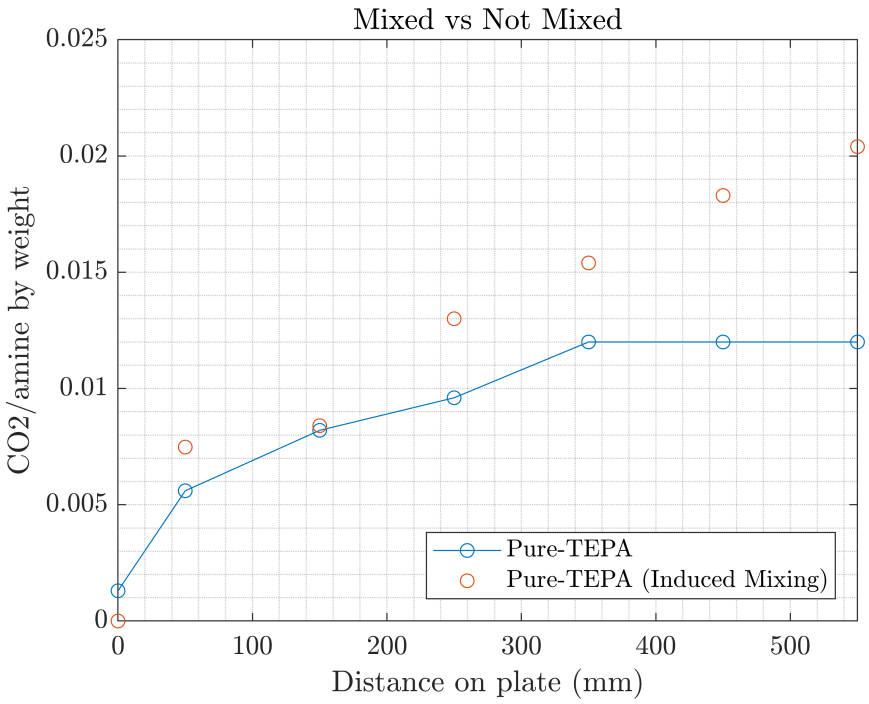

Figure 6.14: Graph representing weight of CO_2 captured per weight of TEPA used. A comparison was made between a normal experiment without mixing and identical experiment with induced mixing.

Figure 6.14 shows the results of the experiment done with induced mixing and and without mixing. It was observed that the experiment with induced mixing performed much better in terms of CO_2 captured per TEPA used. To quantify the performance, table 6.4 shows the average space time yields of the induced mixing experiment as an comparison with experiment done without mixing.

Table 6.4: Average Space Time Yields

Type	**Space Time Yield** $[molCO_2/m^2s]$
TEPA (no mixing)	$2e^{-4}$
TEPA (induced mixing)	$3.8e^{-4}$

Therefore, diffusion on the sorbent side is one of the main limiting factor in the direct air capture absorption process.

6.2.2. MASS FLOW RATE OF SORBENT

Another limiting factor in the absorption process was the mass flow rate of the sorbent. Figure 6.15 shows the weight ratio CO_2 absorbed per sorbent through a channel with a length of 0.6 m. Two different mass flow rates of PEI-600 mentioned in the figure were used to demonstrate the results.

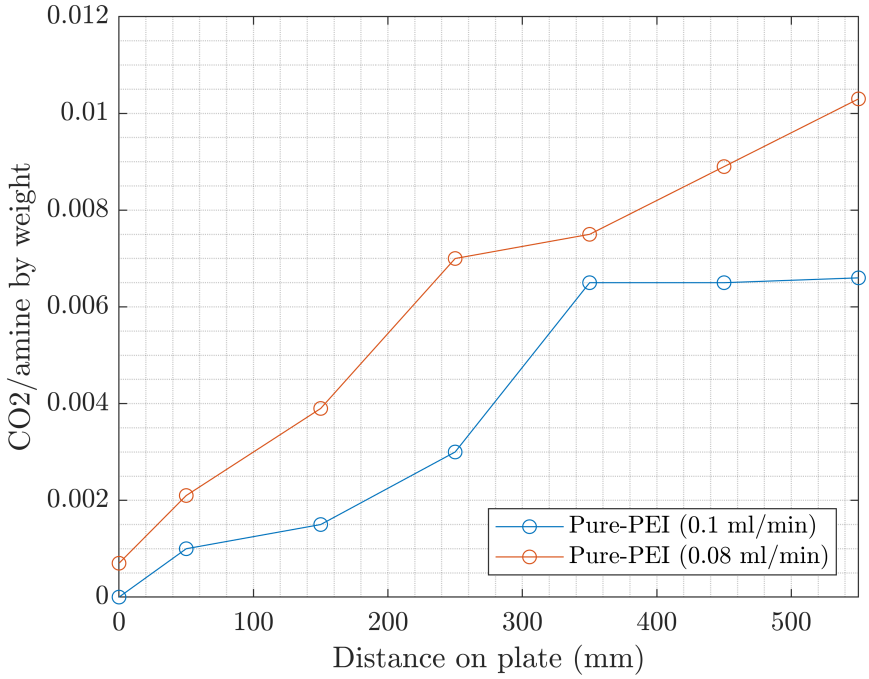

Figure 6.15: Experimental results of PEI-600 with varying mass flow rate of the sorbent

CONCLUSION

It was concluded that as the mass flow rate of the sorbent is increased, the amount of CO_2 captured per sorbent used decreased. Therefore, a lower mass flow rate of sorbent would

result in a higher amount of CO_2 captured per sorbent used. Having said that, in principle, the space time yield or the CO_2 capture rate should be the same in both cases as it is independent of the mass flow rate and this can be seen from the table 6.5.

Table 6.5: Average Space Time Yields

Type	**Space Time Yield** $[molCO_2/m^2s]$
PEI-600 (0.08ml/min)	$1e^{-4}$
PEI-600 (0.1ml/min)	$0.92e^{-4}$

Although, the space time yield is an important performance parameter, efficiency of absorption can also be defined in terms of CO_2 captured per sorbent used. Therefore, the mass flow rate of the sorbent becomes a limiting factor in the absorption process.

6.2.3. MASS FLOW RATE OF AIR

Similar to the mass flow rate of sorbent, the mass flow rate of air is also a limiting factor in the absorption process.

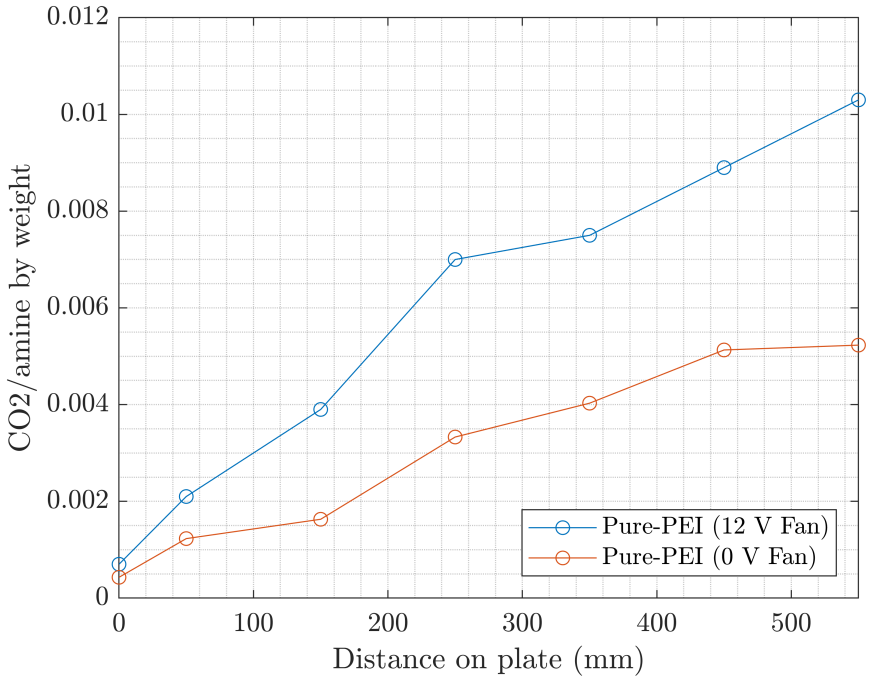

Figure 6.16: Experimental results of PEI-600 with varying mass flow rates of air

Figure 6.16 shows the results of two experiments done on PEI-600. One experiment was performed with a fan operating at 12V and the other was performed without a fan. In all other aspects, the experiments were identical.

CONCLUSION

From figure 6.16, it can be seen that the amount of CO_2 absorbed per sorbent used was much higher for a higher air mass flow rate. However, this is not the conclusion. The figure above actually depicts that without an air flow, CO_2 is locally depleted throughout the

channel whereas with an air flow rate, the depletion is lesser until a high enough mass flow of air is reached when there is no depletion of CO_2. This is also true for water. Unlike the mass flow rate of sorbent, lowering the mass flow rate of air lowers the space time yield of the sorbent being used since depletion causes the driving force for absorption to decrease. The average space time yields of the two experiments described above are shown in table 6.6.

Table 6.6: Average Space Time Yields

Type	**Space Time Yield** $[molCO_2/m^2s]$
PEI-600 (12V Fan)	$1e^{-4}$
PEI-600 (0V Fan)	$0.8e^{-4}$

Therefore, the mass flow rate of air is also a limiting factor in the absorption process. If a sufficient mass flow of air is not provided, amount of CO_2 absorbed per sorbent and the space time yield of sorbent will decrease.

6.3. PEI-600 OR TEPA

Based on all the literature and data collected and analysed during this thesis, it was concluded that **TEPA had a better absorption performance than PEI-600.** This conclusion was based on the following points.

1. The average space time yield of Pure TEPA ($2e^{-4}$ $molCO_2/m^2s$) was found to be twice than that of PEI-600 ($1e^{-4}$ $molCO_2/m^2s$). This can also be seen in table 6.2.

2. The CO_2/amine ratio for TEPA (0.012) was found to be more than PEI-600 (0.01) for identical conditions and similar mass flow rate of sorbent of 0.08 ml/min ($1.33e^{-6}$ kg/s). This can be seen in table 6.1. Moreover, the residence time for pure TEPA was 17 minutes while PEI-600 had a residence time of 48 minutes on the same length of the channel.

3. Even theoretically, TEPA was found to have an advantage over PEI-600. Both TEPA and PEI-600 consist of primary and secondary amines, however, PEI-600 also has some tertiary amines. From section 2.4.1, it is known that tertiary amines can only react with CO_2 through the bicarbonate route. However, literature and experiments both indicate the absence of bicarbonates in lower CO_2 loading in amines. Therefore, some parts of PEI-600 can not contribute towards CO_2 capture, making TEPA the best choice. A FTIR analysis of a sample of loaded PEI-600 depicting an absence of bicarbonates is shown as an example to strengthen this claim in figure 6.17.

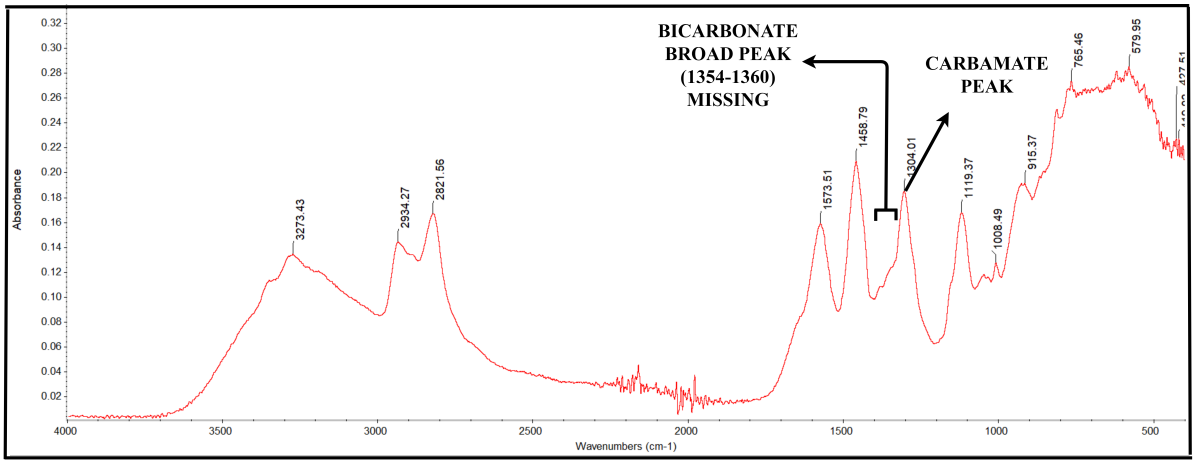

Figure 6.17: Absorbance vs wave number graph obtained by FTIR analysis on a loaded sample of PEI-600. The graph indicates an absence of a bicarbonate peak.

6.4. DESIGNING AN ABSORPTION COLUMN

6.4.1. BASIS OF DESIGN CHOICE

The design specifications for the absorption column were chosen based on the following inputs, parameters and constraints.

- According to ZEF's requirement, it was required to produce 825 grams of CO_2 in 8 hours through one absorption column.
- To maximize the surface area, another requirement was to have a parallel plate installation with channels on both sides.
- Due to area constraint, the top cross-section of the column had to have the dimensions of 0.25m*0.25m.
- The power requirement of fan was not to exceed 60W according to ZEF.
- To have a better accuracy of the model, it was necessary not to extrapolate the much model beyond the region of experimental data collection.
- Initial concentration of the sorbent was required to have 0.2 molCO_2/kg sorbent according to previous research by Ovaa[102].

6.4.2. ABSORPTION COLUMN DESIGN SPECIFICATIONS

Based on the constraints and inputs discussed in 6.4.1, the design specifications were made and can be seen schematically in figure 6.18.

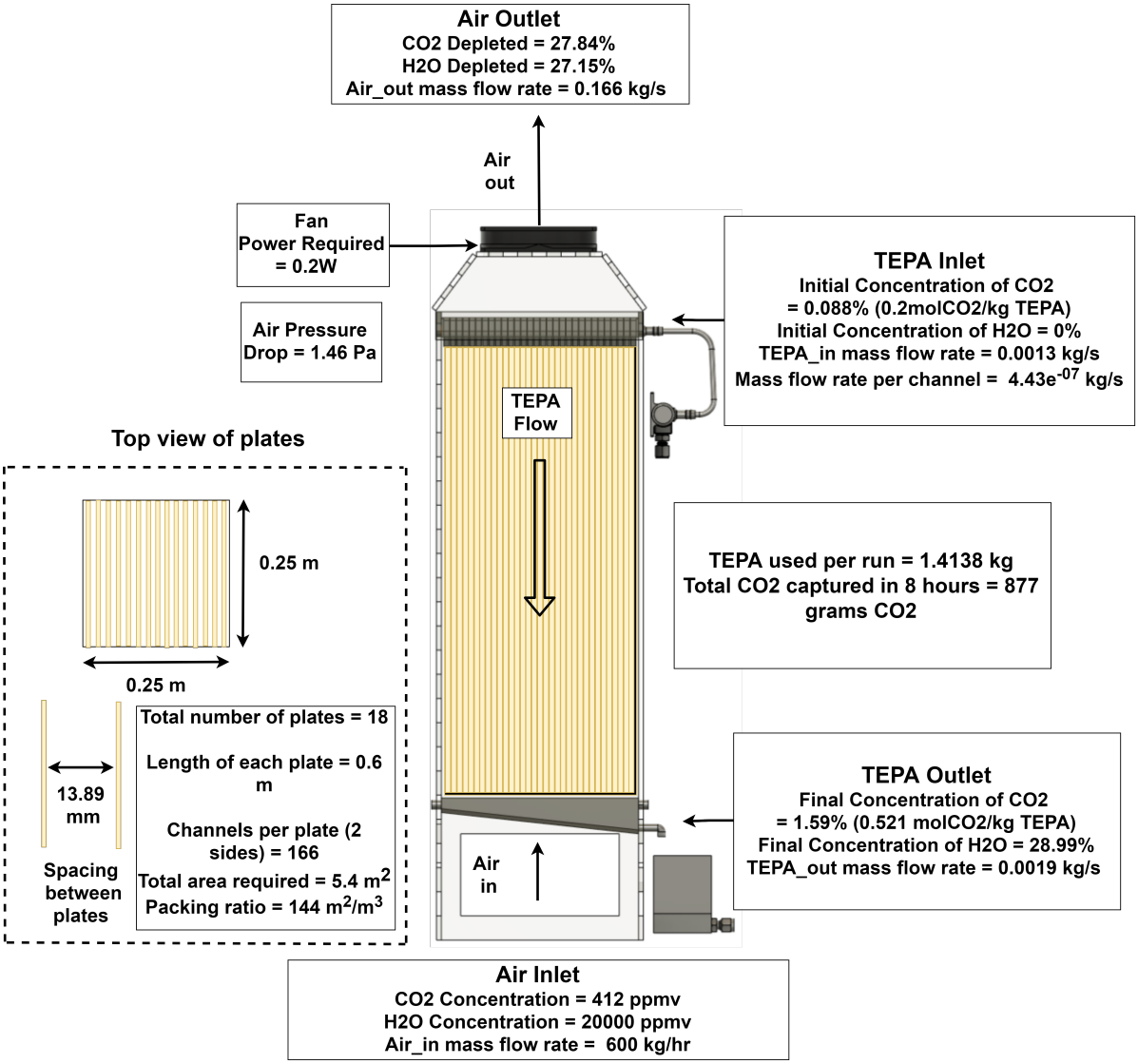

Figure 6.18: Design specifications for a direct air capture absorption column

Note: The power requirements for the fan was calculated through the pressure drop in air by using equation C.16. The efficiency of the fan was not taken into account. However small computer fans are be highly uneconomical and inefficient and the power requirement can easily be 5 times higher than 0.2 W. However, the power requirement for this design would still be much lesser than 60 W (power requirement constraint by ZEF).

6.4.3. DETAILED ANALYSIS OF PARAMETERS

Based on the design specifications, this section sheds light on the absorption process through the entire length of the column.

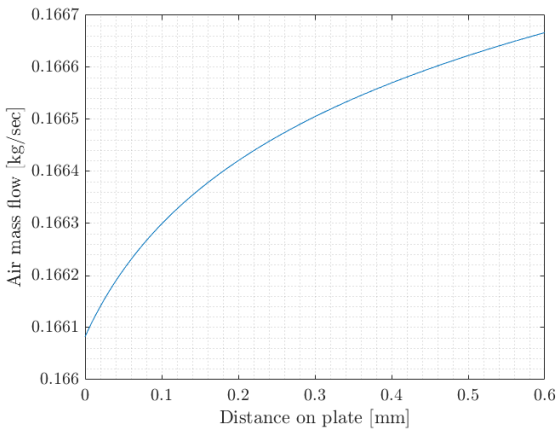

Figure 6.19: Total mass flow rate of air [kg/s] through 0.6 m column

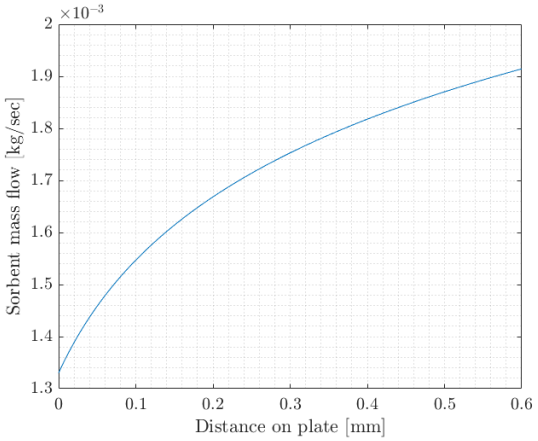

Figure 6.20: Total mass flow rate of sorbent [kg/s] through 0.6 m column

Figures 6.19 depicts a larger mass flow of air at the bottom of the absorption column and how it decreases as the air moves to the top of the column as CO_2 and H_2O are absorbed by the sorbent. Similarly, figure 6.20 depicts an increase in the mass flow of sorbent as the sorbent moves down the column due to absorption of CO_2 and H_2O.

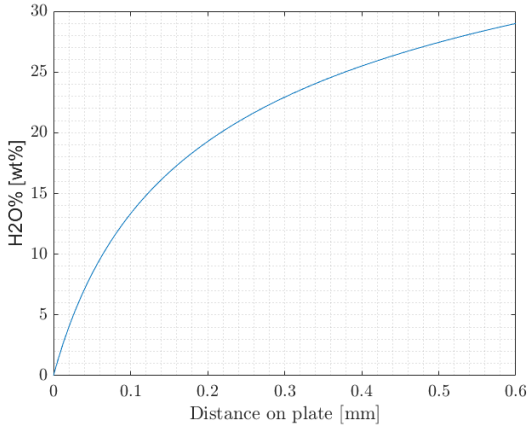

Figure 6.21: H_2O(weight %) absorbed through 0.6 m column

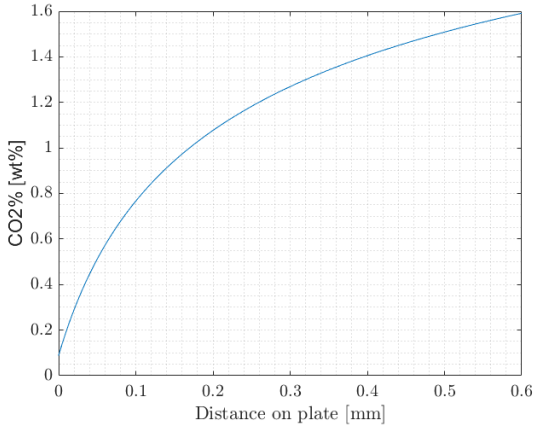

Figure 6.22: CO_2(weight %) absorbed through 0.6 m column

Figures 6.21 and 6.22 depict the increase in the concentration of H_2O and CO_2 in the sorbent as it flows down the absorption column.

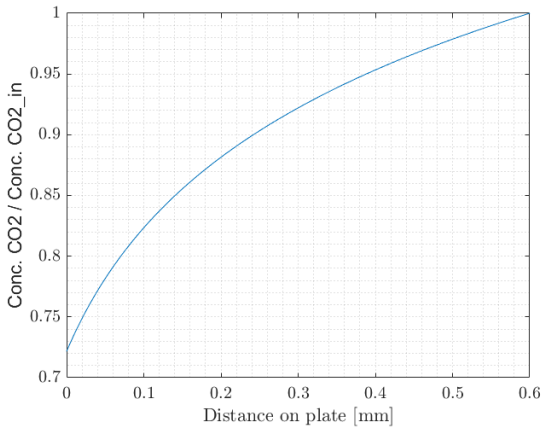

Figure 6.23: Depletion of H_2O through the 0.6 m column indicated by ratio of current to inlet concentration of H_2O

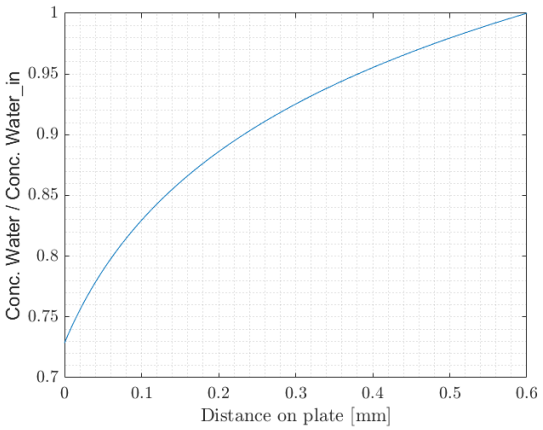

Figure 6.24: Depletion of CO_2 through the 0.6 m column indicated by ratio of current to inlet concentration of CO_2

Figures 6.23 and 6.24 depict the depletion of CO_2 and H_2O in the air as it flows from the bottom to the top of the absorption column.

7

RECOMMENDATIONS

Since thorough recommendations are necessary in order to lay the ground work for future research, this chapter lists the recommendations pertaining to direct air capture based on the work done and experience amassed during this thesis. Recommendations based on additional work done during the thesis with useful insights for future research are also listed in this chapter.

1. MIXING

The greatest insight form this thesis would be the importance of mixing the sorbent while it flows down the channel. The results show an increase in both CO_2 captured per amine used and the space time yield. Unfortunately, in this thesis only one mixing experiment was tried to make this point. **Therefore, future researchers should explore mixing more by trying to either use the same bridges or obstacles used in this thesis or coming up with different mixing strategies.** In addition, while performing mixing experiments, the following points should be investigated and kept in mind.

1. The aim should be to maximize both CO_2 captured per amine and the space time yield.

2. Since more CO_2 would be captured, the viscosity of the sorbent could be considerably higher as compared to what is found in this thesis. This could impact the bulk flow velocity of the sorbent (residence time) and diffusion rates of the sorbent.

3. If an efficient mixing method is found out, the absorption in the channel might behave differently than just a surface effect and it is possible that water could play a supportive role in absorption unlike what was found during a channel flow without mixing in this thesis.

2. SURFACE TENSION

This thesis ignores all effects of surface tension on the flow and the flow profile of the sorbent. The top layer of sorbent is considered flat with no meniscus. In reality, this is not true and should be investigated. Even a small meniscus would mean a greater surface area of the sorbent, thus decreasing the space time yield calculated in this thesis. The surface tension of the sorbent might change continuously with different concentrations of CO_2 and H_2O. Therefore, this should be studied in detail.

3. CHANNEL GEOMETRY

A rectangular geometery was used for the cross-section of the channel used in this thesis. However, if mixing is not included, the absorption is just a surface phenomena. Therefore, if the top surface area is kept constant while varying the geometry of the channel, the CO_2/amine ratio can be greatly increased.

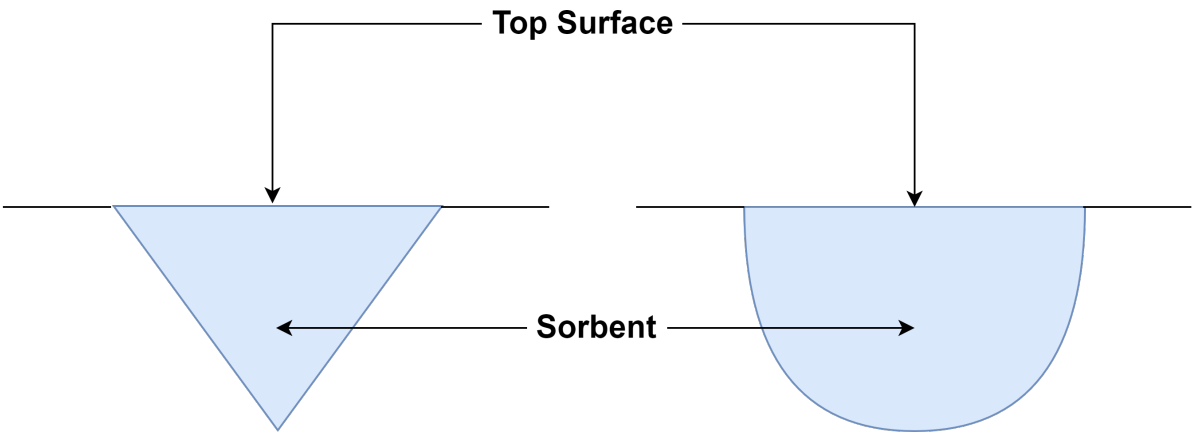

Figure 7.1: Alternative geometries suggested for the channel

Figure 7.1 shows a triangular and a circular cross-section that could be used instead of a rectangular cross-section in order to improve the CO_2/amine ratio. The top surface area would be same while the volume would be considerably lesser.

4. DIFFUSIVITY = FUNCTION (CO_2, H_2O)

The diffusivity for water in TEPA was estimated for different initial concentrations by extrapolating the H_2O data obtained during experiments to fit the equation 7.1.

$$y = A(1 - e^{\frac{-x}{T}}) \tag{7.1}$$

where

y	=	H_2O/amine (by weight)
A	=	maximum H_2O/amine possible (estimated value = 0.625)
x	=	time [s]
T	=	Time constant = L^2/D
D	=	diffusivity [m^2/s]
L	=	thickness of sorbent layer (estimated value = 0.8 mm)

The extrapolation of data can be seen in figure 7.2.

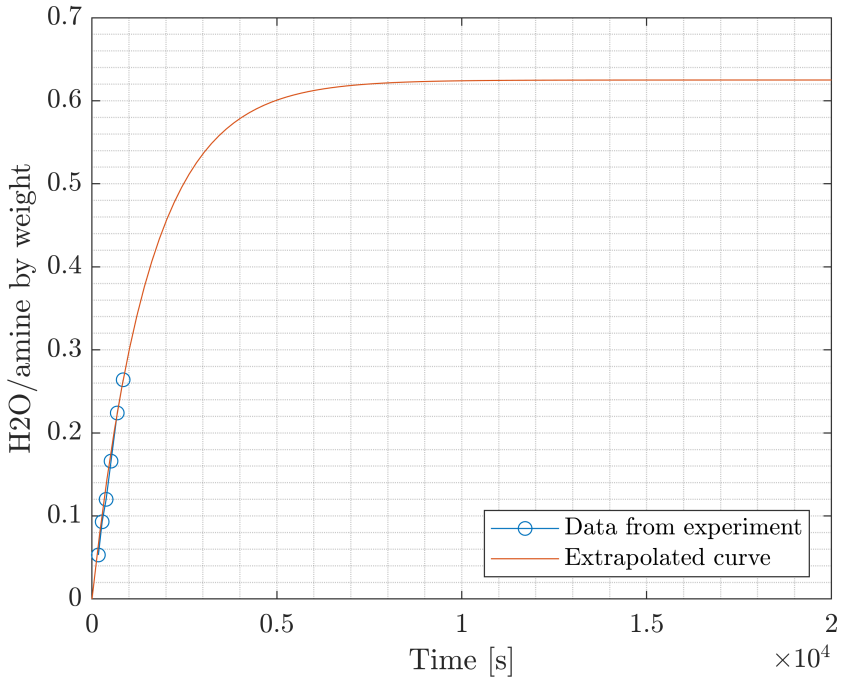

Figure 7.2: Data collected on $H2O$/amine for pure TEPA was extrapolated to fit a curve in order to estimate the diffusivity

Following the example shown above, the diffusivities of water for different initial concentrations of TEPA were estimated and can be seen in table 7.1. Since the theoretical maximum value of CO_2 was not known, extrapolation for CO_2 data was not done. **Note: This method is just used to estimate the diffusivity in order of magnitude to explain the diffusion process.**

Table 7.1: Estimated average diffusivities of water with different initial concentrations of TEPA

Initial concentration of TEPA	**Diffusivity of Water** $[m^2/s]$
0% CO2, 0% H2O	$4e^{-10}$
0% CO2, 10% H2O	$5e^{-10}$
0% CO2, 20% H2O	$1e^{-9}$
0% CO2, 30% H2O	$3e^{-9}$

Based on the data above the following points should be investigated or kept in mind.

1. Assuming an average diffusivity of H_2O or CO_2 for the entire absorption process would be a mistake.

2. The diffusivities of water seem to decrease with increasing initial concentration of water. **Therefore, it is possible that the initial concentration of sorbent in a non mixing regime would define the diffusivity function throughout the channel flow.**

3. This also indicates that the diffusivity of CO_2 and H_2O is complex and future research is necessary to invetigate diffusivity of CO_2 and H_2O in detail.

5. RELATIVE HUMIDITY AND TEMPERATURE VARIATIONS

This thesis conducts all experiments assuming a constant humidity and room temperature. Moving ahead in the research pertaining to absorption in direct air capture, a setup with controlled environment could be made to perform identical experiments. In addition, temperature and relative humidity should be varied to investigate how it affects absorption. Serrano Barthe[53] performed such experiments in a climate chamber for stationary sorbents on a flat plate. Similar experiments can be performed in a climate chamber with a channel flow.

6. MASS FLOW OF SORBENT VS CHANNEL DIMENSIONS

The mass flow of sorbent would greatly influence the channel dimensions. For lower mass flow rates, channels with lesser width would be suited better to maintain a uniform flow of sorbent.

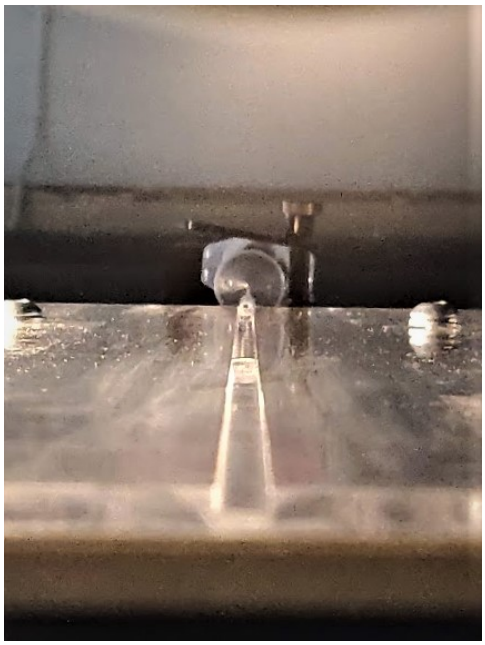

Figure 7.3: PEI-600 flowing uniformly over a 5mm wide channel with a 0.08 ml/min flow rate of sorbent

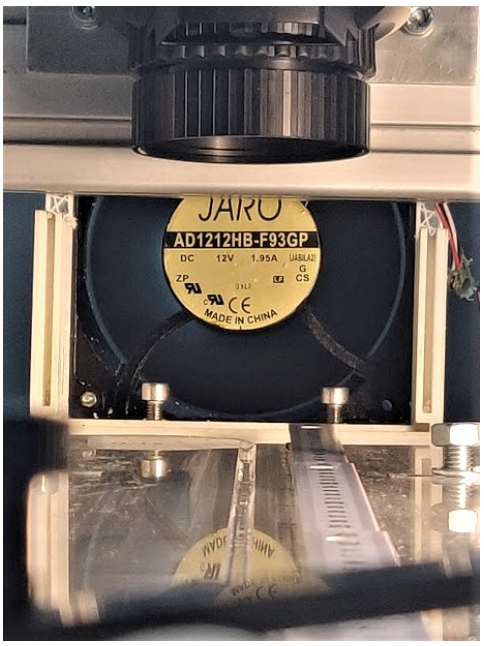

Figure 7.4: Non uniform flow of TEPA over a 5mm wide channel with a sorbent mass flow rate of 0.08 ml/min

Figures 7.3 and 7.4 show that with the same mass flow rate of sorbent, while PEI-600 flows uniformly over a 5 mm channel, TEPA sticks to the corner and flows in a non-uniform manner. For this reason a 3 mm wide channel was used to perform all TEPA experiments. Thus, this again points towards effects of surface tension and shows that the mass flow rate of sorbent would define the channel width being used. This could be countered by a circular or triangular cross-section shown in figure 7.1. While designing the absorption column, this should be kept in mind.

7. CRYSTALLIZATION OF TEPA

From 3.2.4, it can be seen that TEPA with 40% H_2O crystallizes at 11°C. Given the fact that TEPA is the chosen sorbent from this thesis and ZEF plans to install their microplants in deserts where it could get extremely cold at night, further research is required regarding the

causes and prevention of crystallization of TEPA. It is possible that at lower temperatures, TEPA might rystallize with even lower concentrations of water. This poses a threat to the sorbent distributors as they might get blocked due to TEPA's crystallization.

8. Limitations of absorption model and improvements

Every model has its limitations and so does the absorption model used to design the absorption column in this thesis. It is important that future researchers realize these limitations and improve them in order to achieve even better results. These limitations and suggestions for improvements are listed below:

1. The accuracy of the space time yield function for CO_2 and H_2O used in the model decreases if the channel length exceeds 0.6 m. This is due to the fact that the measurements and experiments were done only on a 0.6 mm channel. This can be improved by using longer channels in experiments.

2. The model assumes a fixed concentration of CO_2 and H_2O in ambient air at all times. A variable concentration system can be developed and included in the model to match the reality.

3. If a sorbent mixing method is developed, a new space time yield function corresponding to the new system should be added in the model.

4. Since more CO_2 is expected to be absorbed if sorbent mixing method is included, viscosity of the sorbent might become an important factor and thus, the flow rate of the sorbent might be influenced. Therefore, viscosity variations at each element should be included in the model and correlated with the flow speed of the sorbent.

5. Instead of every 100 mm section on the channel, measurements for CO_2 and H_2O concentrations can be done for every 50 mm or less. Although, it adds labor to the experiments, the data obtained would be more accurate and better space time yield functions can be obtained.

6. The power required to pump the sorbent from the desorber to the absorption column was not included in the model developed for this thesis. Therefore, it should be taken into account for the second version of this model to estimate the total power requirements of the direct air capture system.

9. Degradation of amines

The amines used around the world in a solid sorbent system (2.1.2) are known to degrade by the influence of oxygen, sulphur, high temperatures etc. In addition, formation of urea is also observed in commonly used amine. Keeping this in mind, degradation of amines should be investigated in detail. An FTIR or NMR (Nuclear Magnetic Resonance Spectroscopy) analysis can be helpful in analysing degradation. Moreover, since ZEF wants to install their micro-plants in the desert, dust or sand becomes a major influencing factor in the absorption process. Therefore, once a functional prototype of the direct air capture unit is built, dust filters should be installed. This could also influence the pressure drop of the fan and the air flow. To conclude, this area still requires future research.

10. LIFE CYCLE ANALYSIS

All experiments performed in this thesis were performed once without a life cycle analysis. The behaviour of the rich and lean amine should be studied by continuously absorbing and desorbing amines to investigate if the absorption or desorption performance is affected by this continous operation.

11. VISCOSITY MODEL

Two main points regarding the viscosity model developed in this thesis should be kept in mind.

1. Viscosity was modelled through multiple regression and is not a physically correct model. Therefore, using the model to calculate viscosity of sorbents of concentrations beyond the model's domain is not recommended.

2. The viscosity model can be made more accurate if more data points can be collected in the 0-2 % range of CO_2 weight concentrations. Since it was observed in this thesis that the CO_2 concentration in the absorption process was within the range mentioned above, higher accuracy can be achieved in that region.

12. AVERAGE VISCOSITY VS TOP LAYER VISCOSITY

The work done during this thesis only calculates the average viscosity of the sorbent. However, since the absorption of CO_2 and H_2O is a surface phenomena, the viscosity of the top layer of the sorbent is expected to be significantly higher than the average viscosity. Therefore, an average viscosity would not be a good representation of the absorption process and new methods should be investigated to estimate the viscosity of the top layer. Figures 7.5-7.8 show that the average viscosity makes it difficult to infer results.

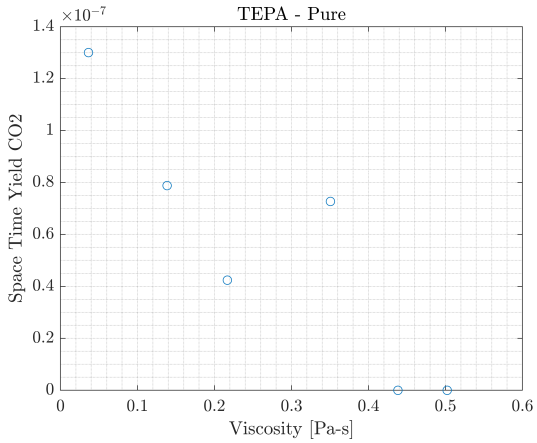

Figure 7.5: Space time yield of CO_2 vs viscosity while using Pure TEPA as sorbent

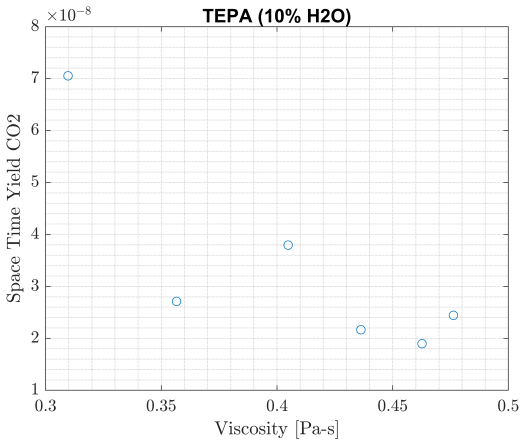

Figure 7.6: Space time yield of CO_2 vs viscosity while using TEPA (10% H_2O, 0% CO_2) as sorbent

It might be inferred by figures 7.5 and 7.6 that the space time yield of CO_2 decreases as the average viscosity increases. However, this analysis is incomplete without considering the data from the figures below.

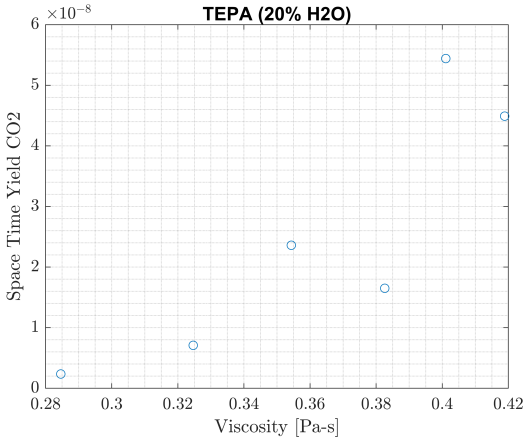

Figure 7.7: Space time yield of CO_2 vs viscosity while using TEPA (20% H_2O, 0% CO_2) as sorbent

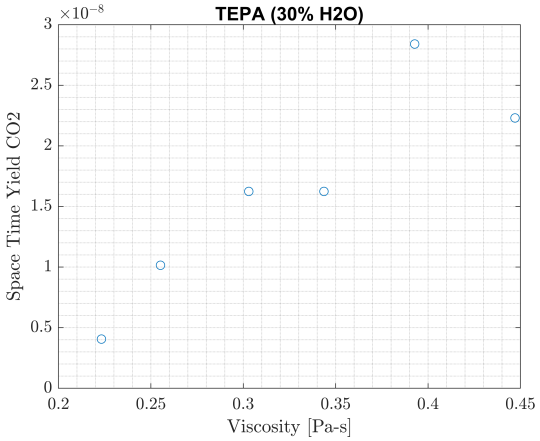

Figure 7.8: Space time yield of CO_2 vs viscosity while using TEPA (30% H_2O, 0% CO_2) as sorbent

Figures 7.7 and 7.8 show a different result. The space time yield of CO_2 seems to increase with increasing average viscosity.
A close analysis on the 4 graphs above would reveal that the space time yield of CO_2 is actually being influenced by the position on the channel, rather than the average viscosity. In figures 7.5 and 7.6, the average viscosity is increasing as the sorbent flows down the channel whereas in figures 7.7 and 7.8, the average viscosity is decreasing as the sorbent flows down the channel. Therefore, the position on the channel is defining the space time yield of CO_2 and not the average viscosity. Having said that, if the viscosity of the top layer could be calculated, that would probably give a better correlation with the space time yield of CO_2. Therefore, the top layer viscosity should be found out.

13. Molecular Simulations

The research at ZEF pertaining to direct air capture has progressed to a stage well beyond proof of concept. Having said that, PEI-600 and TEPA haven't been studied from a chemical standpoint. Therefore, it is time to investigate these amines through molecular simulations in order to find the following and more.

1. The theoretical maximum value of concentrations of CO_2 and H_2O that could be absorbed in PEI-600 and TEPA.

2. Studying the behaviour of hydrogen bridge breakdown and formation in order to explain the maximum viscosity and viscosity trend with water.

3. Simulation on blends of different amines in order to study the performance of blends with respect to absorption and desorption.

4. Studying the effects of steric hindrance and how it could be used in order to improve absorption.

14. Heat of Absorption and Thermal properties

The values for heat of absorption for water calculated during thesis were done through collecting data with a thermal camera assuming all the thermal properties of the sorbent. The thermal properties of bulk PEI-600 and TEPA such as heat capacity should be found

out. Moreover, a calorimeter would give more accurate results for the heat of absorption of water and CO_2 and their dependence on loading and temperature. This data would be useful to calculate the energy costs during regeneration of amines.

15. ISLANDS/ HOT SPOTS

While collecting thermal images of the sorbent flow, hot spots on the sorbent were observed. Figures 7.9-7.12 show the thermal images with these islands or hot spots on PEI-600 and TEPA.

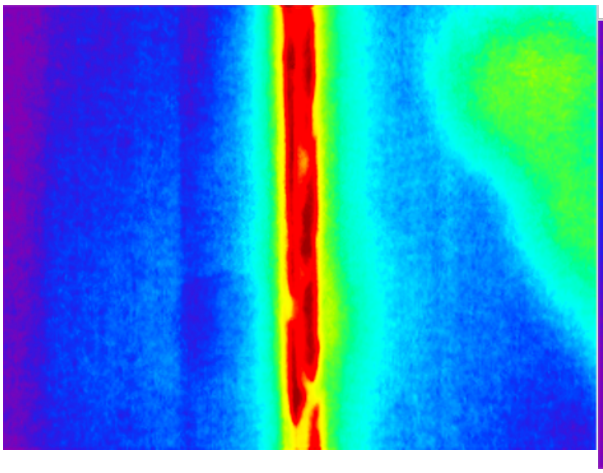

Figure 7.9: Depiction of the starting phase of hot spot formation where the uniformly heated sorbent slowly develops hot spots.

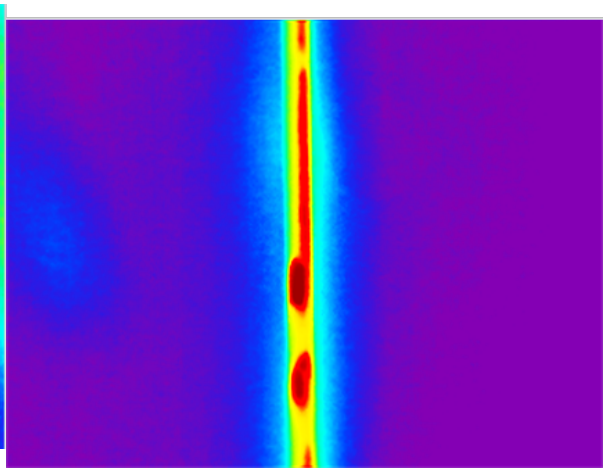

Figure 7.10: Depiction of the hot spots leaving a hot trail while flowing downwards.

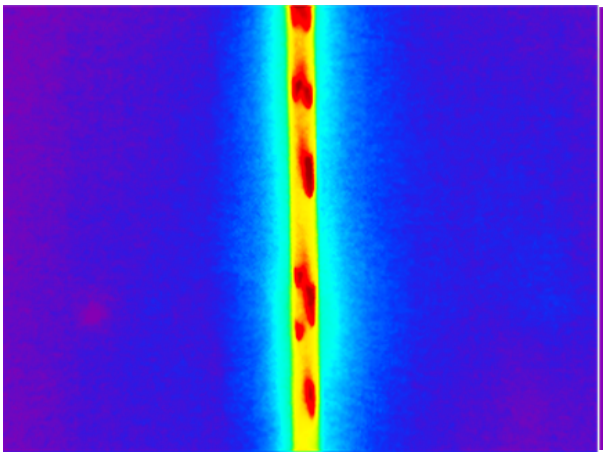

Figure 7.11: Depiction of two or more hot spots clubbed together while flowing down the channel.

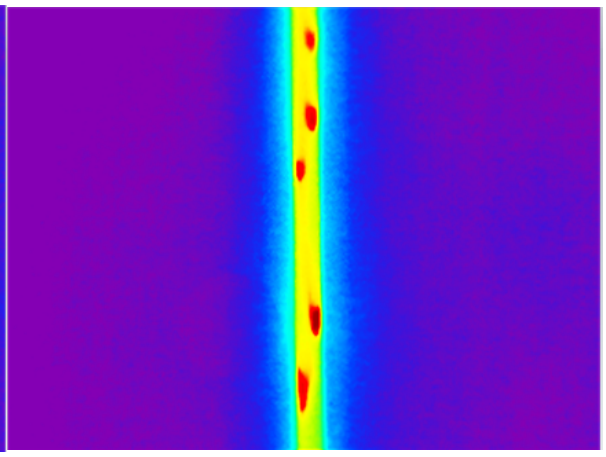

Figure 7.12: Individual hot spots flowing down the channel.

This thesis was unable to explain these effects and further research is required to investigate these hot spots. In addition, the following observations and questions should be kept in mind.

1. These hot spots were always observed towards the bottom part of the channel.

2. Since the sorbent is heated up due to absorption of CO_2 and H_2O, it is possible that the concentration of CO_2 and H_2O is higher in these hot spots. If true, this could mean that we are not utilizing the entire surface of the sorbent for absorption.

3. Induced mixing might help to have a homogeneous surface absorption. Experiments should be performed with a thermal imaging camera with induced mixing to observe the effect on these hot spots.

4. Average concentrations of CO_2 and H_2O are not a good representation of these hot spots and therefore, a method to investigate these concentrations at several points should be found out.

An idea of a setup to better understand these hot spots is described below in figure 7.13. This setup was discarded during this thesis due to its complexity and time constraints. However, such a setup would provide more data and a better representation of the absorption process if it works.

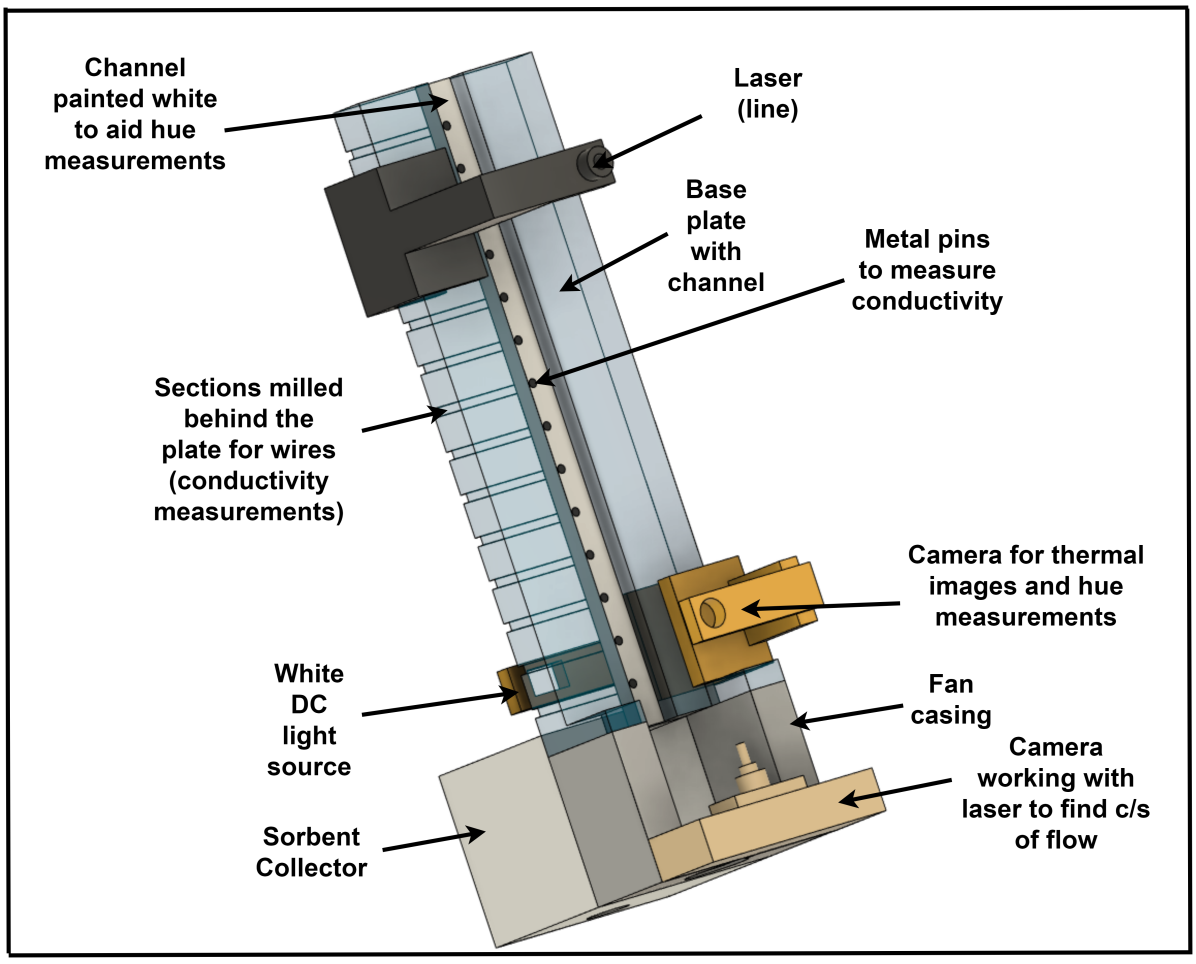

Figure 7.13: Setup proposed to achieve a detailed information about absorption process

Figure 7.13 shows a proposed setup to analyse the absorption process. Based on some experiments done out of sheer curiosity during this thesis, it was found out that the pH and conductivity of the sorbent also varies with varying concentrations of CO_2 and H_2O.

Therefore, this setup could be calibrated with both pH and conductivity measurements. Appendix C.1 and C.2 contain data on the pH and conductivity measurements performed with details of various dyes that can be used in this setup. Using pH dyes, hue measurements can be done to estimate the pH at different points on the channel while metal pins code could be used to measure conductivity. A thermal camera could be used to observe the flow and a line laser with a camera towards the end of the channel could be used to estimate the flow cross-section which would be insightful in estimating the layer thickness and even the meniscus of the flow at different points on the channel. Finally, average concentrations could also be calculated from the FTIR calibration done in this thesis. Therefore, although building such a setup is complex, all these data together in real time while the sorbent is flowing down the channel could provide information well beyond what is presented in this thesis. This could be able to explain the effects of hot spots and would give many insights into the absorption process.

16. ANALYSIS OF SPACE TIME YIELD TRENDS OF CO_2 AND H_2O

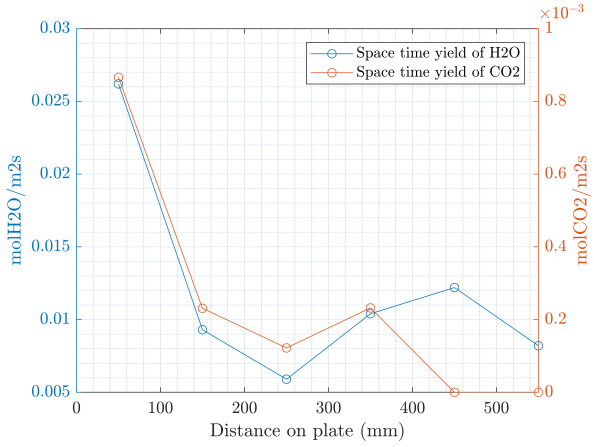

Figure 7.14: Comparison of Space time yields of CO_2 and H_2O for Pure TEPA as a sorbent at every 100 mm on channel

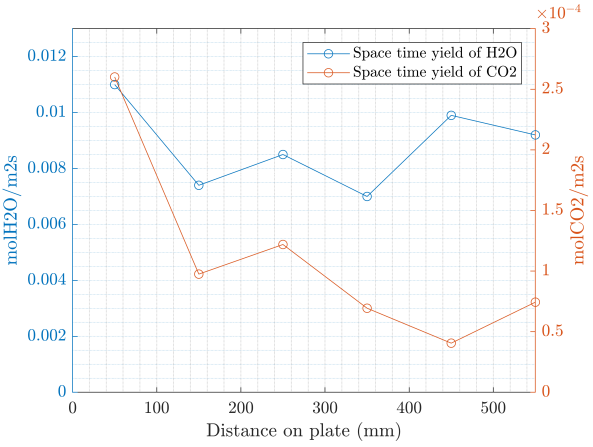

Figure 7.15: Comparison of Space time yields of CO_2 and H_2O for TEPA (0% CO_2, 10% H_2O) as a sorbent at every 100 mm on channel

Figures 7.14 and 7.15 show the comparison of the space time yields of CO_2 and H_2O for pure TEPA and TEPA (0% CO_2, 10% H_2O). Based on these curves, the following points are open to research.

1. It is seen from the two figures that the space time yields of CO_2 and H_2O seem to be directly correlated at least in the top section of the channel. Other initial concentrations of sorbents also yield similar results. It is indicated that space time yield of CO_2 increases and decreases with corresponding increase and decrease in space time yield of H_2O. This points towards the role of water in the CO_2 absorption process. Although this thesis does not draw any conclusions based on this, it might be worthwhile to investigate.

2. The space time yields in the bottom part of the channel do not seem to be correlated. This should also be investigated.

3. While bubbling pure CO_2 through PEI-600 (0% CO_2, 0% H_2O), the CO_2 capture was the lowest and almost negligible as compared to other concentrations of PEI-600. This was seen in figure 3.19. Even if the physical solubility of CO_2 in pure PEI-600 is considered negligible, the surface of the sorbent was still exposed to the pure CO_2 gas. The only difference in that experiment and one one performed on the channels was the absence of H_2O in air in the CO_2 bubbling experiment. This seems to strengthen the possibility that concentration of H_2O in air aids in CO_2 capture in amines. **This should be investigated further. An experiment in a climate chamber can be performed with different relative humidity of air and space time yields of CO_2 and H_2O can be compared.**

A

MEASUREMENT EQUIPMENT

The details of the various measurements instruments and techniques performed in this thesis are presented in this chapter of appendix.

A.1. COULOMETRIC KARL FISCHER TITRATOR

This section discusses the basic working principle of the Karl Fischer Titrator and lists all the data collected from the equipment.

A.1.1. BASIC WORKING PRINCIPLE

There are two types of Karl Fischer titrators - volumetric and coulometric. The distiction between the two is shown in figure A.1.

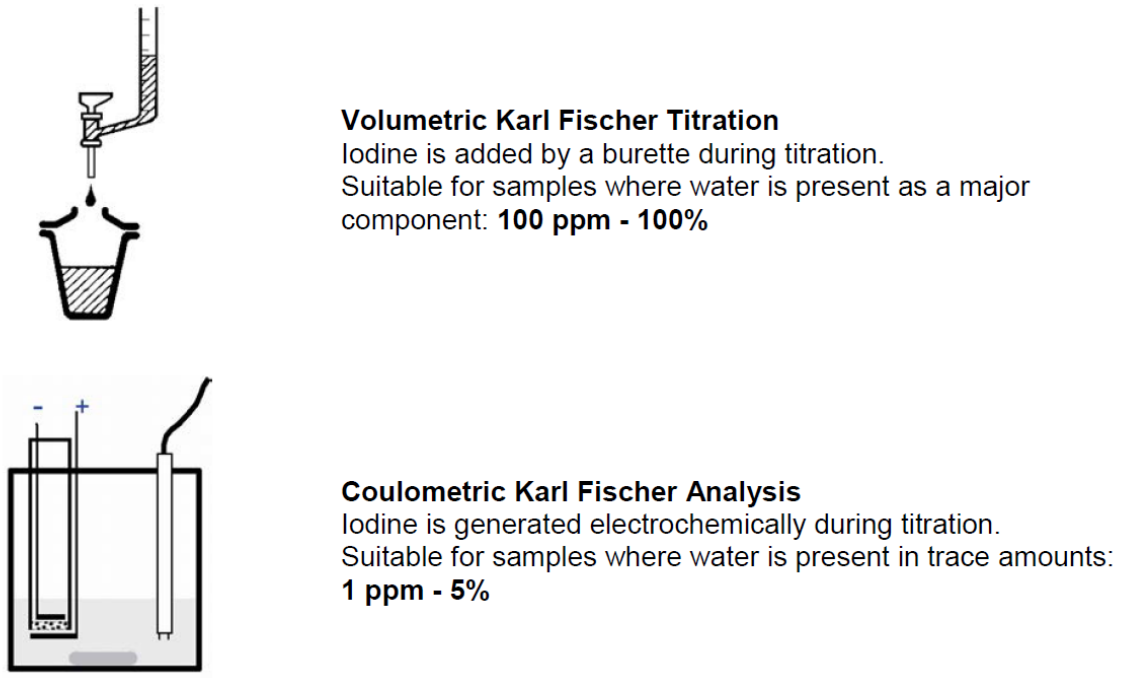

Figure A.1: Volumteric vs Coulometric Karl Fischer analysis [21]

A coulometeric Karl Fischer was used in this thesis because low concentrations of water were being measured after the test sample was diluted with methanol. The titrator consists of a generator and a detector electrode. The generator electrode generates iodine and its job is to maintain a certain concentration of iodine in the titration solution. The equation pertaining to iodine generation can be seen below.

$$2I^- \longrightarrow I_2 + 2e^- \tag{A.1}$$

When a test sample containing water is added to the solution, I_2 reacts with H_2O in a 1:1 ratio. This depletion of iodine is constantly replenished by the generator electrode. According to Faraday's law, the quantity of iodine produced should be proportional to electric load. Since iodine and water react in a 1:1 ratio, the consumption of iodine is calibrated such that $1\mu g H_2O = 10.712$ mC. Therefore, the titration runs until all of the water reacts with the iodine being generated by the generator electrode. When the water is depleted in the the solution, the detector electrode detects excess iodine and the titration is stopped. The total water concentration is found through the total electric load from the quantity of iodine produced [103].
Note: The sample being tested would yield best results if the pH of the sample is between 5.5 and 8. Therefore, amine solutions mixed with methanol are preferred due to the lower pH and lesser absolute water concentration which makes the titration faster.

WATER CONTENT IN METHANOL

Since the amine samples were mixed with methanol, the water concentration in methanol was found out and the measurement values were corrected. The table A.1 below shows the measured concentration of water in methanol.

Table A.1: Water concentration in Methanol used

H2O% in Methanol	
1st measurement	0.067
2nd measurement	0.063
3rd measurement	0.058

A.1.2. DATA OBTAINED FROM KARL FISCHER TITRATOR

The data obtained during this thesis for various samples of PEI-600 and TEPA are tabulated in tables A.2 and A.3. Only the final results are shown here and not the calculations performed to reach to these results. Each measurement was done twice to have a high quality data set.

Table A.2: Water concentration data of PEI-600 samples from Karl Fischer

H2O% (weight)- Karl Fischer Measurement		
Sample code	**1st measurement**	**2nd measurement**
5-final	16.88	16.85
5-final-duplo	17.68	17.71
2-final	20.12	19.77
3-final	10.90	11
P-20.21-2.41	21.68	21.84
Pure PEI(big font)	1.72	1.69
P-10.06-4.1	11.05	11.16
Pure PE Duplo	1.94	1.84
P-10.23-2.6	11.19	11.3
P-20.06-4.1	20.16	20.15
1-final	13.15	12.47
P-29.911-1.5375	29.53	29.9
P-29.6-3	28.77	28.5
BM-P-10W	10.56	11.8
BM-P-30W	29.79	29.1
BM-P-20W	21.08	20.84
BM-P-40W	38.84	39.2
P-10W (mota)	11.29	11.6
P-20W (mota)	20.30	20.51
P-30W(mota)	31.42	31.69
P-30-0Co2	27.39	27.077
P-40W(mota)	39.72	39.34
BM-P-40W	38.21	37.92
P-30.5-5.63	29.55	29.4
P-50W	45.95	45.62
BM-P-50W	49.62	46.84
P-70W	67.47	68.28
BM-P-70W	64.44	65.7

Table A.3: Water concentration data of TEPA samples from Karl Fischer

H2O% (weight)- Karl Fischer Measurement		
Sample code	**1st measurement**	**2nd measurement**
4-final	24.21	24.17
T-10w(MOTA)	13.79	13.66
BM-T-20W	19.90	19.68
BM-T-Pure	1.37	1.45
BM-T-10W	9.11	9.21
T-20W(mota)	21.08	21.4
T-pure(mota)	1.15	1.3
T-20.195-2.46	24.29	23.95
T-30-1.56	30.01	31.11
T-10.25-3.2	10.58	11.01
T-15.55-5.17	16.31	16.05
T-30-4	30.76	30.45
T-10.32-2.32	11.13	11.25
T-20.25-3.2	20.61	21.1
T-30-9.43	29.55	29.3
T-30W(main sample)	29.96	30.05
T-30-5.725	29.53	29.44
T-50W(doubt)	30.57	29.67
BM-T-50W	28.33	29.1
P-50W	45.95	45.62
T-50W(duplo)	29.49	29.63
T-70W	68.42	67.84
BM-T-70W	62.84	61.36
T-60W	64.75	66.94

A.2. PHOSPHORIC ACID TEST

This section discusses the basic working principle of the phosphoric acid test setup and subsequently tabulates all data obtained from the setup during this thesis.

A.2.1. BASIC WORKING PRINCIPLE

Figure A.2 shows the schematics of a phosphoric acid test setup.

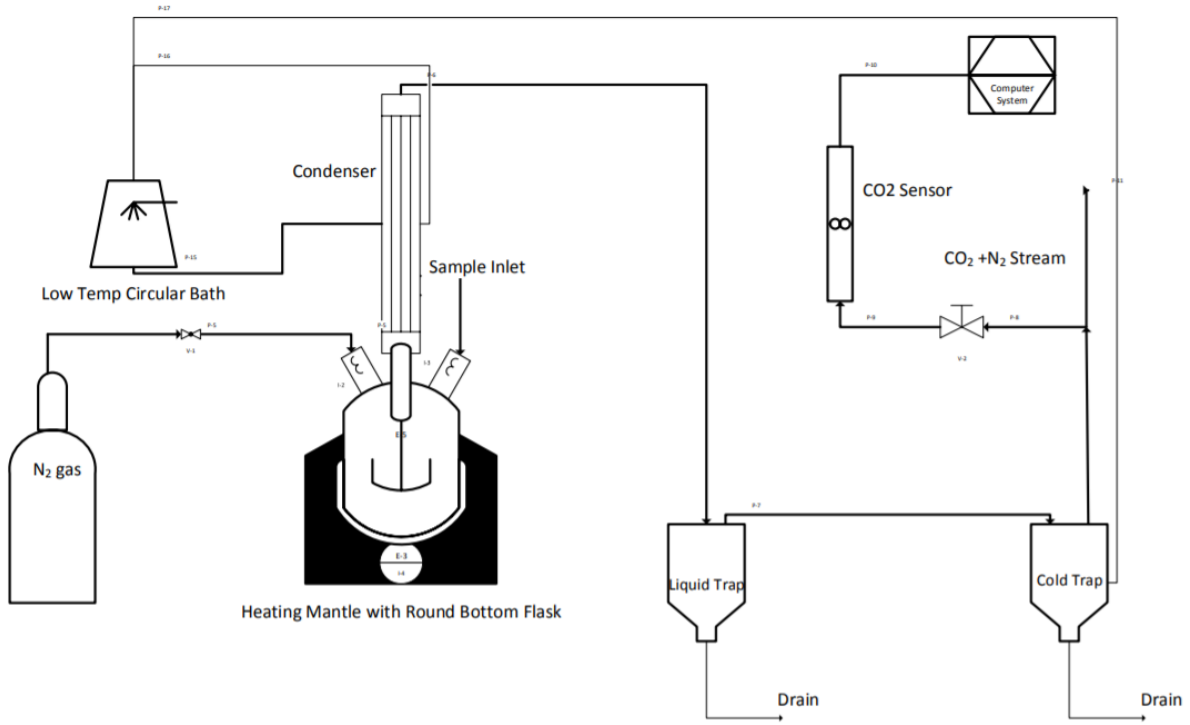

Figure A.2: Schematic of a phosphoric acid setup [22]

The round bottom flask contains about 350 ml of 85% phosphoric acid. With a constant temperature of the heating mantle at about 240°C, the phosphoric acid in the round bottom flask can be maintained at around 150°C which provides sufficient heat to desorb the amines containing CO_2. Small sample of loaded amine can be inserted in the round bottom flask leading to desorption of CO_2 due to esterification between the amine and hot phosphoric acid. The resultant gases desorbed flow through a condensor which is kept at around 8°C to condense water vapours before the gas stream enters the CO_2 analyzer. A nitrogen tank is used to dilute these gases and constantly flows through the round bottom flask to the CO_2 analyzer. The CO_2 gas carried by nitrogen enters the CO_2 analyzer which records voltage changes and calibrates it to CO_2 partial pressure. Through the partial pressure of CO_2, the mass flow rate of CO_2 is calculated and a total amount of CO_2 is displayed on the user interface on the computer [22].

A.2.2. DATA OBTAINED FROM PHOSPHORIC ACID TESTS

The data obtained from the phosphoric acid setup for various samples of PEI-600 and TEPA is tabulated in tables A.4 and A.5. Only the final results are tabulated and not the entire calculation. Each measurement was done twice to achieve a high quality data set.

Table A.4: CO_2 concentration data of PEI-600 samples from Phosphoric acid tests

CO2% (weight)- Phosphoric acid test measurements		
Sample code	**1st measurement**	**2nd measurement**
5-final	0.53	0.55
2-final	0.65	0.63
3-final	0.48	0.47
P-20.21-2.41	2.64	2.58
Pure PEI(big font)	0.10	0.12
P-10.06-4.1	4.90	4.85
P-10.23-2.6	3.04	3.11
P-20.06-4.1	4.64	4.57
1-final	0.43	0.46
P-29.911-1.5375	1.67	1.72
P-29.6-3	3.15	3.19
BM-P-10W	0.15	0.19
BM-P-30W	0.45	0.5
BM-P-20W	0.46	0.46
BM-P-40W	7.12	7.31
P-10W (mota)	0.02	0.02
P-20W (mota)	0.02	0.02
P-30W(mota)	0.02	0.03
P-30-0Co2	1.45	1.37
P-40W(mota)	0.02	0.02
BM-P-40W	0.03	0.02
P-30.5-5.63	7.37	7.48
P-50W	0.01	0.03
BM-P-50W	2.50	2.32
P-70W	0.06	0.08
BM-P-70W	6.13	6.34

Table A.5: CO_2 concentration data of TEPA samples from Phosphoric acid tests

CO2% (weight)- Phosphoric acid test measurements		
Sample code	**1st measurement**	**2nd measurement**
4-final	0.60	0.59
T-10w(MOTA)	0.02	0.02
BM-T-20W	4.75	4.66
BM-T-Pure	0.28	0.31
BM-T-10W	6.11	6.32
T-20W(mota)	0.01	0.02
T-pure(mota)	0.03	0.02
T-20.195-2.46	2.75	2.66
T-30-1.56	1.77	1.61
T-10.25-3.2	4.08	4.21
T-15.55-5.17	6.64	6.51
T-30-4	3.60	3.57
T-10.32-2.32	2.47	2.63
T-20.25-3.2	3.88	4.01
T-30-9.43	11.72	11.48
T-30W(main sample)	0.03	0.03
T-30-5.725	6.70	6.56
T-50W(doubt)	0.02	0.01
BM-T-50W	5.78	5.6
T-50W(duplo)	0.03	0.04
T-70W	0.03	0.02
BM-T-70W	8.82	8.64
T-60W	0.02	0.02

A.3. FOURIER-TRANSFORM INFRARED SPECTROSCOPY

The vibrational spectrum of any molecule can be considered as a unique physical property which would be characteristic of the molecule [104]. The atoms of every molecule are always vibrating. Infrared spectroscopy is the study of interaction of light with matter [105]. When a molecule absorbs infrared radiation, its chemical bonds vibrate. The bonds can stretch, contract, wag and bend. This is why infrared spectroscopy is a type of vibrational spectroscopy [104].The measurements obtained in infrared spectroscopy gives an infrared spectrum, which is a plot of measured infrared intensity versus wavelength (or wavenumber) of light [105].Solids, Liquids, gases, semi-solids, powders and even polymers can be analysed by identifying the positions of their peaks, intensities, width and shapes of the plot obtained by infrared spectroscopy [104][105]. Fourier transform infrared spectroscopy (FTIR) is an analytical technique used to identify organic (and in some cases inorganic) materials.

A.3.1. WORKING PRINCIPLE

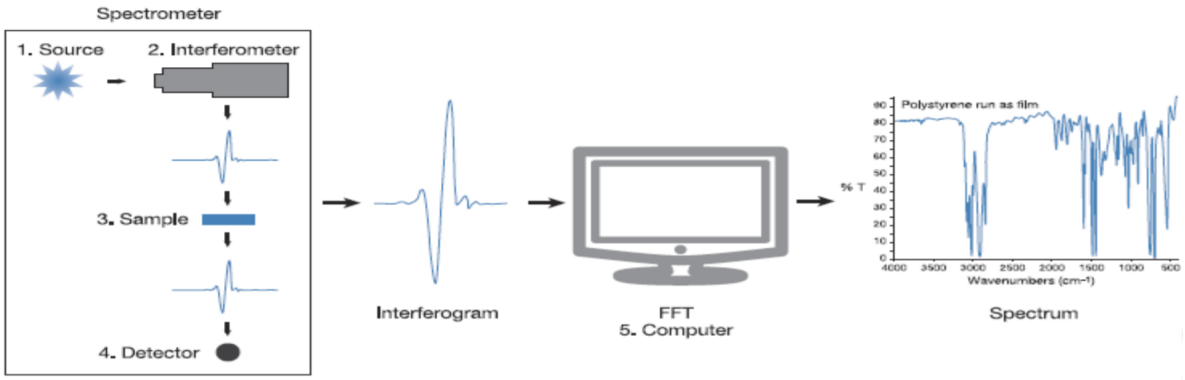

Figure A.3: Depiction of working principle of FTIR [23]

Figure A.3 depicts the working principle of FTIR. The general components of a Fourier Transform Infrared Spectrometer include a source, an interferometer, a sample compartment, a detector and a computer. The source would emit infrared energy. This beam would pass through an aperture which would control the amount of energy being provided to the sample, and ultimately to the detector. The beam enters the interferometer in which the interference of two beams of light would be employed to make precise measurements. The resulting interferogram signal would exit the interferometer and enter the sample compartment. This is where specific frequencies of energy which are uniquely characteristic of the sample are absorbed. The beam passes into the detector for final measurement and the measured signal is digitized and sent to the computer where the Fourier transform takes place. The final infrared spectrum is showed on the computer for further analysis [106][23].

A.3.2. WORKING WITH OMNIC

When the FTIR machine is ready to use, the following steps are conducted to obtain an absorption spectrum.

STEP 1

Install and open the OMNIC software required to analyse the FTIR data. Figure A.4 shows the OMNIC interface.

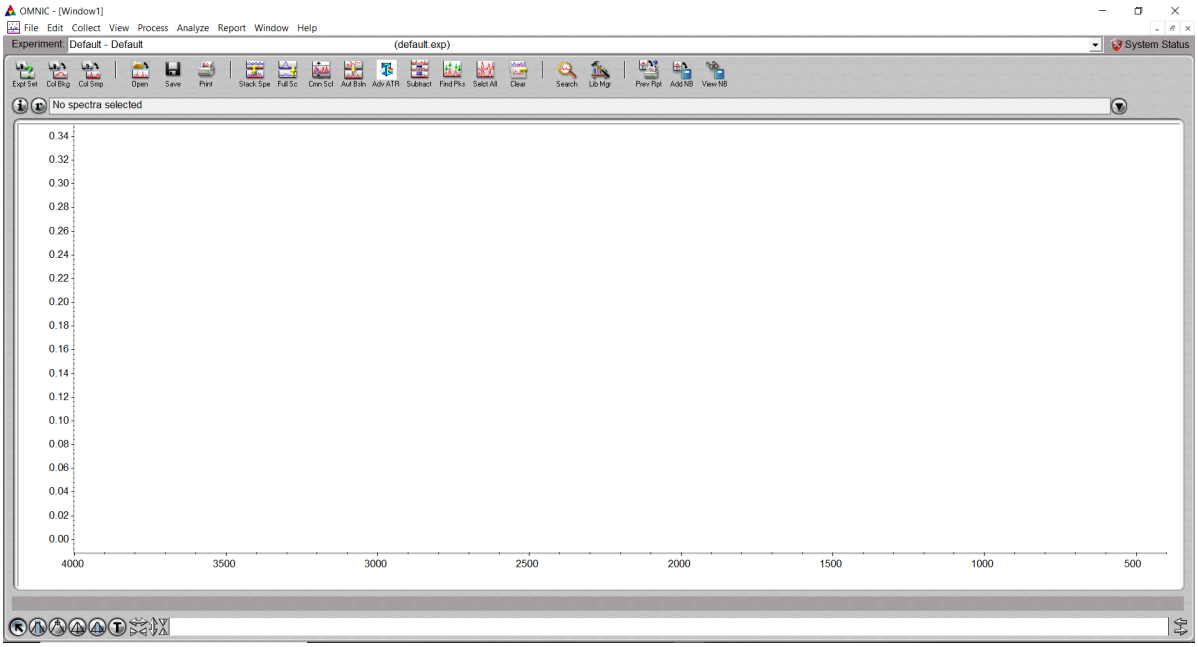

Figure A.4: OMNIC software interface

STEP 2

The second step would be to collect a background spectrum without any sample. The sample collection area is first cleaned and a background spectrum is collected from the "Collect" tab in the top tool bar. An example of a background spectrum can be seen in figure A.5.

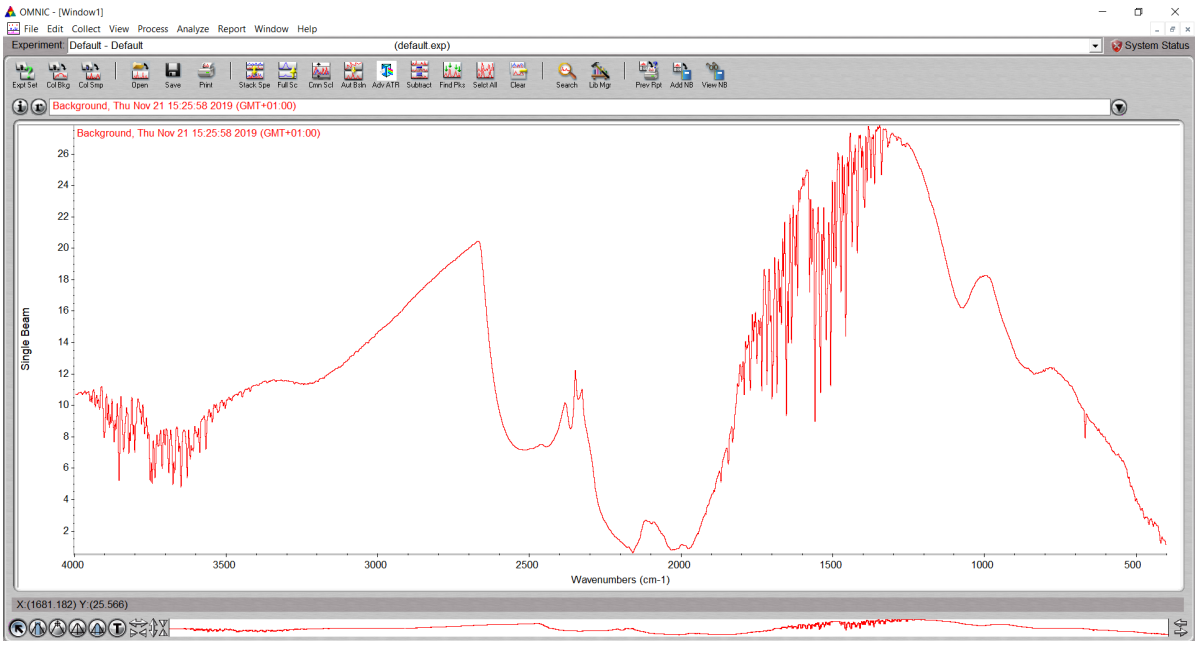

Figure A.5: An example of a background spectrum collected

STEP 3

Now, the sample to be analysed can be placed on the data collection area and analysed through the "Collect Sample" button in the "Collect" tab. The FTIR would take multiple

scans and present an average spectrum on the interface. An example can be seen in figure A.6.

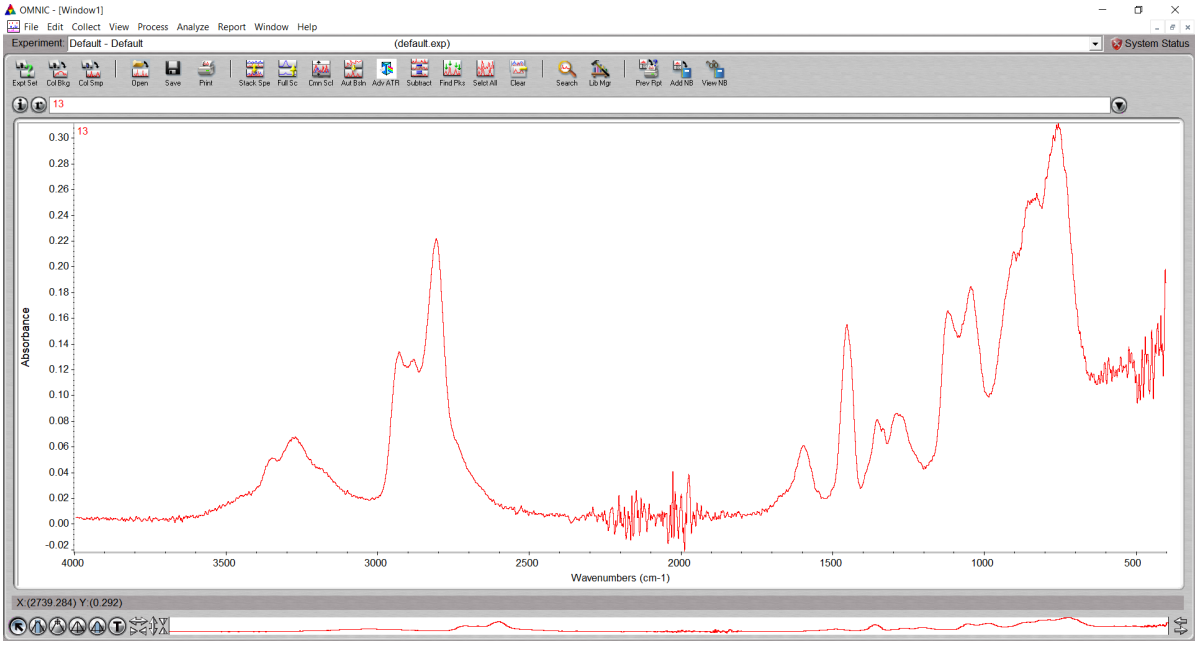

Figure A.6: An example of a spectrum collected by analysing a sample of TEPA

Once such a spectrum is obtained, it can be analysed by the researcher using other tools in this software. The applications of these other tools are vast and not included in this appendix.

A.3.3. IDENTIFICATION OF PEAKS

Table A.6 shows the general peak values in amines according to literature. Generally, the peaks can shift slightly to the left of right. However, this table gives useful information in order to identify peaks with PEI-600 and TEPA in order to qualitatively and quantitatively analyse the sorbent samples.

Table A.6: General peaks in amines

Peaks for amines			
Group	**Type**	**Wavenumber(cm-1)**	**Reference**
N-H wag	primary and secondary amines	910-665	[107]1,[53]
C-N strech	aliphatic amines	1250-1020	[107]1,[53]
C-H bend	alkyl group	1480-1350	[108],[53]
N-H bend	primary amines	1650-1580	[107]1,[53]
C-H stretch	alkyl group	3000-2850	[108],[53],[109]
N-H stretch	primary amines	two bands from 3400-3300 & 3330-3250	[107]1,[53]
N-H stretch	secondary amines	3350-3310	[107]1,[53]
N-H stretch	tertiary amines	no bands	[107]
Water in amines (MEA)			
O-H (broad)	water	3355, 3293	[109]
Amine/CO2/H2O system			
Bicarbonate	amine/CO2/water system	broad peak in 1360-1354	[110]
CO2 loaded MEA			
secondary amine		1564	[109]
experimental observations		1464	[109]
carbonate		1385	[109]
carbamate		1322	[109]
experimental observations		1067, 1019	[109]

IDENTIFICATION OF PEAKS IN PEI-600

Based on table A.6, similar peaks were identified in PEI-600 through experimentally collecting samples of PEI-600 and analysing it. Figure A.7 shows the spectrum of pure PEI-600 obtained from the OMNIC software.

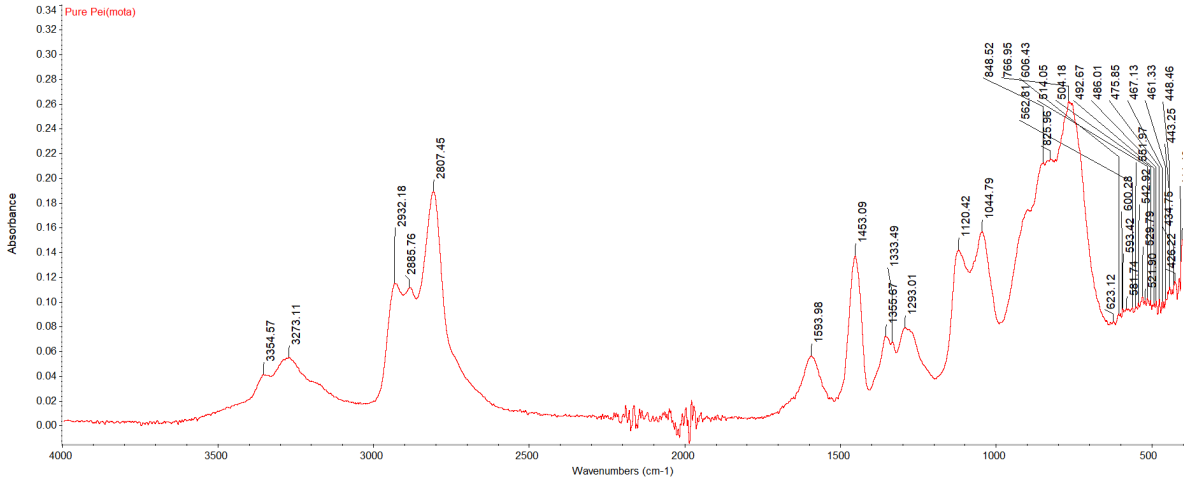

Figure A.7: The spectrum of Pure PEI-600 obtained from OMNIC

Based on the information collected from the literature, the peaks in pure PEI-600 were identified and are summarized in table A.7.

Table A.7: Peaks of PEI-600 found in this thesis

Pure PEI -600 (This Thesis)		
Group	**Type**	**Peaks**
N-H strech	Primary & secondary amine	3354.57, 3273.11
C-H stretch	alkyl group	2932.18, 2885.76
N-H bend	primary amine	1593.98
C-H bend	alkyl group	1453.09, 1355.67
C-N stretch	aliphatic amines	1120.42, 1044.79
N-H wag	primary & secondary amines	756

IDENTIFICATION OF PEAKS IN TEPA

Similarly the spectrum obtained for Pure TEPA can be seen in figure A.8.

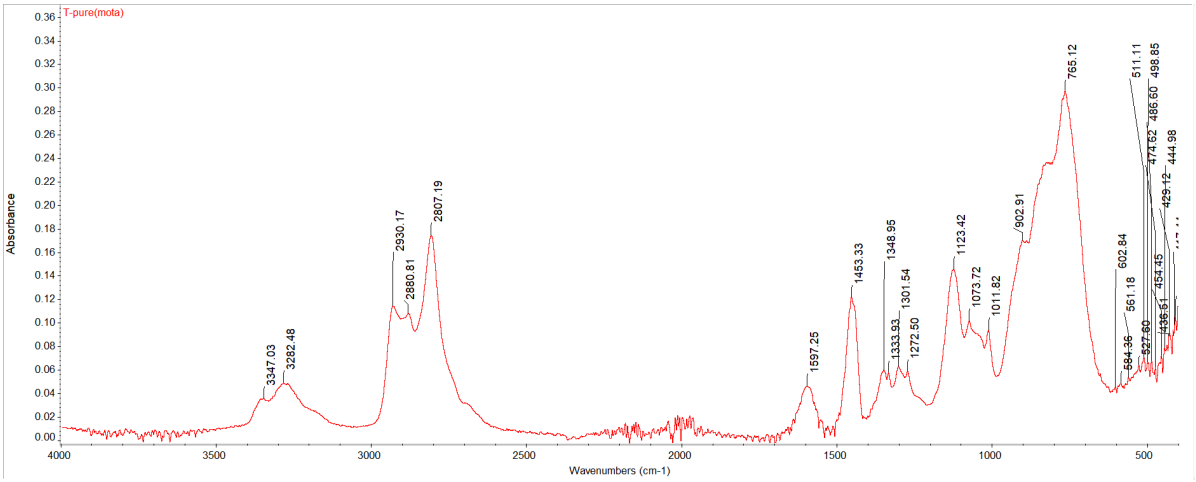

Figure A.8: The spectrum of Pure TEPA obtained from OMNIC

Based on the information collected from the literature, the peaks in pure TEPA were identified and are summarized in table A.8.

Table A.8: Peaks of TEPA found in this thesis

Pure TEPA (This Thesis)		
Group	**Type**	**Peaks**
N-H strech	Primary & secondary amine	3347.03, 3282.48
C-H stretch	alkyl group	2930.17, 2880.81
N-H bend	primary amine	1597.25
C-H bend	alkyl group	1453.33, 1348.95
C-N stretch	aliphatic amines	1123.42, 1073.72
N-H wag	primary & secondary amines	765.12

Note: the CO_2 peaks were found similar to that in MEA (although slightly shifted). They are not shown here because pure amines do not contain any CO_2. A bicarbonate peak was not found in both PEI-600 and TEPA.

A.3.4. CALIBRATION OF FTIR

Although infrared spectroscopy is mostly used for qualitative analysis, quantitative analysis methods can also be applied to a spectrum. This can be done using a software tool called "TQ Analyst" which is used to extract information from spectra. Using this software, measurements can be done on different peak height, width, ratio, location and area to check the presence of a component [111].A robust method for quantitative analysis can be developed using this tool which can be calibrated using known sample spectra. Using this method, unknown compositions of similar materials can be calculated. The quality of the calibration can also be seen in the calibration result window where performance factors like RMSEC, RMSEP and correction coefficients are displayed along with the calibration curve.

STEP 1

The first step is to open the "TQ Analyst" software and choose an analysis type. For complex analysis and accurate results, a partial least square analysis method was chosen. Figure A.9 shows the software's interface.

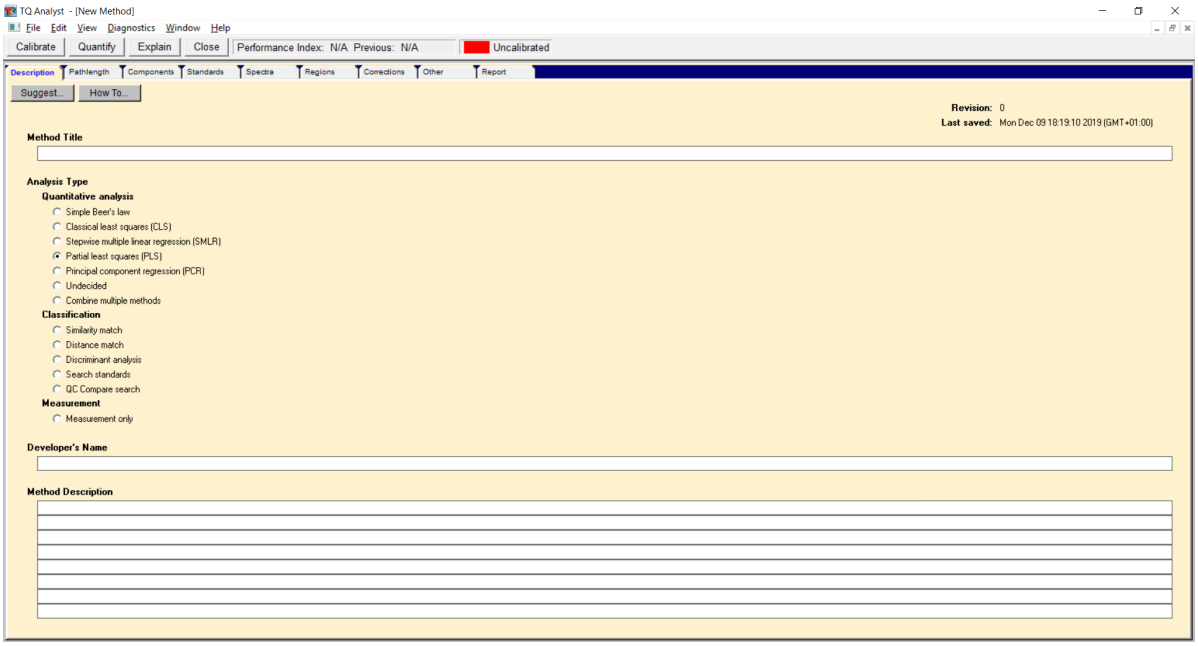

Figure A.9: The interface of the TQ analyst software

STEP 2

After the analysis method is chosen, the components in the samples being calibrated are specified with the required measurement units. This can be seen in figure A.10.

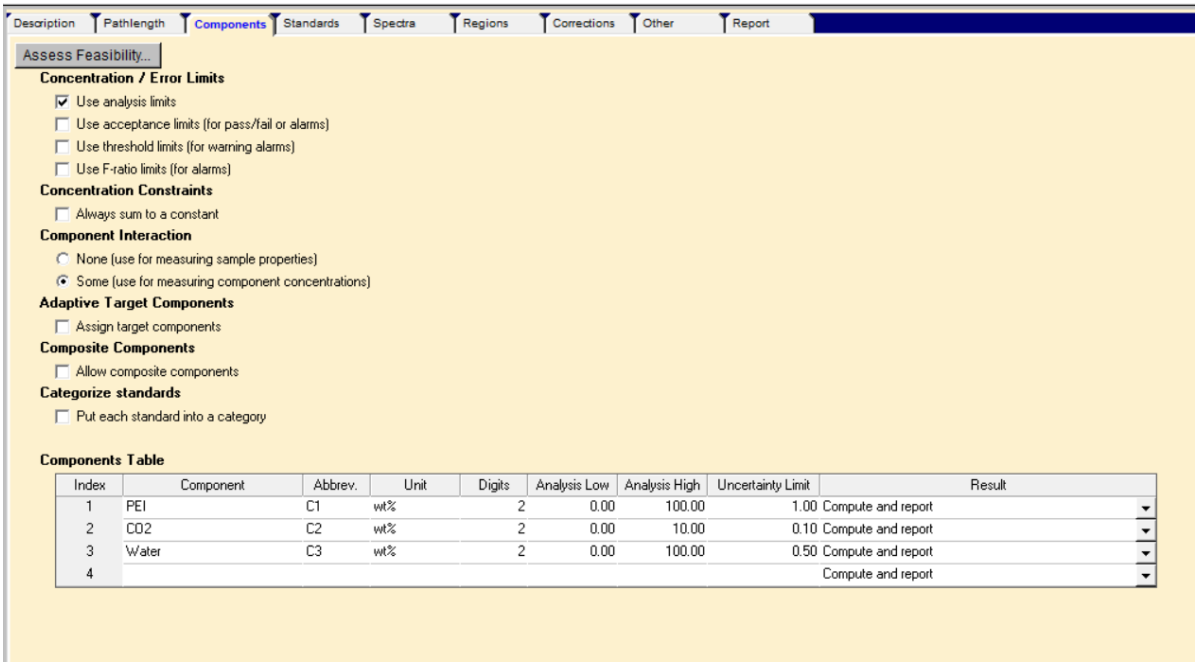

Figure A.10: Specifying the components in the calibrating software

STEP 3

Subsequently, the spectrum of samples whose component concentrations are know are uploaded to the software. The percentage of calibrating and validating samples are chosen. This can be seen in figure A.11.

Standards Table: 19 Calibration, 4 Validation

Index	Select	Spectrum Title	Usage	PEI	CO2	Water
1		P-29.911-1.5375	Calibration	68.78	1.69	29.53
2		P-10.06-4.1	Calibration	84.32	4.63	11.05
3		P-10.23-2.6	Calibration	85.79	3.02	11.19
4		P-20.06-4.1	Calibration	75.29	4.55	20.16
5		P-20.21-2.41	Calibration	76.59	2.64	20.77
6		P-29.6-3	Calibration	68.08	3.15	28.77
7		P-30W(mota)	Validation	68.56	0.02	31.42
8		BM-P-10W	Calibration	89.29	0.15	10.56
9		BM-P-20W	Calibration	78.46	0.46	21.08
10		BM-P-30W	Calibration	69.76	0.45	29.79
11		BM-P-40W	Calibration	55.52	6.88	37.60
12		P-10W(mota)	Validation	88.69	0.02	11.29
13		P-20W(mota)	Calibration	79.68	0.02	20.30
14		5-final	Calibration	81.79	0.53	17.68
15		1-final	Calibration	86.48	0.37	13.15
16		2-final	Validation	79.58	0.65	19.77
17		P-40W(mota)	Calibration	60.26	0.02	39.72
18		3-final	Calibration	88.66	0.44	10.90
19		P-30.5-5.63	Calibration	63.33	7.12	29.55
20		P-30-0co2	Calibration	71.24	1.37	27.39
21		Pure Pei(mota)	Calibration	97.96	0.10	1.94

Figure A.11: Uploading spectrum to known samples to calibrate the software

STEP 4

This step is the most important step in the calibration process. All regions with peaks pertaining to H_2O, CO_2 and amine are specified clearly. If these regions are not known, the calibration would not be accurate. An example for the peaks with information regarding CO_2 is shown in the figure A.12.

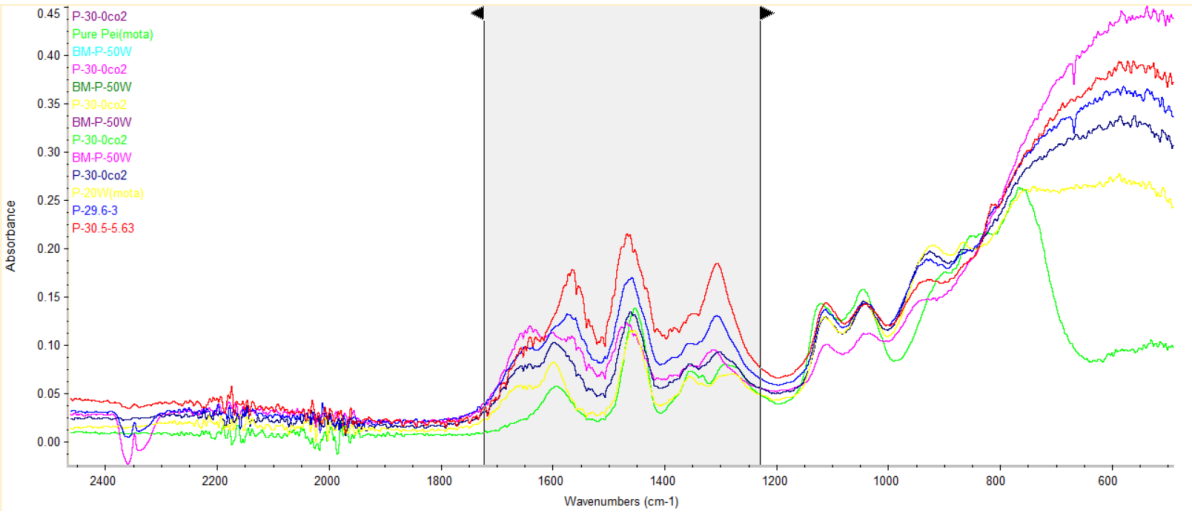

Figure A.12: Region showing the section where CO_2 influences the peaks

STEP 5

After setting all the parameter and following the steps above, the calibration can be run. Figures A.13-A.16 show the calculated vs the actual values for CO_2 and H_2O concentrations for PEI-600 and TEPA with their mean absolute error and coefficient of deviation.

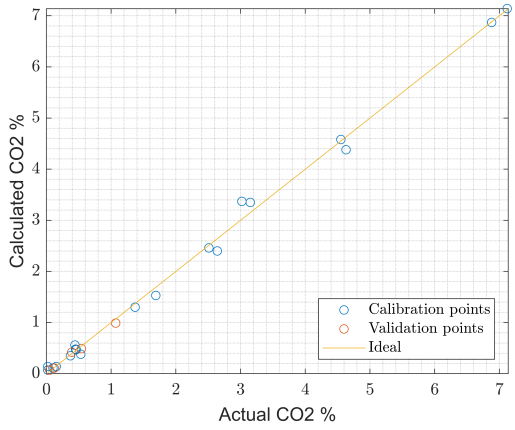

Figure A.13: CO_2 calibration curve for PEI-600. Mean absolute error is 0.1 and R^2 (coefficient of deviation) is 0.998

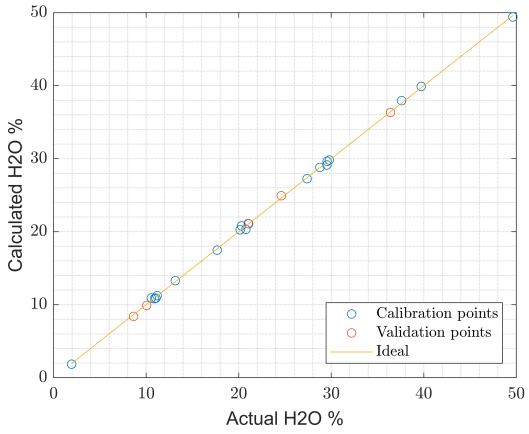

Figure A.14: H_2O calibration curve for PEI-600. Mean absolute error is 0.185 and R^2 (coefficient of deviation) is 0.9998

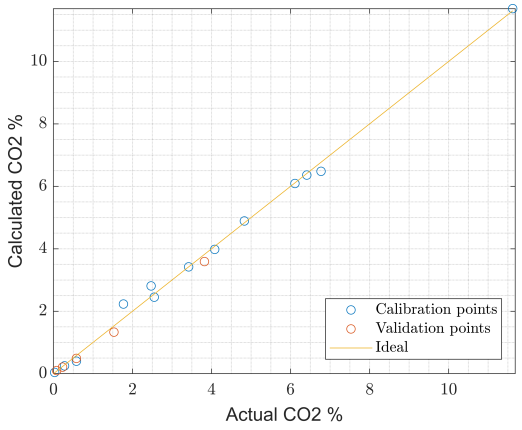

Figure A.15: CO_2 calibration curve for TEPA. Mean absolute error is 0.12 and R^2 (coefficient of deviation) is 0.9984

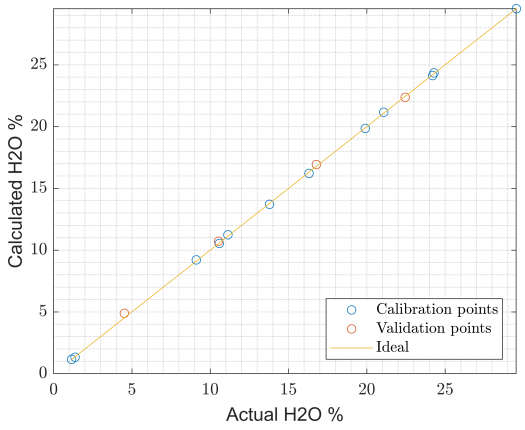

Figure A.16: H_2O calibration curve for TEPA. Mean absolute error is 0.067 and R^2 (coefficient of deviation) is 1

This calibration can be used to quantify any spectrum of PEI-600 and TEPA respectively using the OMNIC software.

A.4. CONTRAVES LOW SHEAR 40

This section explains the working of Low Shear 40 rheometer that was used in this thesis. Figure A.17 shows a sectional view of the rheometer.

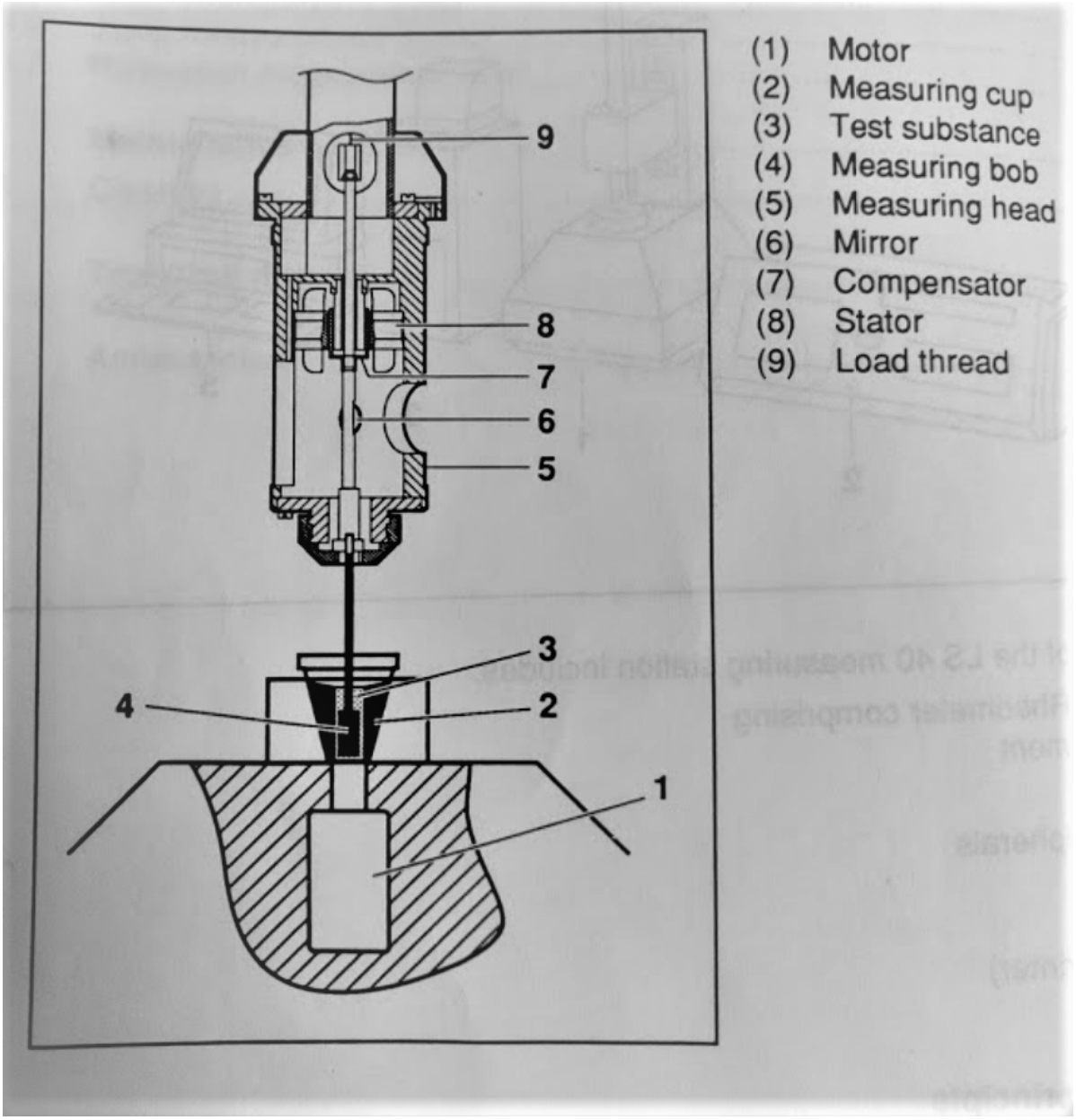

Figure A.17: Sectional view of Low Shear 40 Rheometer used in this thesis [24]

To begin the process of viscosity measurement, a sample (3) of about 5ml is put in the measuring cup (2), the measuring bob (4) is fixed to the measuring head (5) and the measuring bob (4) is lowered down to the measuring cup as shown in figure A.17 such that the test substance (3) is located in the gap between the measuring cup (2) and the measuring bob (4). Now the measurements can begin. The measuring cup (2) is driven by the motor (1). A torque is exerted on the measuring bob due to the friction between the test substance and the measuring bob. The measuring head has a deflection system which the measuring bob is coupled with. The deflection system consists of a compensator (7) and a mirror (6) which are suspended by a load thread (9). On the other hand, the stator (8) is permanently fixed to the measuring head. The measuring bob transmits the deflection to the system which is optically scanned and compensated. The measuring head measures the torque exerted on the system. Viscosity and shear stress is derived from this torque and shown on

the interface.

B

ALL RELEVANT EXPERIMENTAL DATA

B.1. CHANNEL EXPERIMENTAL DATA (PEI-600 AND TEPA)

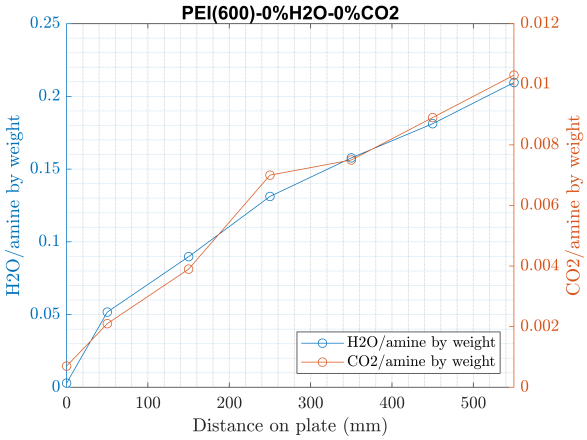

Figure B.1: Starting concentration of 0% CO_2 and 0% H_2O with a flow rate of 0.08 ml/min

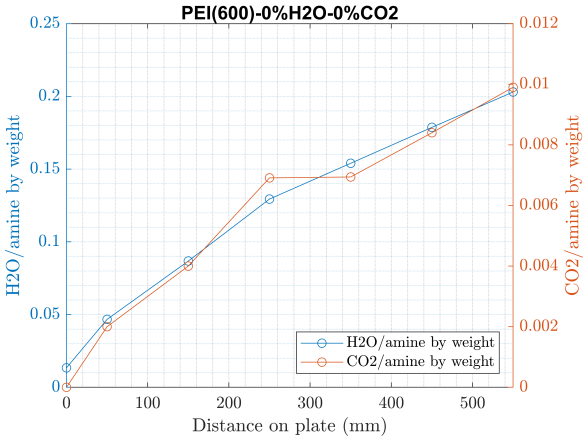

Figure B.2: Starting concentration of 0% CO_2 and 0% H_2O with a flow rate of 0.08 ml/min

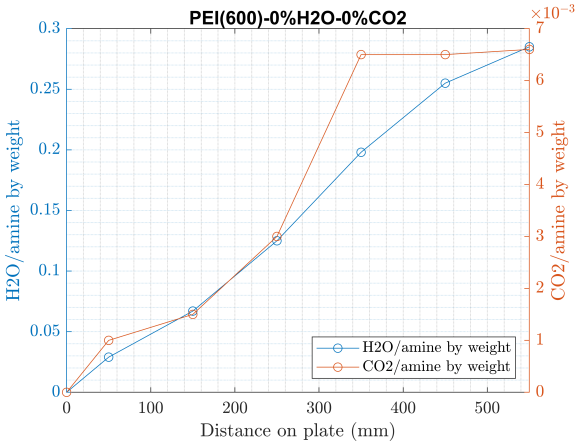

Figure B.3: Starting concentration of 0% CO_2 and 0% H_2O with a flow rate of 0.1 ml/min

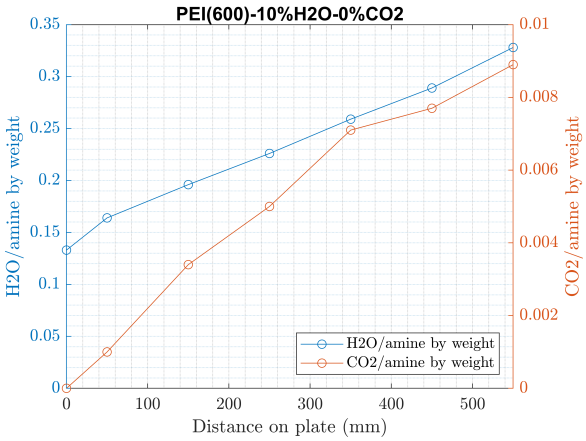

Figure B.4: Starting concentration of 0% CO_2 and 10% H_2O with a flow rate of 0.08 ml/min

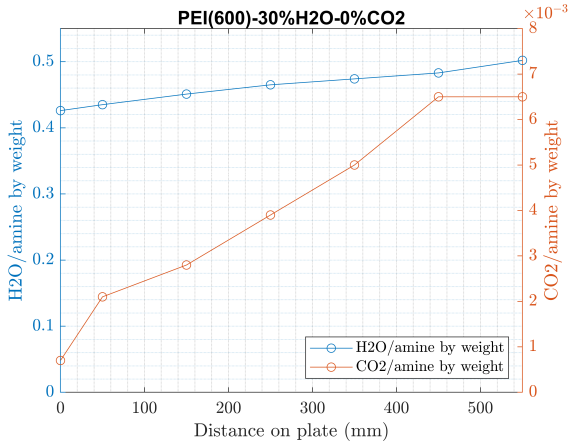

Figure B.5: Starting concentration of 0% CO_2 and 30% H_2O with a flow rate of 0.08 ml/min

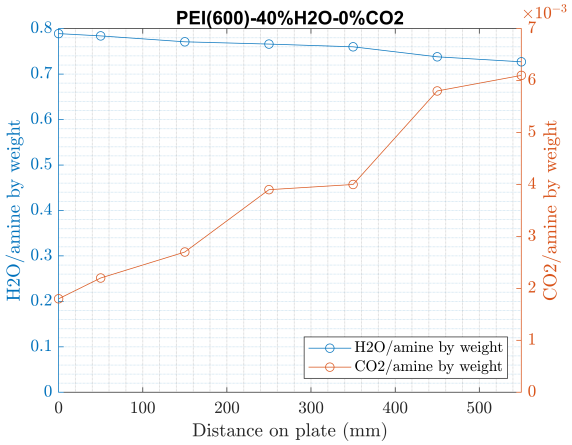

Figure B.6: Starting concentration of 0% CO_2 and 40% H_2O with a flow rate of 0.08 ml/min

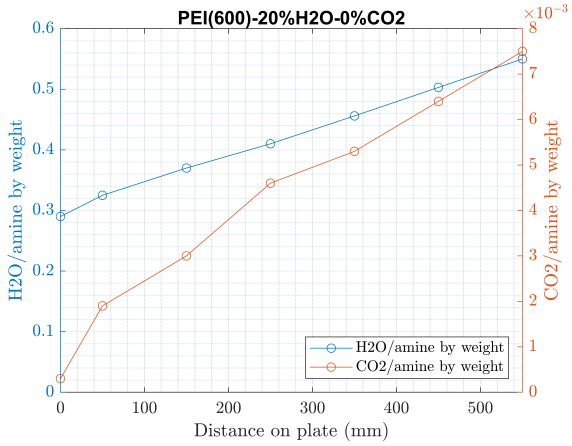

Figure B.7: Starting concentration of 0% CO_2 and 20% H_2O with a flow rate of 0.08 ml/min

Figure B.8: Starting concentration of 0% CO_2 and 10% H_2O with a flow rate of 0.08 ml/min

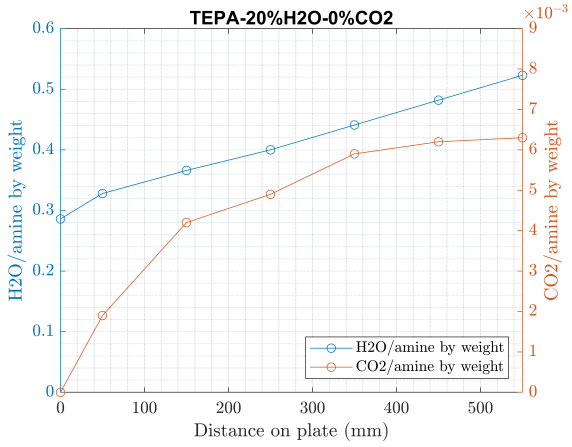

Figure B.9: Starting concentration of 0% CO_2 and 20% H_2O with a flow rate of 0.08 ml/min

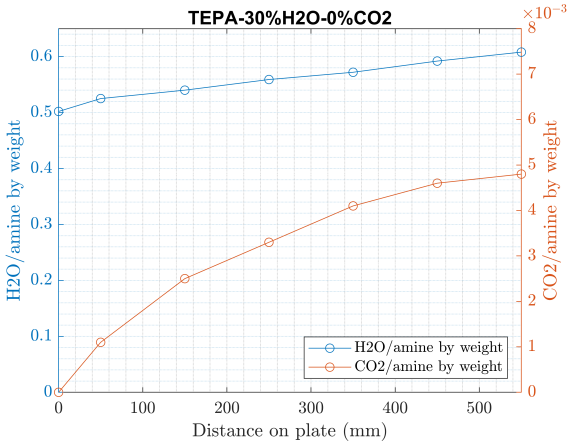

Figure B.10: Starting concentration of 0% CO_2 and 30% H_2O with a flow rate of 0.08 ml/min

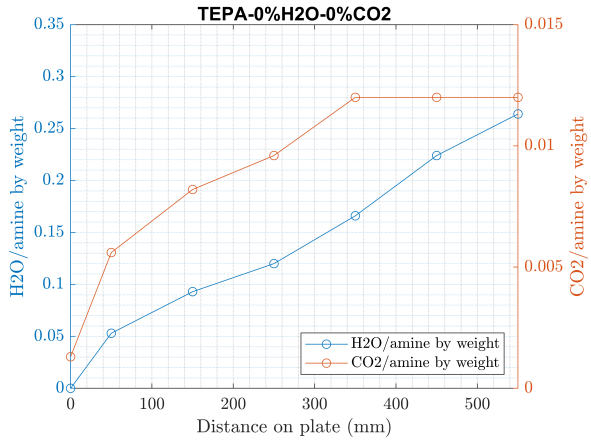

Figure B.11: Starting concentration of 0% CO_2 and 0% H_2O with a flow rate of 0.08 ml/min

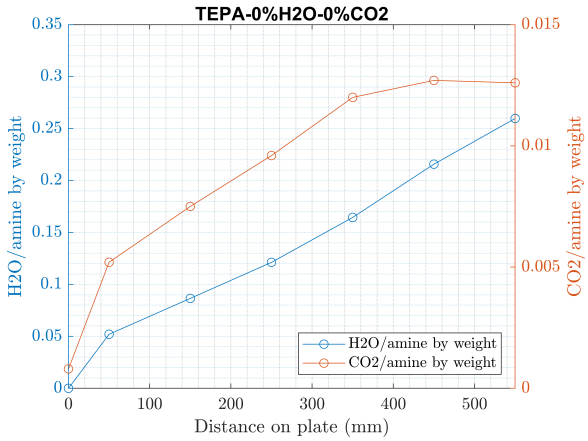

Figure B.12: Starting concentration of 0% CO_2 and 0% H_2O with a flow rate of 0.08 ml/min

B.2. VISCOSITY 3D PLOTS

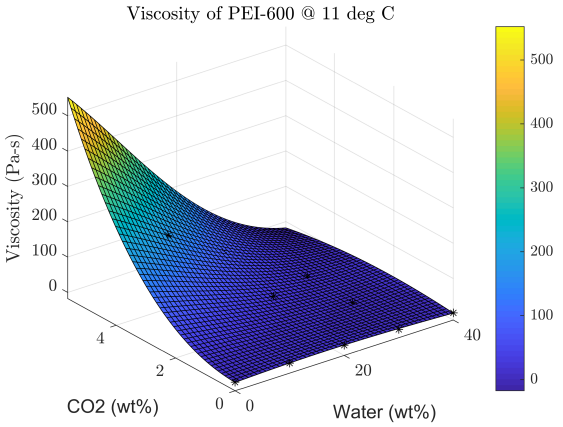

Figure B.13: Viscosity of PEI-600 at 11°C

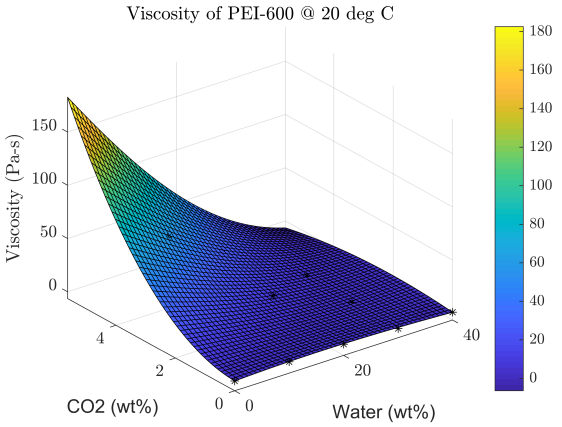

Figure B.14: Viscosity of PEI-600 at 20°C

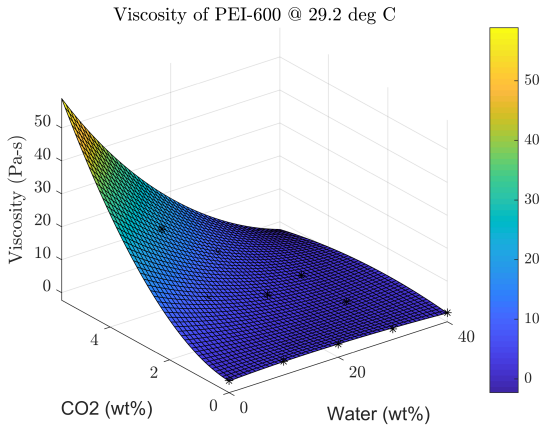

Figure B.15: Viscosity of PEI-600 at 29.2°C

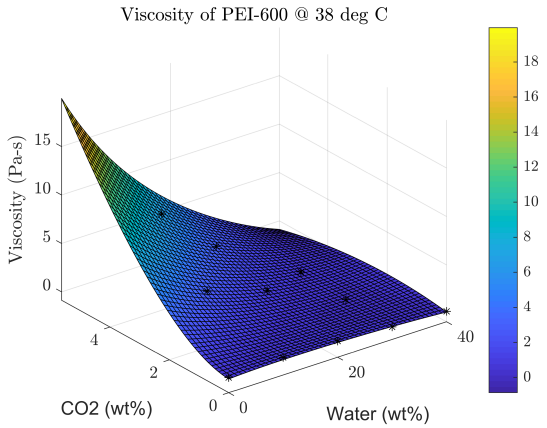

Figure B.16: Viscosity of PEI-600 at 38°C

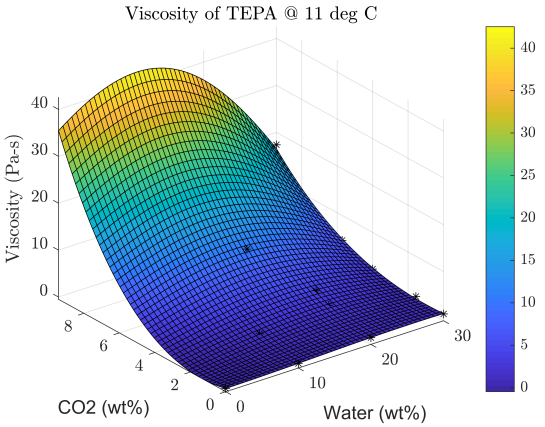

Figure B.17: Viscosity of TEPA at 11°C

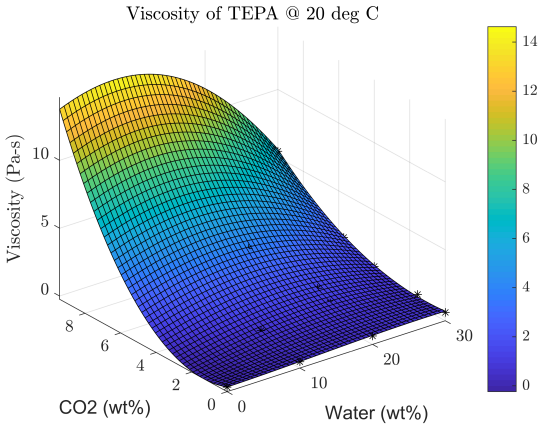

Figure B.18: Viscosity of TEPA at 20°C

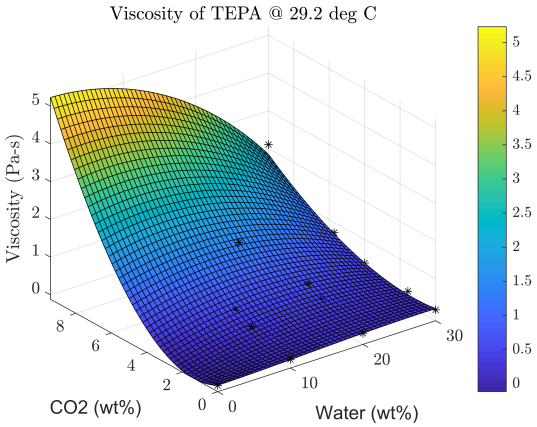

Figure B.19: Viscosity of TEPA at 29°C

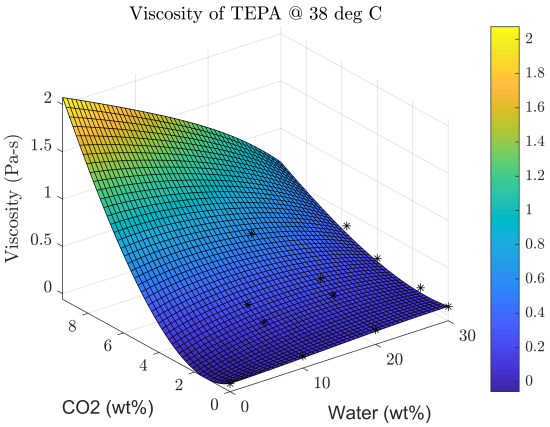

Figure B.20: Viscosity of TEPA at 38°C

C

MISCELLANEOUS

C.1. pH MEASUREMENTS

Table C.1: pH of PEI-600 and TEPA with varying concentrations of CO_2 and H_2O

Sample	water %	CO2%	Sorbent (ml)	Buffer(ml)	pH of sorbent
TEPA	0	0	0.3	1	12.6868
TEPA	10	0	0.3	1	12.6168
TEPA	20	0	0.3	1	12.5768
TEPA	30	0	0.3	1	12.4968
TEPA	10.32	2.32	0.35	2	11.907
TEPA	10.25	3.2	0.35	2	11.787
TEPA	15.55	5.17	0.35	2	11.797
TEPA	20.195	2.46	0.35	2	11.6769
TEPA	20.25	3.2	0.35	2	11.4969
TEPA	30	1.56	0.35	2	11.917
TEPA	30	4	0.35	2	11.6469
TEPA	30	5.725	0.35	2	11.3069
TEPA	30	9.43	0.35	2	10.8867
PEI	0	0	0.35	1	12.2063
PEI	10	0	0.3	1	12.1668
PEI	20	0	0.3	1	12.1168
PEI	30	0	0.3	1	12.0968
PEI	40	0	0.35	1	12.0263
PEI	10.23	2.6	0.35	2	11.6969
PEI	10.06	4.1	0.35	2	11.5069
PEI	20.21	2.41	0.35	2	11.6269
PEI	20.06	4.1	0.35	2	11.4469
PEI	29.911	1.5375	0.3	2	11.7646
PEI	29.6	3	0.35	2	11.4869
PEI	30.5	5.63	0.3	2	11.1744

During this thesis, pH measurements were done on the loaded amine samples in hopes of finding a trend to calibrate the experimental setup. However to time constraints and the complexity of such a setup, the idea was dropped. Table C.1 shows the measured value of the pH for all amine samples. **Note: A buffer solution was mixed to calculate the pH of amine samples. These values should not be considered accurate. The actual pH values are expected to be higher than what is shown. This data is just being presented to observe the change in trend of pH with varying CO_2 and H_2O concentrations.**

Figures C.1 and C.2 show the variation of pH with different CO_2 and H_2O concentrations.

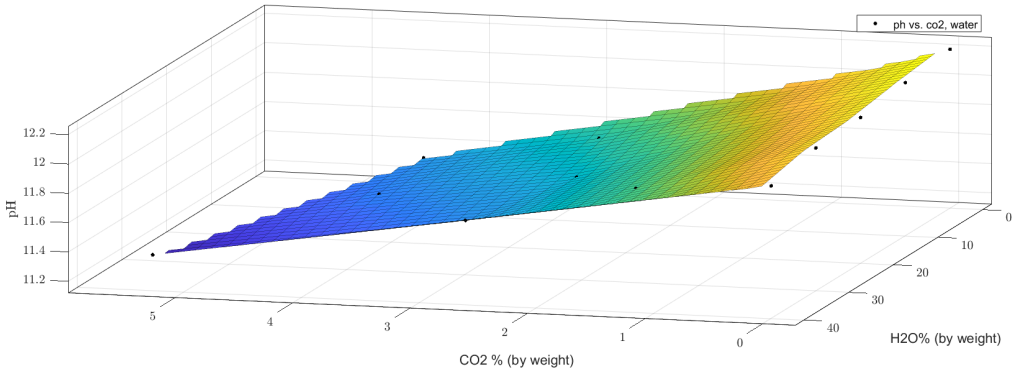

Figure C.1: pH of PEI-600 with varying concentrations of CO_2 and H_2O

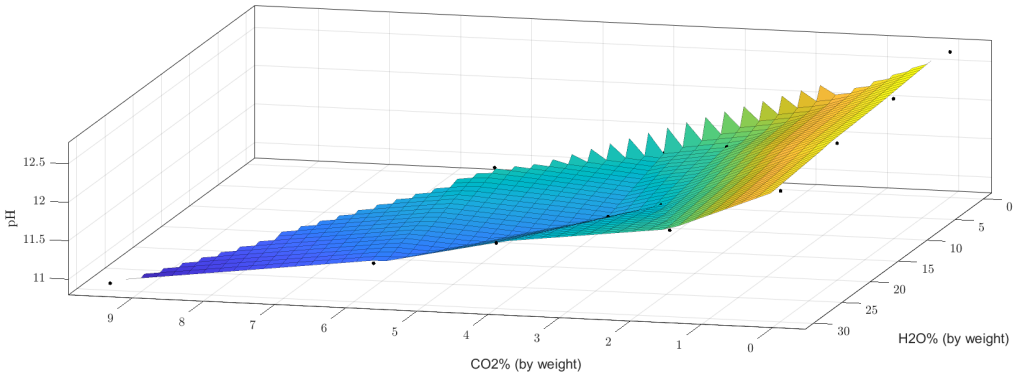

Figure C.2: pH of TEPA with varying concentrations of CO_2 and H_2O

Some research on different pH dyes was also done in this thesis. Table C.2 shows all the different types of dyes that can be used for pH or hue measurements if needed.

Table C.2: pH dyes that could be used for pH measurements by future researchers [25]

Name	pH Change/color change	
ACID BLUE 89	11 (blue)	12 (red)
ACID BLUE 92	11 (blue)	12 (pink)
ACID FUCHSIN	12 (red)	14 (colorless)
ALIZARIN RED	10.1 (red)	12.1 (purple)
ALIZARIN YELLOW GG	10 (yellow)	12 (orange)
ALIZARIN YELLOW R	10(yellow)	12.1 (orange)
ALKALI BLUE	9.4 (blue-violet)	14 (red-pink)
ANILINESULFONEPHTHALEIN	11.75 (violet)	12.53 (yellow)
CHROME ORANGE GR	10.5 (yellow)	12 (red)
CLAYTON YELLOW	11 (yellow)	13 (red)
2,4-DINITROPHENYLHYDRAZINE	11 (yellow)	12.5 (brown)
GALLEIN	10.6 (pink)	13 (violet)
INDIGO CARMINE	11.5 (blue)	14 (yellow)
INDOPHENOL	6.3 (red)	12.3 (blue)
LANACYL VIOLET BF	11 (violet)	13 (orange)
MALACHITE GREEN	11.6 (green)	14 (colorless)
NITRAMINE	10.8 (colorless)	13 (red-brown)
p-NITROBENZYLCYANIDE	11.4 (yellow)	12.9 (orange-red)
ORANGE II	10.2 (orange)	11.8 (red)
POIRRIER BLUE	11 (blue)	13 (violet-red)
PYROGALLOLPHTHALEIN	10.6 (pink)	13 (violet)
SALICYL YELLOW	10 (yellow)	12 (orange)
TETRYL	10.8 (colorless)	13 (red-brown)
THIAZOL YELLOW G	11 (yellow)	13 (red)
TRINITROBENZENE	11.5 (colorless)	14 (orange)
TRINITROTOLUENE	11.5 (colorless)	14 (orange)
TROPAEOLIN O	11 (yellow)	12.7 (red)
TRINITROBENZOIC ACID	12(colorless)	13.4 (orange)
DIRECT BLUE 72	13 (blue)	14 (violet)
ANTHRANILIC ACID	12.5 (florescence)	14 (florescence)

C.2. CONDUCTANCE MEASUREMENTS

Similar to pH experiments, conductance experiments were also performed to find a way to calibrate the setup. Although the data was obtained, the idea was dropped due to the time constraints and complexity of the setup. However, the data collected can be useful and used by future researchers and therefore, it is presented here in the appendix. Tables C.3 and C.4 show the values of conductance obtained for various PEI-600 and TEPA samples. Figures C.3 and C.4 are 3D plots of these values showing how conductance varies with varying CO_2 and H_2O concentrations.

Table C.3: Measured conductance of PEI-600 samples with varying CO_2 and H_2O concentrations

H2O% (by weight)	CO2% (by weight)	Conductance (mS)
0	0	0.8
10	0	10.7
20	0	22.5
30	0	44.6
40	0	86.8
10.23	2.6	8.9
10.06	4.1	6.7
20.21	2.41	28.1
20.06	4.1	25.6
29.911	1.5375	63.3
29.6	3	67.4
30.5	5.63	70.5

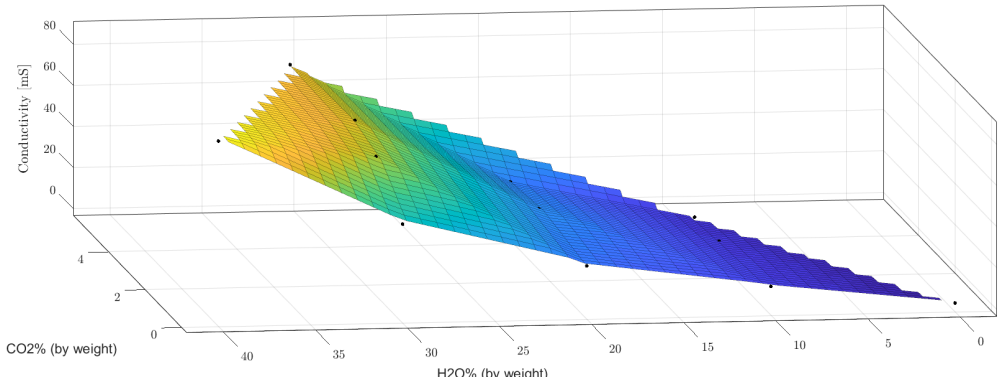

Figure C.3: Conductance variations in PEI-600 samples with different CO_2 and H_2O concentrations.

Table C.4: Measured conductance of TEPA samples with varying CO_2 and H_2O concentrations

H2O% (by weight)	CO2% (by weight)	Conductivity (mS)
0	0	0
10	0	0.9
20	0	2.4
30	0	4.4
10.32	2.32	23.5
15.55	5.17	45
10.25	3.2	25.9
20.195	2.46	74.8
20.25	3.2	64.5
30	1.56	94.5
30	4	145.8
30	5.725	173.6
30	9.43	127.6

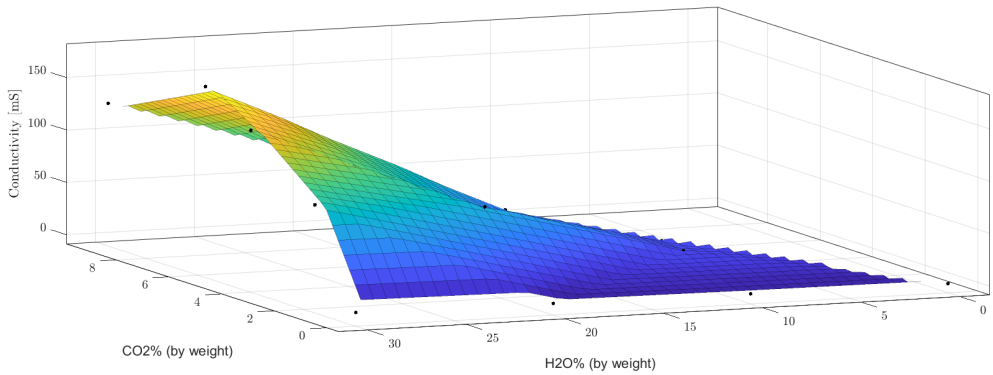

Figure C.4: Conductance variations in TEPA samples with different CO_2 and H_2O concentrations.

C.3. PRESSURE DROP IN ABSORPTION COLUMN

In order to find the power consumption of the fan used in the absorption column, the pressure drop of air through the column needs to be calculated. The column consists of many parallel plates equally spaced where sorbent flows through multiple channels in each plate and the air flow is counter current to the sorbent.

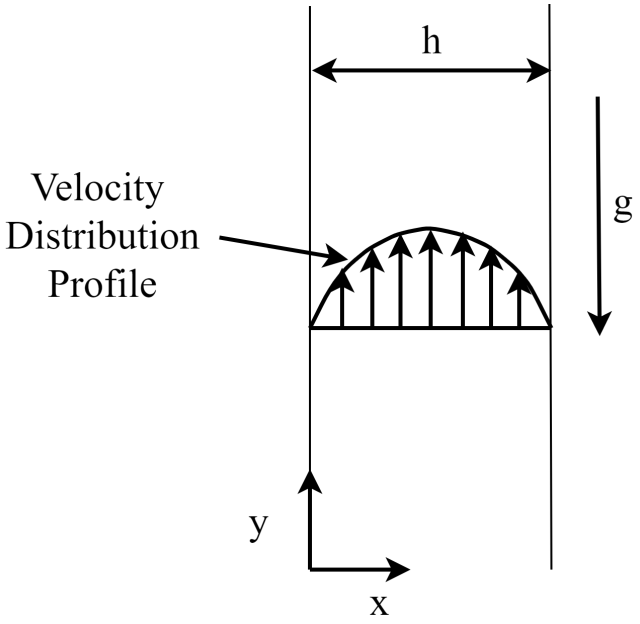

Figure C.5: Depiction of air flow between two parallel plates in the absorption column

Figure C.5 depicts the airflow between two parallel plates in the absorption column where h is the spacing between the two plates, and the velocity profile can be represented as similar to Poiseuille flow as shown. The width into the page is considered to be unity. Consider the two dimensional Navier-Stokes equation in Cartesian coordinates.

Continuity Equation

$$\frac{\partial u}{\partial x} + \frac{\partial v}{\partial y} = 0 \tag{C.1}$$

x-Momentum Equation

$$\frac{\partial u}{\partial t}+u\frac{\partial u}{\partial x}+v\frac{\partial u}{\partial y}=-\frac{1}{\rho}\frac{\partial P}{\partial x}+\frac{\mu}{\rho}(\frac{\partial^2 u}{\partial x^2}+\frac{\partial^2 u}{\partial y^2})+g_x \tag{C.2}$$

y-Momentum Equation

$$\frac{\partial v}{\partial t}+u\frac{\partial v}{\partial x}+v\frac{\partial v}{\partial y}=-\frac{1}{\rho}\frac{\partial P}{\partial y}+\frac{\mu}{\rho}(\frac{\partial^2 v}{\partial x^2}+\frac{\partial^2 v}{\partial y^2})+g_y \tag{C.3}$$

The velocity in x-direction is 0, therefore, u=0. Thus equation C.1 reduces to:

$$\frac{\partial v}{\partial y}=0 \tag{C.4}$$

Considering steady state, u=0, no acceleration in x-direction (g_x = 0) and equation C.4, equation C.2 can be reduced to

$$-\frac{1}{\rho}\frac{\partial P}{\partial x}=0 \tag{C.5}$$

Based on equation C.5, the pressure doesn't vary in the x-direction and it can be concluded that pressure only varies with y or $P = f(y)$. Similarly, the y-momentum equation (C.3) would reduce to

$$0=-1\frac{1}{\rho}\frac{\partial P}{\partial y}+\frac{\mu}{\rho}\frac{\partial^2 v}{\partial x^2}-g \tag{C.6}$$

Note that g_y has been replaced by $-g$ since the acceleration due to gravity is in the negaive direction as shown in figure C.5. In order to find the velocity profile, equation C.6 has to be integrated twice. Rearranging the equation and integrating once would give the following:

$$\int(\frac{1}{\rho}\frac{\partial P}{\partial y}+g)dx=\frac{\mu}{\rho}\int\frac{\partial}{\partial x}(\frac{\partial v}{\partial x})dx \tag{C.7}$$

Since the left hand side of equation C.7 is not a function of x, integrating would result in the following.

$$(\frac{1}{\rho}\frac{\partial P}{\partial y}+g)x=\frac{\mu}{\rho}\frac{\partial v}{\partial x}+C_1 \tag{C.8}$$

Integrating equation C.8 again would result in the following.

$$(\frac{1}{\rho}\frac{\partial P}{\partial y}+g)\frac{x^2}{2}=\frac{\mu}{\rho}v+C_1x+C_2 \tag{C.9}$$

Rearranging equation C.9 and replacing constants C_1,C_2 by new constants A and B, we get the following velocity profile.

$$v(x)=\frac{\rho}{\mu}[(\frac{1}{\rho}\frac{\partial P}{\partial y}+g)\frac{x^2}{2}+Ax+B] \tag{C.10}$$

In order to find value of constants A and B, no slip boundary condition can be applied at x=0 and x=h. At x=0, V(0)=0 and therefore, the equation C.10 reduces to B=0. Now applying

V(h)=0 at x=h, the value of A can be achieved.

$$A = -\frac{h}{2}[\frac{1}{\mu}\frac{\partial P}{\partial y} + \frac{\rho g}{\mu}] \tag{C.11}$$

Putting the values of A and B in equation C.10, we get the velocity profile.

$$\boxed{V(x) = (\frac{1}{\mu}\frac{\partial P}{\partial y} + \frac{\rho g}{\mu})\frac{x}{2}[x-h]} \tag{C.12}$$

Equation C.12 can be used to find the volumetric flow rate (Q). Considering a small element, dx and depth into the page as unity, Q can be achieved by the following equation.

$$Q = \int_{x=0}^{x=h} v(x).dx.1 \tag{C.13}$$

Solving equation C.13, we get the equation for volumetric flowrate Q.

$$\boxed{Q = -\frac{h^3}{12\mu}[\frac{\partial P}{\partial y} + \rho g]} \tag{C.14}$$

Assuming uniform pressure drop, $\frac{\partial P}{\partial y}$ can be written as $\frac{\Delta P}{\Delta L}$, where ΔL is the length of the plates being considered. Therefore, the equation to find the pressure drop across two parallel vertical plates can be written as following.

$$\boxed{\Delta P = -[(\frac{12Q\mu}{h^3}) + \rho g]L} \tag{C.15}$$

Since the effect of gravity is similar on the air outside the plates, the term ρg can be neglected from the derivation. Therefore the final equation for the pressure drop is equation C.16.

$$\boxed{\Delta P = -[(\frac{12Q\mu}{h^3})]L} \tag{C.16}$$

BIBLIOGRAPHY

[1] H. Ritchie and M. Roser, *Energy Production & Changing Energy Sources,* (last accessed 06 August 2019).

[2] H. Ritchie and M. Roser, *Fossil Fuels,* (last accessed 18 August 2019).

[3] *Carbon Dioxide,* (last accessed 2 August 2019).

[4] C. P. Morice, J. J. Kennedy, N. A. Rayner, and P. D. Jones, *Quantifying uncertainties in global and regional temperature change using an ensemble of observational estimates: The HadCRUT4 data set,* Journal of Geophysical Research: Atmospheres **117** (2012), 10.1029/2011JD017187.

[5] *Zero Emission Fuels - Methanol from sunlight and air,* (last accessed 10 September 2019).

[6] M. Fasihi, O. Efimova, and C. Breyer, *Techno-economic assessment of CO2 direct air capture plants,* Journal of Cleaner Production **224**, 957 (2019).

[7] D. W. Keith, G. Holmes, D. St. Angelo, and K. Heidel, *A Process for Capturing CO2 from the Atmosphere,* Joule **2**, 1573 (2018).

[8] O. Azzalini, *Designing a carbon dioxide adsorption unit for producing sustainable synthetic fuels.*, Ph.D. thesis, Delft University of Technology (2018).

[9] R. W. van den Berg, *DESIGNING A DIRECT AIR CAPTURE UNIT FOR METHANOL SYNTHESIS*, Ph.D. thesis, Delft University of Technology (2018).

[10] M. Sinha, *Experimental study of absorption and desorption in a continuous direct air capture system to build a concept model*, Tech. Rep. (Delft University of Technology, Delft,Netherlands, 2018).

[11] J. Seader and J. E. Henley, *SEPARATION PROCESS PRINCIPLES*, 2nd ed., p. 791.

[12] K. Weissermel and H. Arpe, *Industrial Organic Chemistry* (Wiley, 2003).

[13] M. Frauenkron, J.-P. Melder, G. Ruider, R. Rossbacher, and H. Höke, *Ethanolamines and Propanolamines,* in *Ullmann's Encyclopedia of Industrial Chemistry* (Wiley-VCH Verlag GmbH & Co. KGaA, Weinheim, Germany, 2001).

[14] R. Veneman, *Adsorptive systems for post-combustion CO2 capture : design, experimental validation and evaluation of a supported amine based process*, Ph.D. thesis, University of Twente, Enschede, The Netherlands (2015).

[15] B. L Fernandes and J. R Figueiredo, *Modeling Viscosity of Liquid Ammonia-Water Mixture,* **15**, 51 (2012).

[16] Nouryon, *Technical Data Sheet TETRAETHYLENEPENTAMINE (TEPA),* (2019).

[17] Huntsman, *Technical Bulletin TETRAETHYLENEPENTAMINE (TEPA),* (2008).

[18] M. Jäger, S. Schubert, S. Ochrimenko, D. Fischer, and U. S. Schubert, *Branched and linear poly(ethylene imine)-based conjugates: synthetic modification, characterization, and application,* Chemical Society Reviews **41**, 4755 (2012).

[19] N. SHOKUBAI, *Epomin Polyment (PDF),* (2014).

[20] S. KD, *kd Scientific - Model 100 Series User's Manual,* (2014).

[21] M. TOLEDO, *Good Titration Practice™ in Karl Fischer Titration,* (2014).

[22] A. Adeosun, N. El Hadri, E. L. Goetheer, and M. R. AbuZahra, *Absorption of CO2by Amine Blends Solution: An Experimental Evaluation,* International Journal Of Engineering And Science **3**, 12 (2013).

[23] G. Forensics, *How does Fourier Transform Infrared (FTIR) Spectroscopy Work?* (last accessed on 15 November 2019).

[24] M. TOLEDO, *Operating Instructions - Low Shear 40,* ().

[25] R. W. Sabnis, *Handbook of Acid-Base Indicators* (CRC Press, 2007).

[26] A. Goeppert, M. Czaun, G. K. Surya Prakash, and G. A. Olah, *Air as the renewable carbon source of the future: an overview of CO2 capture from the atmosphere,* Energy & Environmental Science **5**, 7833 (2012).

[27] J. G. Olivier and J. A. Peters, *Trends in global CO2 and total greenhouse gas emissions*, Tech. Rep. (PBL Netherlands Environmental Assessment Agency, The Hague, 2018).

[28] *Global Energy & CO2 Status Report,* (last accessed on 18 August 2019).

[29] J. Gills, *Earth Sets a Temperature Record for the Third Straight Year,* (2017).

[30] M. McGrath, *Climate change: Data shows 2016 likely to be warmest year yet,* (2017).

[31] M. Bui, C. S. Adjiman, A. Bardow, E. J. Anthony, A. Boston, S. Brown, P. S. Fennel, S. Fuss, A. Galindo, and L. A. Hackett, *Carbon capture and storage (CCS): the way forward,* Energy & Environmental Science (2018).

[32] M. Aresta, *Carbon Dioxide as Chemical Feedstock* (2010).

[33] A. Dibenedetto, A. Angelini, and P. Stufano, *Use of carbon dioxide as feedstock for chemicals and fuels: homogeneous and heterogeneous catalysis,* Journal of Chemical technology and Biotechnology **89**, 334 (2013).

[34] A. Adegbulugbe, Ø. Christophersen, H. Ishitani, W. Moomaw, and J. Moreira, *IPCC Special Report on Carbon dioxide Capture and Storage*, Tech. Rep. (Cambridge University, 2005).

[35] E. S. Sanz-Pérez, C. R. Murdock, S. A. Didas, and C. W. Jones, *Direct Capture of CO2 from Ambient Air,* **116**, 11840 (2016).

[36] A. Goeppert, *Regenerable polyamine based solid adsorbents for CO2 capture from the air,* Loker Hydrocarbon Research Institute (2014).

[37] K. S. Lackner, *The thermodynamics of direct air capture of carbon dioxide,* Energy **50**, 38 (2013).

[38] M. Broehm, J. Strefler, and N. Bauer, *Techno-Economic Review of Direct Air Capture Systems for Large Scale Mitigation of Atmospheric CO2,* SSRN Electronic Journal (2015), 10.2139/ssrn.2665702.

[39] *Negative Emissions Technologies and Reliable Sequestration* (National Academies Press, Washington, D.C., 2019) pp. 189–228.

[40] G. Holmes and D. W. Keith, *An air–liquid contactor for large-scale capture of CO 2 from air,* Philosophical Transactions of the Royal Society A: Mathematical, Physical and Engineering Sciences **370**, 4380 (2012).

[41] *CE demonstration plant – a year in review,* (last accessed on 25 July 2019).

[42] R. P. Lively and M. J. Realff, *On thermodynamic separation efficiency: Adsorption processes,* AIChE Journal **62**, 3699 (2016).

[43] *Capturing CO2 from Air,* (last accessed on 12 July 2019).

[44] E. Ping, M. Sakwa-Nowak, and P. Eisenberger, *Global Thermostat low cost direct air capture technology,* in *International Conference on Negative CO2 Emissions* (Gothenburg, 2018).

[45] T. Roestenberg, *Design Study Report - ANTECY Solar Fuels Development. Antecy. Hoevelaken, the Netherlands*, Tech. Rep. (2015).

[46] V. S. Derevschikov, J. V. Veselovskaya, T. Y. Kardash, D. A. Trubitsyn, and A. G. Okunev, *Direct CO2 capture from ambient air using K2CO3/Y2O3 composite sorbent,* Fuel **127**, 212 (2014).

[47] A. R. Kulkarni and D. S. Sholl, *Analysis of Equilibrium-Based TSA Processes for Direct Capture of CO 2 from Air,* Industrial & Engineering Chemistry Research **51**, 8631 (2012).

[48] A. Sinha, L. A. Darunte, C. W. Jones, M. J. Realff, and Y. Kawajiri, *Systems Design and Economic Analysis of Direct Air Capture of CO 2 through Temperature Vacuum Swing Adsorption Using MIL-101(Cr)-PEI-800 and mmen-Mg 2 (dobpdc) MOF Adsorbents,* Industrial & Engineering Chemistry Research **56**, 750 (2017).

[49] S. Voskian and T. A. Hatton, *Faradaic electro-swing reactive adsorption for CO 2 capture,* Energy & Environmental Science (2019), 10.1039/C9EE02412C.

[50] K. Lackner, *Capture of carbon dioxide from ambient air,* The European Physical Journal Special Topics **176**, 93 (2009).

[51] D. S. Goldberg, K. S. Lackner, P. Han, A. L. Slagle, and T. Wang, *Co-Location of Air Capture, Subseafloor CO 2 Sequestration, and Energy Production on the Kerguelen Plateau,* Environmental Science & Technology **47**, 7521 (2013).

[52] R. A. Freitas Jr., *The Nanofactory Solution to Global Climate Change: Atmospheric Carbon Capture*, Tech. Rep. (2015).

[53] N. Serrano Barthe, *Absorption of CO2 from the air using polyamines: Experiments, modelling and design,* (2019).

[54] S. Giannoulidis and S. Wagenaar, *Experimental testing and design of a direct air capture unit for methanol production*, Ph.D. thesis, Delft University of Technology (2018).

[55] D. van Laake, *Characterization of a sorbent for a small scale direct air capture system,* (2018).

[56] J. Seader, J. E. Henley, and D. K. Roper, *SEPARATION PROCESS PRINCIPLES - Chemical and Biochemical Operations*, 3rd ed. (John Wiley & Sons, Inc.) pp. 106–110.

[57] J. Brillo, A. I. Pommrich, and A. Meyer, *Relation between Self-Diffusion and Viscosity in Dense Liquids: New Experimental Results from Electrostatic Levitation,* Physical Review Letters **107**, 165902 (2011).

[58] C. Wilke and P. Chang, *CORRELATION OF DIFFUSION COEFFICIENTS IN DILUTE SOLUTIONS,* AIChE Journal **1** (1955).

[59] W. Hayduk and B. S. Minhas, *Correlations for prediction of molecular diffusivities in liquids,* The Canadian Journal of Chemical Engineering **60**, 295 (1982).

[60] T. G. Hiss and C. E.L., *Diffusion in High Viscosity Fluids,* AIChE Journal **19** (1973).

[61] F. Bougie and M. C. Iliuta, *Sterically Hindered Amine-Based Absorbents for the Removal of CO 2 from Gas Streams,* Journal of Chemical & Engineering Data **57**, 635 (2012).

[62] G. Puxty and M. Maeder, *The fundamentals of post-combustion capture,* in *Absorption-Based Post-combustion Capture of Carbon Dioxide* (Elsevier, 2016) pp. 13–33.

[63] N. El Hadri, D. V. Quang, E. L. Goetheer, and M. R. Abu Zahra, *Aqueous amine solution characterization for post-combustion CO2 capture process,* Applied Energy **185**, 1433 (2017).

[64] R. J. Littel, G. F. Versteeg, and W. P. M. van Swaaij, *Kinetics of COS with primary and secondary amines in aqueous solutions,* AIChE Journal **38**, 244 (1992).

[65] T. L. Donaldson and Y. N. Nguyen, *Carbon Dioxide Reaction Kinetics and Transport in Aqueous Amine Membranes,* Industrial & Engineering Chemistry Fundamentals **19**, 260 (1980).

[66] A. F. Ciftja, A. Hartono, and H. F. Svendsen, *Carbamate Stability Measurements in Amine/CO2/Water Systems with Nuclear Magnetic Resonance (NMR) Spectroscopy,* Energy Procedia **63**, 633 (2014).

[67] P. Singh, *Amine based solvent for CO2 absorption : from molecular structure to process,* Ph.D. thesis, University of Twente, Enschede, The Netherlands (2011).

[68] X. Zhang, R. Zhang, H. Liu, H. Gao, and Z. Liang, *Evaluating CO2 desorption performance in CO2-loaded aqueous tri-solvent blend amines with and without solid acid catalysts,* Applied Energy **218**, 417 (2018).

[69] F. Mani, M. Peruzzini, and P. Stoppioni, *CO2 absorption by aqueous NH3 solutions: speciation of ammonium carbamate, bicarbonate and carbonate by a 13C NMR study,* Green Chemistry **8**, 995 (2006).

[70] A. Sayari and Y. Belmabkhout, *Stabilization of Amine-Containing CO 2 Adsorbents: Dramatic Effect of Water Vapor,* Journal of the American Chemical Society **132**, 6312 (2010).

[71] X. Xu, C. Song, B. G. Miller, and A. W. Scaroni, *Influence of Moisture on CO 2 Separation from Gas Mixture by a Nanoporous Adsorbent Based on Polyethylenimine-Modified Molecular Sieve MCM-41,* Industrial & Engineering Chemistry Research **44**, 8113 (2005).

[72] A. D. Ebner, M. L. Gray, N. G. Chisholm, Q. T. Black, D. D. Mumford, M. A. Nicholson, and J. A. Ritter, *Suitability of a Solid Amine Sorbent for CO 2 Capture by Pressure Swing Adsorption,* Industrial & Engineering Chemistry Research **50**, 5634 (2011).

[73] S.-Y. Horng and M.-H. Li, *Kinetics of Absorption of Carbon Dioxide into Aqueous Solutions of Monoethanolamine + Triethanolamine,* Industrial & Engineering Chemistry Research **41**, 257 (2002).

[74] A. Aboudheir, P. Tontiwachwuthikul, A. Chakma, and R. Idem, *Kinetics of the reactive absorption of carbon dioxide in high CO2-loaded, concentrated aqueous monoethanolamine solutions,* Chemical Engineering Science **58**, 5195 (2003).

[75] E. B. Rinker, S. S. Ashour, and O. C. Sandall, *Kinetics and Modeling of Carbon Dioxide Absorption into Aqueous Solutions of Diethanolamine,* Industrial & Engineering Chemistry Research **35**, 1107 (1996).

[76] B. P. Mandal, M. Kundu, and S. S. Bandyopadhyay, *Density and Viscosity of Aqueous Solutions of (N -Methyldiethanolamine + Monoethanolamine), (N -Methyldiethanolamine + Diethanolamine), (2-Amino-2-methyl-1-propanol + Monoethanolamine), and (2-Amino-2-methyl-1-propanol + Diethanolamine),* Journal of Chemical & Engineering Data **48**, 703 (2003).

[77] S. A. Udara, A. Neelakantha, A. E. Dag, and C. M. Morten, *Viscosities of Pure and Aqueous Solutions of Monoethanolamine (MEA), Diethanolamine (DEA) and N-Methyldiethanolamine (MDEA),* ANNUAL TRANSACTIONS OF THE NORDIC RHEOLOGY SOCIETY **21** (2013).

[78] R. Macıas-Salinas, F. Garcıa-Sánchez, and G. Eliosa-Jiménez, *An equation-of-state-based viscosity model for non-ideal liquid mixtures,* Fluid Phase Equilibria **210**, 319 (2003).

[79] J. Zhang, P. S. Fennell, and J. P. M. Trusler, *Density and Viscosity of Partially Carbonated Aqueous Tertiary Alkanolamine Solutions at Temperatures between (298.15 and 353.15) K,* Journal of Chemical & Engineering Data **60**, 2392 (2015).

[80] I. Kim and H. F. Svendsen, *Heat of Absorption of Carbon Dioxide (CO 2) in Monoethanolamine (MEA) and 2-(Aminoethyl)ethanolamine (AEEA) Solutions,* Industrial & Engineering Chemistry Research **46**, 5803 (2007).

[81] A. Abdulkadir, A. V. Rayer, D. V. Quang, N. E. Hadri, A. Dindi, P. H. Feron, and M. R. Abu-Zahra, *Heat of Absorption and Specific Heat of Carbon Dioxide in Aqueous Solutions of Monoethanolamine,3-piperidinemethanol and Their Blends,* Energy Procedia **63**, 2070 (2014).

[82] N. McCann, M. Maeder, and H. Hasse, *Prediction of the overall enthalpy of CO2 absorption in aqueous amine systems from experimentally determined reaction enthalpies,* Energy Procedia **4**, 1542 (2011).

[83] P. Datt, *Latent Heat of Vaporization/Condensation,* (2011) pp. 703–703.

[84] J. Cakstins, *Thermal properties of polyethyleneimine (PEI) impregnatedmesoporous silica,* Journal of the Department of Chemical and Environmental Engineering:University of Nottingham 2015 (2015).

[85] W. Zhang, H. Liu, C. Sun, T. C. Drage, and C. E. Snape, *Performance of polyethyleneimine–silica adsorbent for post-combustion CO2 capture in a bubbling fluidized bed,* Chemical Engineering Journal **251**, 293 (2014).

[86] J. Kapica-Kozar, B. Michalkiewicz, R. J. Wrobel, S. Mozia, E. Piróg, E. Kusiak-Nejman, J. Serafin, A. W. Morawski, and U. Narkiewicz, *Adsorption of carbon dioxide on TEPA-modified TiO 2 /titanate composite nanorods,* New Journal of Chemistry **41**, 7870 (2017).

[87] I. Smal, Q. Yu, R. Veneman, B. Fränzel-Luiten, and D. Brilman, *TG-FTIR Measurement of CO2-H2O co-adsorption for CO2 air capture sorbent screening,* Energy Procedia **63**, 6834 (2014).

[88] F. Tamajón, E. Álvarez, F. Cerdeira, and M. Vázquez, *Comparative Study of CO2 Absorption in Aqueous Mixtures of Methyldiethanolamine (MDEA) and Methanol, Focusing on the Temperature and Concentration Influence over the Absorption Rate,* Defect and Diffusion Forum **353**, 193 (2014).

[89] J. Xia, M. Jödecke, Á. Pérez-Salado Kamps, and G. Maurer, *Solubility of CO 2 in (CH 3 OH + H 2 O),* Journal of Chemical & Engineering Data **49**, 1756 (2004).

[90] TESTO, *Data sheet testo 885,* (last accessed on 21 October 2019).

[91] ADDA, *ADDA - AD12038GP Series Data Sheet,* .

[92] A. Mills, *Introduction and Elementary Heat Transfer,* in *Basic Heat and Mass Transfer* (Pearson Education Limited, 1998) 2nd ed., Chap. Chapter 1:, pp. 1–22.

[93] Engineering ToolBox, *Thermal Conductivity of selected Materials and Gases,* (last accessed on 12 November 2019).

[94] A. Mills, *Multidimensional and Unsteady Conduction,* in *Basic Heat and Mass Transfer*, edited by 2 (1998) Chap. 3, pp. 193–207.

[95] T. L. Bergman, A. S. Lavine, F. P. Incropera, and D. P. Dewitt, *Two-Dimensional Steady-State Conduction,* in *Fundamentals of Heat and Mass Transfer* (John Wiley & Sons, Inc., 2011) 7th ed., Chap. 4, pp. 230–255.

[96] B. STEINBERG, *Thermal Flow Working Principle and Theory,* (2013).

[97] A. Mills, *Convection Fundamentals and Correlations,* in *Basic Heat and Mass Transfer* (Peasrson Education Limited, 1998) 2nd ed., Chap. 4, pp. 262–284.

[98] A. Mills, *Appendix,* in *Basic Heat and Mass Transfer* (Pearson Education Limited, 1998) 2nd ed., Chap. A.

[99] T. L. Bergman, A. S. Lavine, F. P. Incropera, and D. P. Dewitt, *Introduction,* in *Fundamentals of Heat and Mass Transfer* (Jihn Wiley & Sons, Inc., 2011) 7th ed., Chap. 1, p. 8.

[100] D. M. Himmelblau and J. B. Riggs, *Basic Principles and Calculations in Chemical Engineering, 8th Edition*, 8th ed. (Prentice Hall, Austin, 2012) p. 102.

[101] *Monthly weather forecast and Climate Amsterdam, Netherlands,* (last accessed on 18 October 2019).

[102] B. Ovaa, *Direct Air Capture: An experimental approach on the desorption of CO2 and H2O from PEI and TEPA*, Ph.D. thesis, Delft University of Technology (2019).

[103] M. TOLEDO, *Karl Fischer Coulometers - Operating Instructions,* ().

[104] J. Coates, *Interpretation of Infrared Spectra, A Practical Approach,* in *Encyclopedia of Analytical Chemistry* (John Wiley & Sons, Ltd, Chichester, UK, 2006).

[105] *How to Interpret An Infrared Spectrum,* (last accessed on 19 July 2019).

[106] W. Perkins, *Fourier Transform-Infrared Spectroscopy,* Topics in chemical instrumentations **63** (1986).

[107] *IR Spectroscopy Tutorial: Amines,* (last accessed on 4 July 2019).

[108] *Characteristic IR Absorption Frequencies of Organic Functional Groups,* (2016).

[109] P. Jackson, K. Robinson, G. Puxty, and M. Attalla, *In situ Fourier Transform-Infrared (FT-IR) analysis of carbon dioxide absorption and desorption in amine solutions,* Energy Procedia **1**, 985 (2009).

[110] K. Robinson, A. McCluskey, and M. I. Attalla, *An ATR-FTIR Study on the Effect of Molecular Structural Variations on the CO2 Absorption Characteristics of Heterocyclic Amines, Part II,* ChemPhysChem **13**, 2331 (2012).

[111] T. Scientific, *Thermo Scientific TQ Analyst – Professional Edition,* (2015).